Building the Oceanic Lithosphere: Geophysical Analysis and Numerical Simulations of Rheology and Dynamics in the Formation of Transform Faults and Hotspot Island Chains

A Dissertation

Presented in Partial Fulfillment of the Requirements for the

Degree of Doctor of Philosophy

with a

Major in Geology

in the

College of Graduate Studies

University of Idaho

by

Thomas A. Morrow

Major Professor: Eric Mittelstaedt, Ph.D.

Committee Members: Catherine Cooper, Ph.D.; Jerry Fairley, Ph.D.;

Jessica Stanley, Ph.D.

Department Administrator: Leslie Baker, Ph.D.

August 2019

Authorization to Submit Dissertation

This dissertation of Thomas A. Morrow, submitted for the degree of Doctor of Philosophy with a Major in Geology and titled "Building the Oceanic Lithosphere: Geophysical Analysis and Numerical Simulations of Rheology and Dynamics in the Formation of Transform Faults and Hotspot Island Chains," has been reviewed in final form. Permission, as indicated by the signatures and dates below is now granted to submit final copies for the College of Graduate Studies for approval.

Advisor:	Eric Mittelstaedt, Ph.D.	Date
Committee:	Catherine Cooper, Ph.D.	Date
	Jerry Fairley, Ph.D.	Date
	Jessica Stanley, Ph.D.	Date
Department Chair:	Leslie Baker, Ph.D.	Date

Abstract

The oceanic lithosphere comprises over half of the Earth's surface. In this dissertation, I explore rheologic characteristics and dynamic evolution of the lithosphere through a series of investigations of mid-oceanic ridge transform faults, fracture zones, and hotspot island chains. I use geophysical observations from satellite- and ship-based collections to measure structure, deformation, and melt fluxes as well as constrain dynamic numerical simulations of long-term lithosphere movements. From these observations and models, I characterize the heterogeneous strength of the lithosphere across length scales and interpret dynamic behavior in rising thermal plumes from the Earth's mantle.

Acknowledgements

Funding for this work was provided by the National Science Foundation (NSF), the Republic of Korea National Research Foundation (NRF), the National Oceanographic and Atmospheric Administration (NOAA), the Graduate and Professional Student's Association of the University of Idaho, and the University of Idaho College of Science.

Additional support for this work came from the University of Idaho, Department of Geological Sciences; Chungnam National University, Department of Geological Sciences, Daejeon, Republic of Korea; NOAA's Pacific Marine Environmental Laboratory; the crew and science party of the R/V *Onnuri*; the crew and science party of NOAA Ship *Okeanos Explorer*. Computational facilities and support were provided by the University of Idaho Institute for Bioinformatics and Evolutionary Studies (IBEST) and the Northwest Knowledge Network (NKN).

Dedication

For my family and my partner Courtney, and all of the friends and faculty who have helped me along the way. Thank you for your support.

Statement of Contribution

Coauthors for the published work presented in chapter two are T.A. Morrow, E.L. Mittelstaedt, and S.S. Kim. The project was conceptualized by Morrow and Mittelstaedt, funding was acquired by Morrow. Original observations were collected by Kim during an NRF-funded cruise as part of a separate project. Structural mapping and interpretation was carried out by Morrow. Model methodology and development was carried out by Morrow with support and input from Mittelstaedt and Kim. The original draft was written by Morrow with a joint effort in review and revisions by Morrow, Mittelstaedt, and Kim.

Table of Contents

List of Tables

List of Figures

Chapter 1: The Oceanic Lithosphere

1.1 Introduction

The rigid oceanic lithosphere covers roughly three-fifths of the surface of the Earth. Our knowledge of its composition, history, behavior, and response to mantle convection and plate tectonics is severely limited by our ability to access and sample the seafloor and observe tectonic motions. Rather, geophysical and other remotely-sensed observations as well as numerical simulations provide crucial insight into oceanic lithosphere behavior over millions of years.

In this dissertation, I quantify the tectonic impacts of rheologic heterogeneities and mantle dynamics on the oceanic lithosphere using numerical models and geophysical observations. Through these models and observations, I connect small-scale lithosphere heterogeneities in rheology or distributions of magmatism to large-scale tectonic features and processes. I also summarize ways in which these million-year processes may impact human life on the scale of hundreds of years to mere minutes (i.e., how long-term changes in oceanic lithosphere construction affect the distribution of volcanism and earthquakes on our planet). Below, I briefly describe some important characteristics of the oceanic lithosphere and how numerical models approximate these characteristics. I highlight shortcomings of some of these approximations and then describe how each chapter of the dissertation addresses the complexities associated with a mechanically heterogeneous oceanic lithosphere.

1.2 Lithosphere, defined

The oceanic lithosphere initially forms at mid-ocean ridges, where upwelling material from within the mantle partially melts, cools, crystallizes into mineral phases,

and produces new solid lithosphere. A typical crystallization sequence for extracted melts is $olivine(\pm spinel) \rightarrow olivine + plagioclase(\pm spinel) \rightarrow olivine + plagioclase + clinopyroxene$. The bulk behavior of these mineral assemblages depends on their depth, temperature, susceptibility to alteration, and the influences of overlying seawater.

Both crust and mantle make up the oceanic lithosphere. The crustal section is defined by four lithologic layers (Winter, 2001). The shallowest layer consists of deep-sea sediments with a thickness that varies significantly throughout the ocean basins (Fowler, 2005). Pillow basalts form layer 2A and 2B (2A and 2B are distinguished by their relative porosity), while sheeted dikes form layer 2C, with a combined thickness of 1.0-1.5 km. Below layer 2 lies the 2-5 km-thick gabbro sequence, which grades from layer 3A isotropic gabbros into more organized layer 3B gabbro cumulates. The upper section of ultramafic layer 4 consists of layered peridotite (wehrlites) above harzburgites, which are interpreted as the residual material left after melt extraction to form the upper layers. These layers were originally defined using ophiolite sequences (sections of obducted oceanic crust) and may also be identified *in situ* by their P-wave seismic velocity. Below the crust lies the lithospheric mantle, which is predominantly composed of peridotite.

The strength of the lithosphere is dependent on its thickness and thus, its age (Figure 1.1). The thickness of the lithosphere h increases with age as it cools

$$h \propto \sqrt{\kappa t} \tag{1.1}$$

where κ is thermal diffusivity and t is time. The cooling and thickening lithosphere acts as a rigid, elastic lid above the viscous asthenosphere. The lithosphere supports loads and will bend underneath their mass. After unloading, the lithosphere will recover some loading strain and rebound in elastic recovery (Ekman and Mäkinen, 1996).

Interactions with seawater modify the mineralogy and strength of the oceanic lithosphere. Seawater penetration into the lithosphere is evidenced by hydrothermal venting

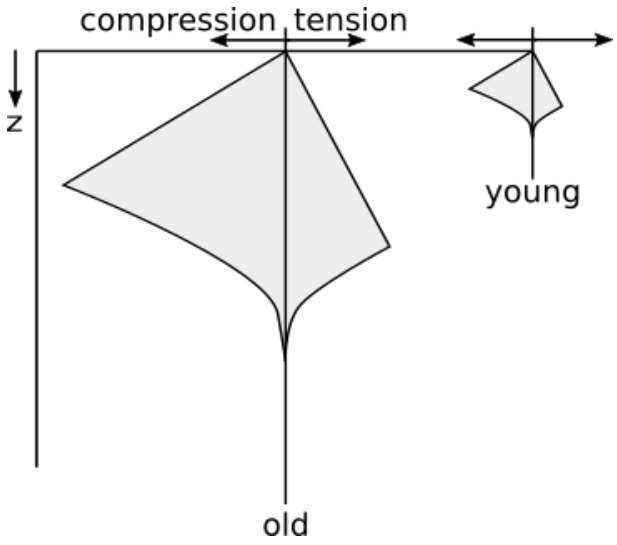

Figure 1.1: Schematic yield strength envelopes for old and young oceanic lithosphere (Watts, 2001)

(Macdonald et al., 1980). Exposed sections of lithosphere are often altered by low-grade metamorphic reactions, when olivine and pyroxene are serpentinized, producing lizardite, chrysotile, and antigorite (Winter, 2001). Talc may also be present in some serpentinites (Winter, 2001). These alteration products are significantly weaker than their un-altered counterparts, and may serve to localize deformation in the oceanic lithosphere (Escartín et al., 2001a).

1.3 Numerical simulations of oceanic lithosphere

Our understanding of the oceanic lithosphere is rapidly growing with the advent of new, detailed observations and increasingly-powerful numerical simulations. Expanded computational capacities allow for more detailed modeling and inclusion of more complex processes, linking observations across spatial and temporal scales beyond the observational limits of a human lifetime. Satellite-derived observations provide global maps of bathymetry (Ryan et al., 2009), gravity (Sandwell et al., 2014), and sediment cover (Whittaker et al., 2013), which serve to infer relationships between discrete, local obser-

vations. Detailed sampling and survey at individual sites (for example, observations from the NOAA Ship *Okeanos Explorer*'s expeditions to the Musicians Seamounts presented in chapter two, below), reveal highly localized heterogeneities in the oceanic lithosphere that may have wide-ranging tectonic impacts (Morrow et al., 2019). These impacts may develop over the lifetime of the oceanic lithosphere (100s of millions of years), culminating in historically significant impacts on human society (Manea et al., 2014). Connections between tectonic processes and human impacts across temporal and spatial scales become recognizable when observations and numerical models reveal their cumulative effects and interactions.

Numerical geodynamic simulations generally treat the oceanic lithosphere as a high-viscosity layer in a visco-plastic or visco-elastic-plastic rheology. Many models rely on a viscosity contrast of 3-5 orders of magnitude between the lithosphere and the asthenosphere (e.g., Gerya, 2010a; Behn and Ito, 2008) and employ a variety of yielding and failure methodologies to simulate deformation and brittle failure (e.g., Buck, 2006; Lavier et al., 2000; Lavier and Buck, 2002). Yielding criterion are often derived from experimental data on monomineralic, synthesized, or averaged material compositions deforming at strain rates much higher than typical lithosphere experiences (Escartín et al., 1997). Thus, many numerical simulations are simplifying micro- and macro-scopically heterogeneous materials into averaged parameters, often to improve the numerical feasibility of the simulation; simulating complex materials can require intense computational resources.

Recently, elastic rheologies have been included in numerical simulations capable of resolving kilometer-scale features in model domains spanning hundreds of kilometers (e.g., fracture zones, Figure 1.2). Only recently have numerical capabilities been able to simulate tectonic-scale processes with sufficient resolution to capture individual faults and structural features (e.g., Olive et al., 2016; Lavier et al., 2000; Behn and Ito, 2008), instead of integrating their effects into a bulk rheologic behavior. In chapters two and

four I take advantage of such improvements in computational capabilities to examine 100 km-scale behaviors and responses in the lithosphere as a function of single kilometer-scale discontinuities representing localized alteration products and brittle deformation features. Although the simulations presented here do not capture the full range of oceanic lithosphere heterogeneity described above, my models attempt capture physical behaviors on scales relevant to the problems being addressed.

1.4 Summary and preview

Each chapter focuses on the production or evolution of different heterogeneities within the oceanic lithosphere. In chapter two, I explore the consequences of hydrothermal alteration and enhanced pore fluid pressures along closely-spaced fracture zones. A series of seafloor measurements of transform fault and fracture zone geometries comprises chapter three; I relate these observations to changing plate motions over geologic time and infer controls on TF segmentation. In chapter four, I attempt to model an orthogonal ridge-TF-ridge system in a homogeneous elastic layer, subject to well-studied constraints used in other numerical models. Chapter five is a quantification of twelve hotspot melt fluxes, with methodologies that rely on assumed qualities of the lithosphere. The total impact of the heterogeneities described here may best be previewed by a map of known lithosphere discontinuities (Figure 1.2). The observations and models presented here serve to further our understanding of the mechanically heterogeneous oceanic lithosphere.

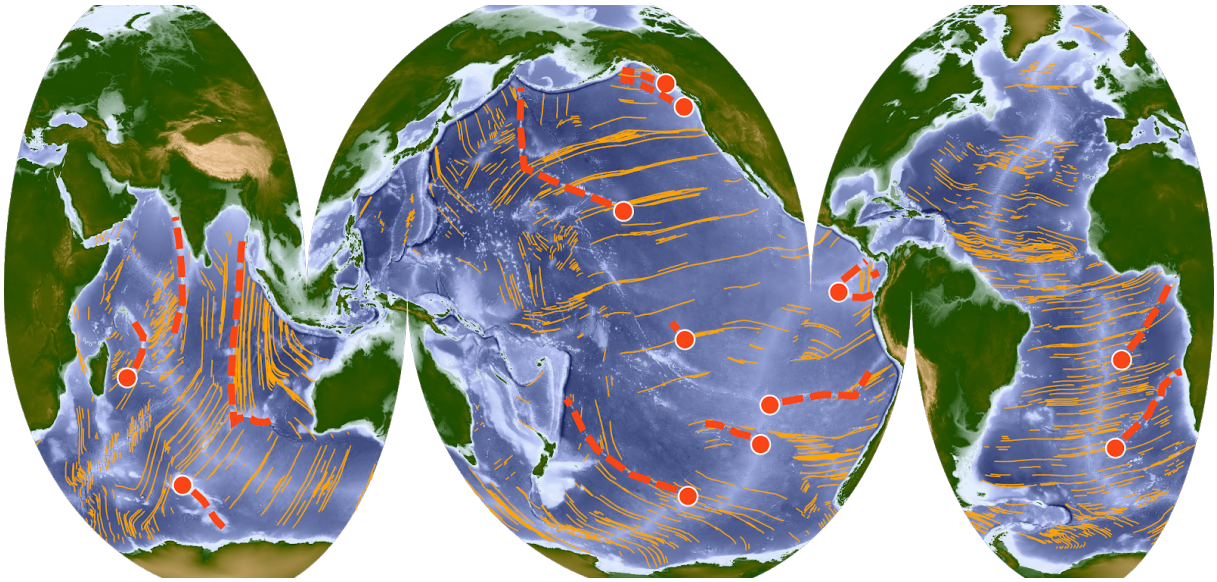

Figure 1.2: The Global Seafloor Fabric and Magnetic Lineation database (Matthews et al., 2011) contains a record of major fracture zones and lithosphere discontinuities (orange lines). Twelve hotspots (red dots) included in this study leave a trail of magmatic material (red dashed lines) as tectonic plates traverse over their mantle plume sources. Such features are abundant throughout each ocean basin and contribute to the lithosphere's heterogeneous composition and behavior.

Chapter 2: Weak Fracture Zones

Morrow, Thomas A, Eric Mittelstaedt, and Seung-sep Kim (2019). "Are segmented fracture zones weak? Analytical and numerical models constrain anomalous bathymetry at the Clarion and Murray fracture zones". In: *Earth and Planetary Science Letters* 512, pp. 214–226. doi: 10.1016/j.epsl.2019.02.010.

2.1 Introduction

Fracture zones (FZ) are ocean basin-scale discontinuities in oceanic lithosphere that preserve a record of the tectonic history of mid-ocean ridge (MOR) transform fault (TF) offsets (e.g., Atwater et al., 1993). In addition to recording the direction of relative tectonic motions within the TF, differential subsidence rates of younger, relatively warm lithosphere on one side of the FZ and older, relatively cold lithosphere on the other side of the FZ can cause continued vertical slip along the FZ interface after it leaves the TF (Wessel, 1990). Vertical slip ceases within a few million years as FZs strengthen and lock in the isostatic step produced by this differential subsidence (Sandwell and Schubert, 1982). Further differential subsidence along the now locked FZ creates a flexure profile with a young-side high and old-side low, features characteristic of the locked fault model for FZ evolution (Sandwell and Schubert, 1982; Parmentier and Haxby, 1986; Wessel, 1990; Christeson and Mcnutt, 1992).

The locked fault model is inconsistent with observations at many fracture zones (Wessel, 1990; Bonneville and McNutt, 1992; Christeson and Mcnutt, 1992; Kruse et al., 1996). For example, Kruse et al., 1996 found that half of all Geosat crossings of Pacific fracture zones have gravity anomaly profiles that conflict with the locked fault model. Conflicting profiles were attributed to re-orientation changes (i.e., changes in spreading rate and orientation) modifying tectonic structure within the TF during FZ formation. Features

considered diagnostic of such re-orientation modifications include closely-spaced fracture zones separated by intra-transform spreading center (ITSC) fabrics (Searle, 1983; Fornari et al., 1989), parallel ridge and trough structures (Jordahl et al., 1995), and transverse ridges and uplifted scarps (Tucholke and Schouten, 1988; Bonatti et al., 1994). In extreme cases, compression across a TF can vertically extrude mantle material up to 3500 m above the seafloor (Maia et al., 2016). Most features inconsistent with the locked fault model are thought to form in the active TF and to be subsequently inherited and preserved by the FZ (e.g., Kruse et al., 1996), not to be the result of active FZ processes.

Consistent with FZ inheritance of syn-formational structures, high shear strength is estimated across old FZs (20 MPa at 85 Myr, Jordahl et al. (1995); 5-40 MPa after first few million years, Kruse et al. (1996)). Yet, for millions of years after their formation, FZs may remain relatively weak (Wessel, 1990; Hall and Gurnis, 2005). Geoid anomaly and bathymetry observations (Wessel, 1990) suggest that FZs are sufficiently weak to allow vertical slip during the first 4 Myr after departing the TF. Furthermore, numerical simulations suggest that FZs may have yield stresses $<$10 MPa for up to 10 Myr (Hall and Gurnis, 2005). If FZs are relatively weak for some time after leaving the active TF, then structural features within and around FZs must be interpreted in the context of both intra- and post-transform deformation.

Formed by localized, intense deformation at TFs, young FZs are likely regions of pervasive alteration due to fluid circulation. Indeed, fluid penetration to mantle depths promotes serpentinization and alteration along TFs (Bonatti and Honnorez, 1976; Dick, 1989; Cannat and Seyler, 1995; Detrick et al., 1993; Rüpke and Hasenclever, 2017). At segmented FZs (those formed at closely spaced TFs separated by ITSCs), alteration likely affects greater volumes of mantle compared to un-segmented FZs. However, the degree to which fluid circulation and chemical alteration affects TF and FZ dynamics is difficult to quantify.

Here, we present analyses of new multibeam bathymetry data collected within the segmented region of the Clarion FZ (152°–140°W and 12°–16°N) and the segmented region of the Murray FZ, (159.5°–157.5°W and 28°–30°N). These new data reveal structural features and FZ morphology that are systematically inconsistent with the locked fault model. First, seafloor bounded by closely spaced FZs dips in the opposite direction to that predicted for locked fracture zones, and second, in some locations expected isostatic depth relationships are reversed, such that older lithosphere is shallower than younger lithosphere. Though these features may be inherited from accretionary processes at the ITSC, our aim is to understand if they could have been produced during evolution of the FZs as they migrate away from the active TF. To assess the physical processes responsible for the anomalous observations listed above, we use analytical and numerical models to simulate the thermo-mechanical evolution of closely-spaced FZs.

2.1.1 Geologic Setting

The Clarion fracture zone (Figure 2.1) marks the trace of a formerly active transform fault along the Pacific-Farallon spreading center. The total age offset across the FZ varies from 4 Myr to 10 Myr along its length. Active during the Cretaceous, the Clarion transform fault has been traced back to Mathematician Ridge, where spreading was abandoned during a plate boundary reorganization at 5 Ma (Demets and Traylen, 2000). The Murray FZ (Figure 2.1) shares a similar history with Clarion, with a 4.5 Myr age offset across the FZ. Full spreading rates along the Pacific-Farallon spreading center are estimated to have been 65 to 90 mm/yr from the end of the Cretaceous (83 Ma) until 53.5 Ma, 100 mm/yr from 53.5 Ma to 43.79 Ma, and 160 mm/yr from 43.79 Ma to 40 Ma (Rowan and Rowley, 2014).

The Clarion and Murray TFs were subjected to several changes in spreading direction (Rowan and Rowley, 2014). These changes modified the configuration of the transform

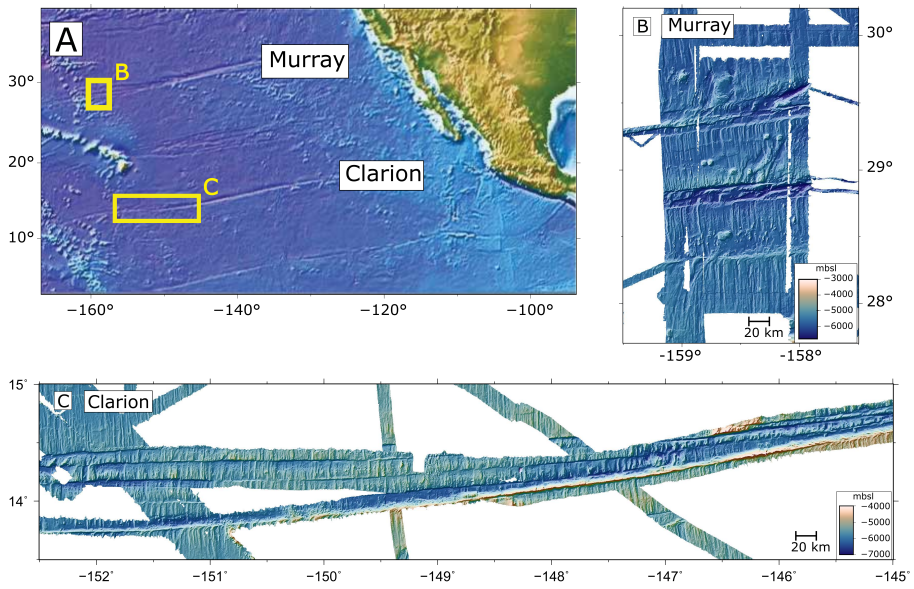

Figure 2.1: (A) Numerous, thousand-kilometer-long oceanic fracture zones cross the Pacific Plate, including the Clarion FZ and Murray FZ. New, high-resolution (200 m or smaller grid cell size) multibeam swath bathymetry provide new insights into the morphology and structure of the segmented portion of the (B) Murray FZ and (C) Clarion FZ. New coverage highlights regions formed at intra-transform spreading centers, between fracture zones. Approximate global locations are shown in (A).

faults (Menard and Atwater, 1968), leaving behind a complex array of closely-spaced fracture zones (Figure 2.1). By the end of the Cretaceous Magnetic Quiet Zone (CMQZ), the Clarion FZ was comprised of six distinct FZ strands recording the tectonic history of six closely-spaced TFs separated by intra-transform spreading centers (ITSCs) and the Murray FZ was comprised of at least 3 closely-spaced TFs separated by ITSCs (Figure 2.1).

2.2 Bathymetric data and interpretation

In 2009, the R/V *Onnuri* collected in-transit swath bathymetry along previously unsurveyed portions of the Clarion FZ between 153°W and 138°W using an EM120 multibeam echo sounder. The soundings were auto-cleaned with MB-System and gridded at 0.02 arc-minutes (200 m), then combined with existing high-resolution observations from

the Global Multi-Resolution Topography (GMRT) Synthesis (Ryan et al., 2009). In 2017, the NOAA ship *Okeanos Explorer* surveyed a section of the Murray FZ between 159.5°and 157.5°W using an EM302 multibeam echo sounder. Soundings were similarly cleaned and gridded at 200 m and combined with existing observations from GMRT for analysis. Our new observations at Clarion are restricted to the region between 153°and 140°W, corresponding to a period from the end of the late Cretaceous to 40 Ma, and at Murray between 159.5°and 157.5°W, corresponding to a period between 92.5-87.5 Ma.

To examine changes in tectonic structure between different regions along both FZs, we construct representative bathymetric profiles in several locations. We extract 200 km-long, FZ-perpendicular bathymetric profiles from only high-resolution ship-based data (GMRT synthesis) and the new observations presented here, spaced 200 m apart and calculate their median value to generate a single FZ-perpendicular profile that is representative of the general tectonic bathymetry and excludes small-scale features, such as abyssal hill fabric and smaller seamounts (Figure 2.2B-F, Figure 2.3). From these tectonic cross sections, we interpret across-FZ structural relationships for each region.

The large-scale features of the Clarion FZ reflect accommodation of changing plate motions through the late Cretaceous (100 Ma) and into the Paleogene (40 Ma) by reorientation of the active TF. From the westernmost extent of the field area, the Clarion FZ widens from a single FZ into a series of 6 parallel FZs, each spaced 20 km apart. Magnetic isochron data do not clearly resolve the sense of offset across each individual FZ; we assume they shared the same offset direction, as is commonly observed in existing segmented TFs (for example, the Quebrada-Discovery-Gofar system, Pickle et al. (2009)). Rotation poles derived from the earliest available magnetic isochron crossing the FZ (chron 34, 83 Ma) (Rowan and Rowley, 2014) predict that the Clarion TF was in a state of transpression until 68 Ma. The predicted period of transpression coincides with the merging of several FZs, leaving only one distinguishable FZ (Figure 2.1). The outermost intra-

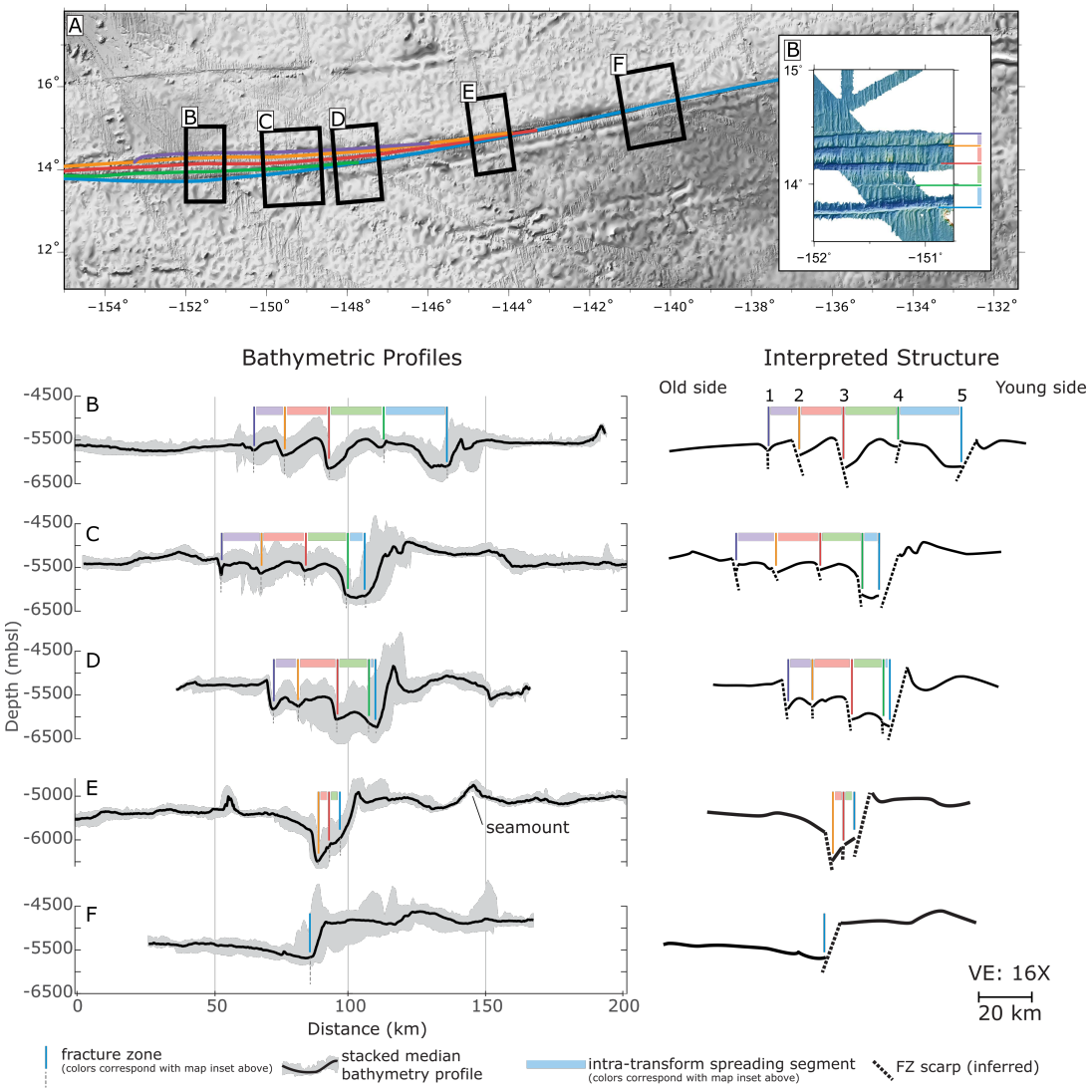

Figure 2.2: Using new data and existing high-resolution multibeam data (A) we construct a series of representative cross-sections from boxes (B–F) to characterize the evolution of the segmented Clarion FZ over time. Cross sections (B–F) are median-filtered sections taken perpendicular from the FZ trace at 200 m spacings, using only high-resolution ($<$ 200 m) soundings. The gray field indicates the total depth range in each box, the heavy black line indicates the median value for all FZ-perpendicular sections. Inset (B) delineates the five closely-space FZs in the field area (colored lines) and their corresponding intra-transform spreading center generated crust (colored bars). An interpreted structure diagram corresponding to each median profile (B–F) shows locations where bathymetry is consistent with a "locked fault" thermal subsidence model. At many locations, including FZ 2, 3 in profile (B), FZ 1-4 in profile (C), FZ 1, 3 in profile (D), age-depth relationships are reversed and interior FZ blocks dip towards the old side of the FZ (blocks 1, 2, 3 in (B), 2 in (C), 1 and 2 in (D)).

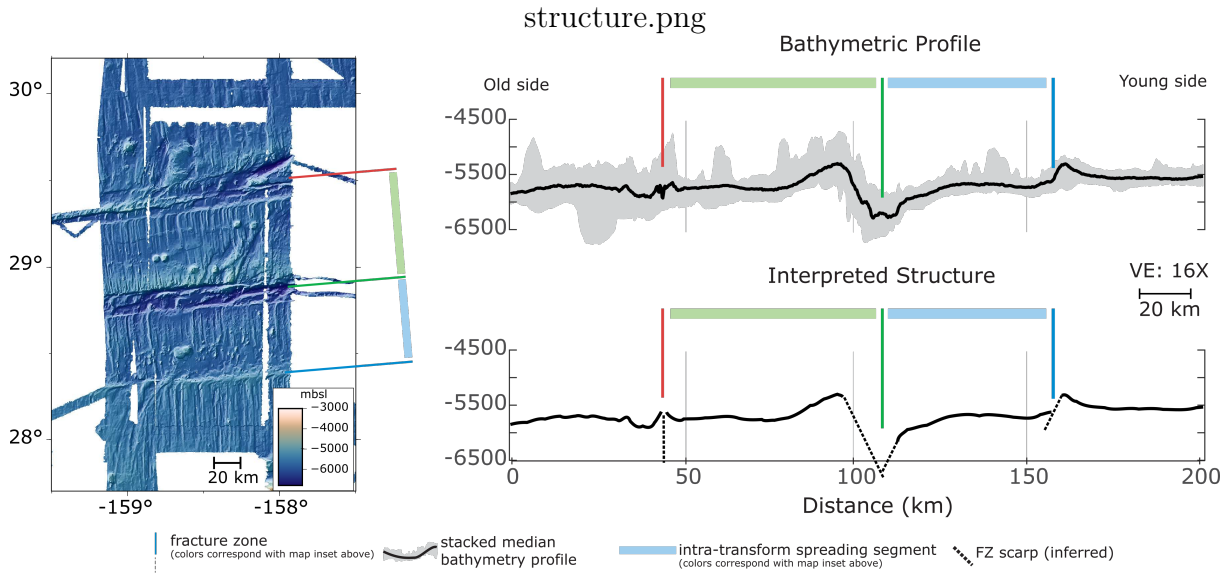

Figure 2.3: As for Fig. 2.2, but for new bathymetry in the Murray FZ. One profile is constructed from the combination of new data and existing high-resolution coverage. The three FZs (colored lines) and regions of intra-transform generated material (colored bars) are indicated on the map inset and in the structural diagram. At the southernmost FZ (blue), older lithosphere lies deeper than younger lithosphere, consistent with conductive plate cooling models (e.g., Turcotte and Schubert, 2002). At the central FZ (green), this relationship is reversed and a large region of chaotic structures dominates the FZ seafloor expression. At FZ 3, structural age-depth relationships are ambiguous.

transform segments close first and, as each intra-transform section shortens, spreading fabrics within the segments become less apparent and their general orientation rotates counter-clockwise from a predominantly spreading-perpendicular direction. Although the spreading fabric between FZs closes from outside to inside, the second southernmost FZ (number 5 in Figure 2.2) remains while changing orientation across the field area. After 68 Ma, transtension is predicted along the TF and the remaining FZ persists until 40 Ma when the FZ again segments into at least 3 parallel FZs.

At the Murray FZ, our new observations are more restricted in time; rotation poles suggest that the active Murray TF in our study area would have also been in a state of transpression. The southernmost trace (Figure 2.1) is localized to a vertical offset in the bathymetry (Figure 2.3), whereas the middle and northern FZs are characterized

by broader valleys containing complex structures. The FZs are separated by regions of ITSC-generated crust, exhibiting spreading-perpendicular abyssal hill fabrics.

Within the segmented region of the Clarion and Murray FZs, predictions from the locked fault model do not always hold (Figure 2.2 and 2.3). If each FZ was behaving as a locked fault, flexure associated with thermal subsidence would cause all the interior ITSC-produced blocks of lithosphere (i.e., blocks of lithosphere bounded by FZs) to tilt down towards the younger side of the FZs (south). At the Clarion FZ, however, the interior FZ blocks often tilt down towards the old side of the FZ (Figure 2.2, blocks 1, 2, 3 in (B), 2 in (C), 1 and 2 in (D), 2 and 3 in (E)). At the Murray FZ, neither of the two interior blocks dip in a southward direction, in fact the northern block appears to dip in the opposite direction (Figure 2.3). Additionally, isostasy predicts younger, warmer lithosphere to rest at shallower depths than older, colder lithosphere. At many locations, including FZs 2 and 3 in profile (B), FZs 1-4 in profile (C), and FZs 1 and 3 in profile (D) at Clarion (Figure 2.2), and the middle FZ at Murray FZ (Figure 2.3) this predicted age-depth relationship is reversed. Hereinafter we will refer to these unexpected characteristics as reverse tilt, where interior blocks dip towards the old side of the FZ, and scarp reversal, where older lithosphere lies shallower than younger lithosphere across a FZ. These observations violate the predictions of the locked fault model (Haxby and Parmentier, 1988) and predictions of thermal subsidence based upon plate cooling models (Turcotte and Schubert, 2002).

2.3 Analytical and Numerical Modeling

2.3.1 Conceptual model of post-transform fracture zone evolution

Figure 2.4A illustrates the conceptual framework for our mathematical and numerical models of FZ evolution. Along a given transect perpendicular to the TF (X-X' in Figure

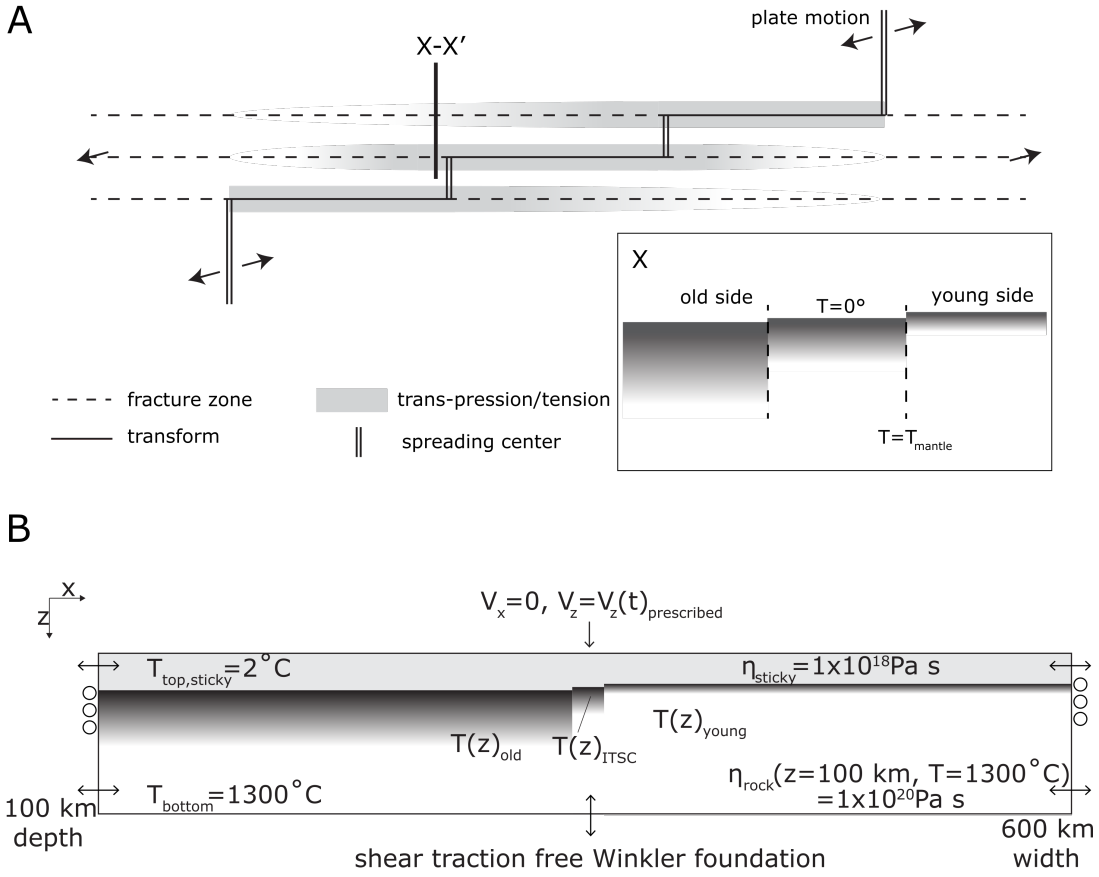

Figure 2.4: (A) Conceptual model for early evolution of two closely spaced FZs within a segmented TF. Compression or tension may occur across the FZs in the active TF region, but limited compression or tension across FZs occurs outside the outermost ridge-transform intersections (RTIs). This geometry leads to tectonic-scale motions across FZs early in their evolution. Cross-section X-X': The thermal profile (gradient) is determined by the age of the lithosphere and the topography of the surface is determined by isostatic equilibrium. (B) Boundary and initial conditions for numerical models. The top boundary of the domain is a free-slip condition with prescribed inflow determined by the subsidence rate of the oldest section of modeled lithosphere and the bottom boundary is a shear traction-free Winkler foundation. In the sticky air layer and where the rock material is viscous (where the Maxwell visco-elastic relaxation time is $<10 \times 10^{-2}$ times the time step), the sides of the model are traction free (open). We impose a free-slip condition (rollers) in elastic portions of the domain, which allows for vertical subsidence but no horizontal movement in or out of the model domain in cases simulating pure thermal subsidence. In compression or tension cases, prescribed inflow or outflow conditions are applied to the elastic portions of the lithosphere and several adjacent cells above and below the brittle material. Initial temperature profiles $T(z)$ are prescribed by a half-space cooling model depending on the initial modeled ages. The top boundary and sticky air layer are constant 2°C and the bottom boundary is 1300°C.

2.4A), two closely-spaced (<50 km) FZs separate an ITSC block from bordering lithosphere of different ages, younger on one side and older on the other. Initially, the ITSC block and bordering lithosphere are assumed to be in isostatic equilibrium. However, different rates of heat transfer to the ocean in young and old lithosphere results in differential subsidence, while lateral heat transfer between adjacent lithosphere of different ages imposes a torque on the ITSC block; heating of the ITSC block across one FZ causes a decrease in density while simultaneous cooling of the ITSC block across the other FZ causes an increase in density. If the FZ interfaces are sufficiently weak, the thermally-induced torque will rotate the ITSC block in the opposite sense to that expected for the locked fault model. Further rotation could be exacerbated by tectonic compression or extension due to changes in spreading direction. The staggered geometry of a segmented TF (Figure 2.4A) allows tectonic compression to influence the early structural evolution of the oldest two (upper and middle) FZs along profile X-X', provided tectonic stresses are transmitted across the active TF. The youngest (lower) FZ (not included in X-X') is relatively unaffected however, because it lies in a mostly intraplate setting.

2.3.2 Analytical model for buoyancy driven torques across segmented fracture zones

ITSC blocks may acquire a reverse tilt if frictional forces along the FZ interface are surpassed by a thermal buoyancy induced torque associated with heat transfer across the bounding fracture zones. To evaluate the conditions necessary for buoyancy-driven reverse tilt of an ITSC block, we derive a simplified analytical model of thermal diffusion across two FZs with specified age offsets.

Our analytical model calculates a force balance on a single block of coherent, rigid lithosphere bounded by one warm and one cool boundary, much like ITSC-produced lithosphere is bounded by FZs separating it from warmer, younger lithosphere on one side

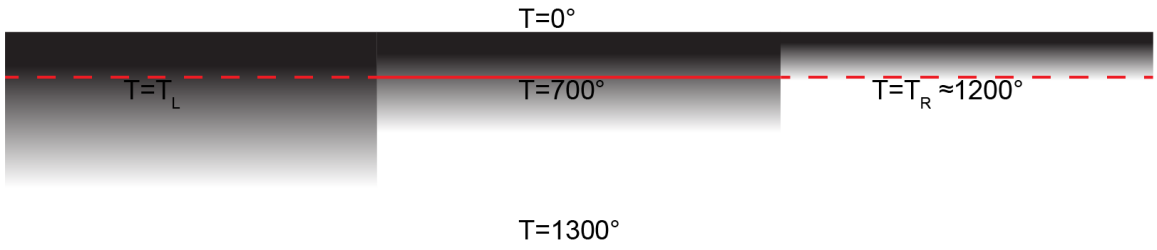

Figure 2.5: Initial conditions for thermal diffusion within a lithosphere block bounded by two closely-spaced fracture zones are set based upon the shown conceptual model. Using a half-space cooling model and the specified age of the internal block, we calculate the depth to the 700° C isotherm. Temperature profiles (grayscale) are determined by a half-space cooling model based on the chosen age offsets across the FZs and the age of the interior lithosphere block. The depth to the 700° isotherm in the interior block (solid red line) determines the depth in the left block which dictates the temperature TL, and TR is fixed at 1200° . Thermal gradients in all three blocks are determined by model time t and the age offsets across the two FZs t_1 and t_2.

and older, colder lithosphere on the other (Figure 2.4). Initially, the block is assumed to be in perfect isostatic equilibrium and to have a uniform temperature of 700°(we choose this temperature because the greatest thermal contrast between different age blocks will occur at depth in a half-space cooling model). We set the right boundary temperature to 1200°(young, warm mantle) and allow the thermal condition of the left side of the block to evolve with time following a half-space cooling model (cooling, older lithosphere). Initially, using a half-space cooling model, the left boundary temperature is calculated at the same depth as the 700° isotherm in the central block, but based upon the prescribed age of the left block.

Thermal evolution of the block is calculated by solving the 1-D heat equation subject to the above temperature conditions on the left T_L and right T_R boundaries

$$\frac{\partial T}{\partial t} = \kappa \frac{\partial^2 T}{\partial x^2}, \tag{2.1}$$

where T is temperature, t is time, κ is thermal diffusivity, and x is distance from the left side of the modeled interior block (Figure 2.5). Model parameters are listed in Table 2.1. Solving Equation 2.1 subject to these conditions yields

$$T(x) = T_L(t) + \frac{(T_R - TL(t)}{L}x + \sum_{n1=}^{infty} a_n e^{-\kappa t(\frac{n\pi}{L})^2} \sin\frac{n\pi x}{L}, \tag{2.2}$$

where L is width of the block (distance between FZs). The constant in the infinite summation, a_n, is defined as the integral

$$a_n = \int_0^L (T_{init} - T_L(t) - \frac{(T_R - TL(t)}{L}x) \sin\frac{n\pi x}{L} dx \tag{2.3}$$

where T_{init} is the initial temperature of the ITSC block. where T_L is set to as the temperature in the oldest block of lithosphere at depth h, which corresponds to the depth of the 700° isotherm in the central block following a half space cooling model (Turcotte and Schubert, 2002). T_L and h are both dependent on t_1 and t_2, the age offsets of the young and old FZs, respectively, as well as the model time t. Note that this calculation for thermal evolution is only valid from zero to two million years. Beyond two million years, the mantle adjacent to the ITSC block on the right side will cool below the T_R boundary condition value 1200°C and become part of the lithosphere.

We convert the thermal perturbation for each solution to a pressure differential ΔP (i.e., the upward or downward pressure associated with negative or positive change in density, respectively) via

$$\Delta P(x) = -\alpha\rho_0\Delta T(x)gh, \tag{2.4}$$

where α is the coefficient of thermal expansion, ρ_0 is the reference density, g is the acceperation due to gravity, and $\Delta T(x) = T_{init} - T(x)$. The left and right buoyancy pressures are treated as point forces producing two complementary moments acting in the same sense

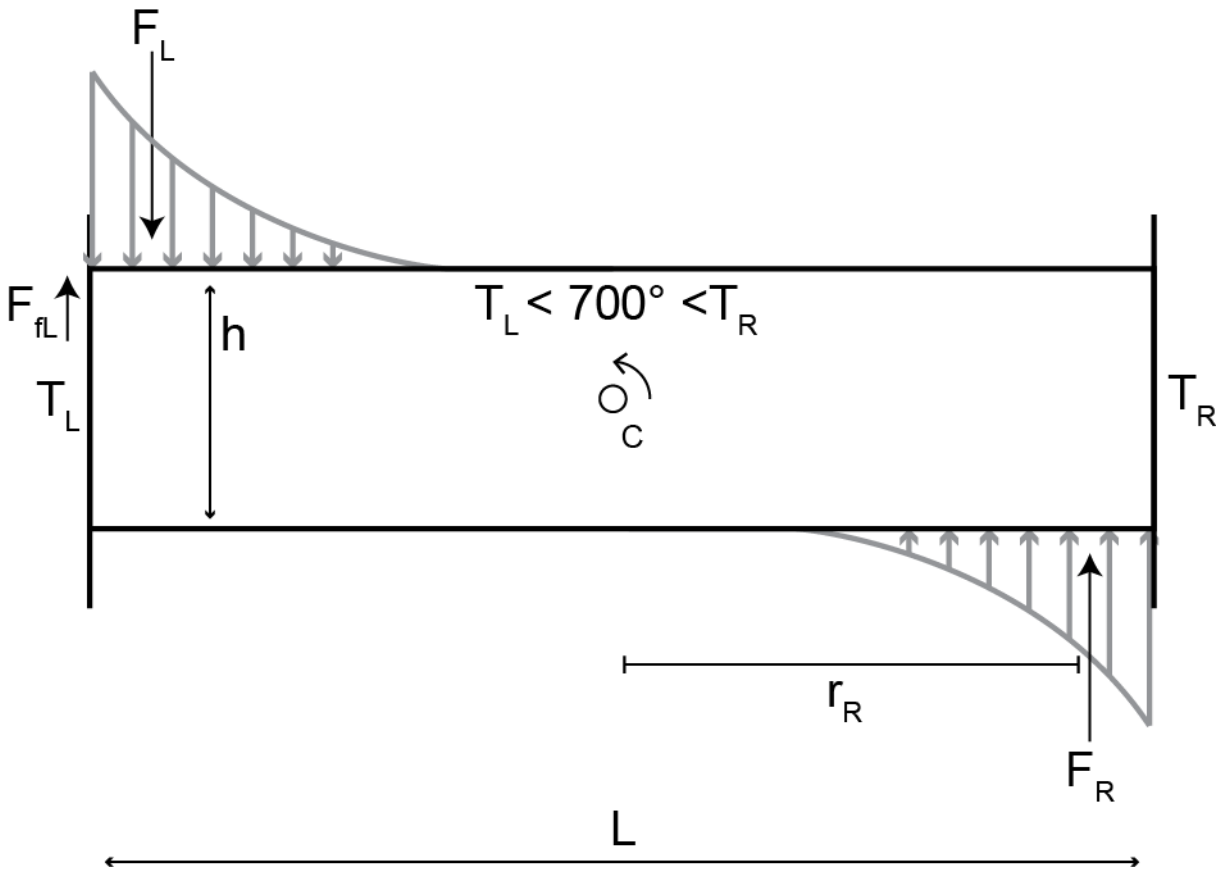

Figure 2.6: Torque balance for the center block, bounded by left-side temperature T_L and right-side temperature T_R. Positive and negative buoyancy forces produced by thermal diffusion (gray arrow fields) are treated as point forces F_R and F_L acting at distances r_R and r_L to rotate the block around a pivot point c. Torque due to frictional resistance along the side of the block $F_f L$ acts to oppose the buoyancy torques.

of rotation on the block acting at a distance r_L and r_R from the rotation axis location, c (Figure 2.6).

$$F_L = \int_0^c \Delta P(x)dx, \tag{2.5}$$

$$F_R = \int_c^L \Delta P(x)dx, \tag{2.6}$$

where F_L and F_R are the point force equivalent buoyancies acting on either side of the block. Note that F_L and F_R are forces per unit meter along the fracture zones (into and out of the page in Figure 2.6). The value of c is determined based on the location where $\Delta P = 0$, which is usually near (but not precisely) $x = L/2$; r_L and r_R are determined as the centroids of the left and right buoyancy differentials, respectively,

$$r_L = \frac{\int_0^c x\Delta P(x)dx}{\int_0^c \Delta P(x)dx}, \tag{2.7}$$

$$r_R = \frac{\int_c^L x\Delta P(x)dx}{\int_c^L \Delta P(x)dx} - c. \tag{2.8}$$

Bounding FZs are treated as simple, vertical interfaces along which thermal buoyancy-driven torques are resisted by static friction along the portion of the interface in the brittle deformation regime (shallower than the 700° isotherm). Using an apparent coefficient of friction μ_a to account for frictional forces and undifferentiated reductions to friction resistance (i.e., alteration or pore fluid effects), we balance the total torque on the block against frictional resistance along the FZ interface located between the interior block and older lithosphere. Assuming the block is in static equilibrium, the sum of the buoyancy torques must be resisted by a counter-acting torque produced by frictional resistance on the sides of the block. It is difficult to constrain the relative contributions from each side, however, the left (old) side of the block has the greatest depth to the brittle-ductile transition (700°isotherm) and the greatest area available for frictional forces to act on.

Therefore, we make the simplifying assumption that the left side friction torque exerts a stronger counter-torque on the block than the right side friction torque. We equate the sum of the buoyancy torques with the frictional torque on the left side and solve for the minimum apparent friction coefficient required to resist block rotation, μ_a

$$\mu_a = \frac{F_L r_L + F_R r_R}{c(\frac{1}{2}\rho_0 g h^2 - F_T)}, \tag{2.9}$$

where μ_a is the apparent coefficient of friction on the cold side of the block, F_L and F_R are the left and right buoyancy forces, respectively, r_L and r_R are the moment arm lengths for the cooling (left) and heating (right) moments, respectively, c is the distance from the left boundary to the rotational axis, h is the depth to the 700° isotherm, and F_T is the reduction to the normal force due to thermal contraction,

$$F_T = \frac{1}{3}\alpha E \int_0^L \Delta T(x) dx, \tag{2.10}$$

where E is Young's modulus.

Restricting our examination to one side of the interior block allows an end-member calculation of the largest frictional resistance (greater FZ surface in the brittle regime). The value of μ_a determined by the above equations represents the minimum apparent coefficient of friction along a discrete fault required to resist block rotation, driven by thermal buoyancy interactions. Here we use an apparent coefficient of friction which includes undifferentiated effects on frictional resistance, including chemical alteration and pore fluid pressure (Beeler et al., 2000). If the interface on the side of the block is comprised of a material with an apparent coefficient of friction less than μ_a, our model predicts that thermal buoyancy torques will overcome resistive forces and the block will rotate. If the interface on the side of the block has an apparent coefficient of friction

greater than μ_a, our model predicts the block will remain in static equilibrium and will not rotate.

2.3.3 Analytical model assumptions and limitations

The analytical model presented here is valid under the following assumptions and limitations. First, we assume the temperature of the hot side, T_R is fixed at 1200° C. In a half-space cooling model, this temperature would decrease with time as the thermal boundary between older and younger lithosphere diffuses. Thus, our analytical results are only valid for a short time (2 Myr), before the right boundary cools significantly below 1200° C. Second, our model is not dynamic. The analytical model results do not predict amounts or rates of rotation and our rigid beam approximation does not account for flexure of the internal block, which likely becomes an important dynamic process with greater FZ separation. We calculate temperature differentials at the depth of the 700° isotherm, which does not take into consideration the temperature of the overlying material. However, this assumption works to maximize thermal torque magnitudes and thus maximize estimates of μ_a. We assume in equation 2.10 that contributions to thermal stresses from outside the FZs are at least equal to contributions from the interior block, an additional assumption that works to maximize predicted values of μ_a. Using only the thermal stress reduction from the interior block does not significantly alter the results. We assume that μ_a is significantly greater than the coefficient of friction on the right side of the block, which will act over a smaller area due to the depth of the brittle-ductile transition being shallower on the hot side of the block. Finally, we treat FZs as flat, smooth fault interfaces despite evidence of complex damage zones up to several kilometers in width along some FZs. The above assumptions and limitations were chosen with the goal of finding first-order estimates of the friction coefficients required to prevent rotation of a FZ-bounded lithosphere block.

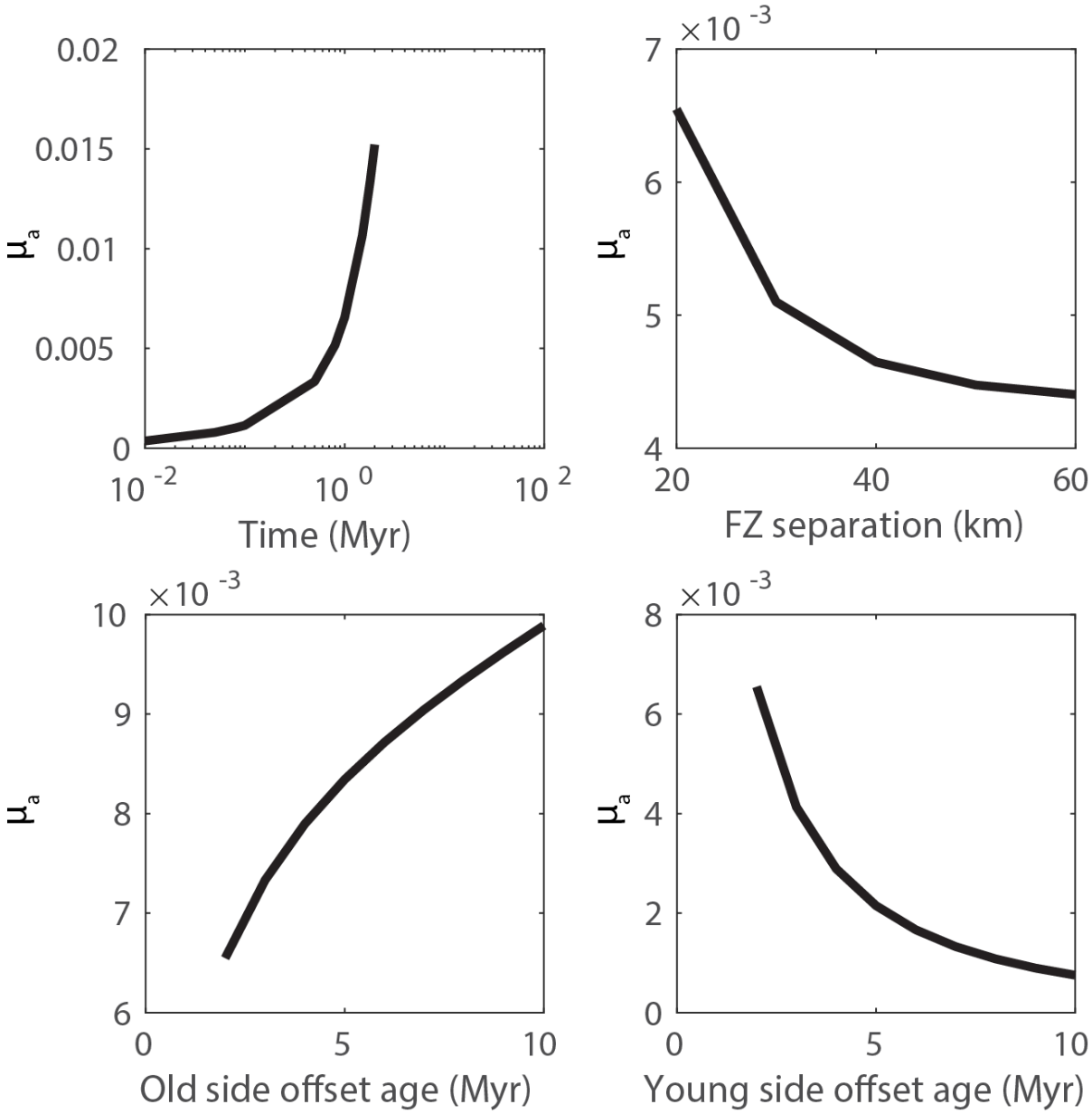

Figure 2.7: Analytical model results. (A) μ_a predictions with time for a fixed block length L=20 km and fixed FZ age offsets of 2 Myr each. (B) For a fixed time of 1 Myr and fixed FZ age offsets of 2 Myr each, μ_a decreases with increasing FZ separation L. (C) and (D) show μ_a predictions at 1 Myr and L=20 km for different FZ age offsets on the old and young sides, respectively.

We evaluate our model for a range of parameters (Table 2.1) to characterize the model behavior for a limited set of results (Figure 2.7). As time t increases, the minimum left-side apparent coefficient of friction required to resist rotation increases. With increasing FZ separation, the minimum coefficient of friction decreases (Figure 2.7). For larger age offsets across the old side of the FZ, μ_a increases. On the young side, as the FZ age offset increases, mu_a decreases.

Table 2.1: Analytical model constants

Parameter	Description	Value (units)
κ	Thermal diffusivity	1×10^{-6}
T_R	Right side bounding temperature	1200°C
T_{init}	Interior block initial temperature	700°C
ρ_0	Reference density	3200 kg m^{-3}
α	Thermal expansivity	3×10^{-5} K^{-1}
g	Gravitational acceleration	9.8 m s^{-2}
E	Young's modulus	30 GPa
L	Block length	20–60 km
t_1	Young side FZ age offset	2–10 Myr
t_2	Old side FZ age offset	2–10 Myr
T_L	Left side bounding temperature, derived from t, t_1, t_2	-
c	Moment axis x location	-

Results from the above simplified analytical model indicate that FZs must be vanishingly weak to produce reverse tilts. For example, after 1 Myr of thermal evolution of a 20 km-long block with age offsets of 2 Myr across each FZ (oldest lithosphere in model is 5 Myr) a value of μ_a =0.01 provides sufficient frictional force to resist the buoyancy-driven torque on the interior block. In fact, the maximum buoyancy-driven torques calculated in our model (t=2 Myr, block initial ages 10 Myr and 2 Myr for the left side and interior block, respectively) will only overcome frictional resistance on FZs with $\mu_a \leq 0.028$. A model using the same age offsets (Müller et al., 2008) and structural details for the Clarion FZ suggests that $\mu_a \geq 0.01$ along the old-side of the FZ could resist thermally-driven rotation. Results of the above analytical model provide insights into the conditions required

for development of reverse tilts of ITSC blocks, but do not address dynamic controls on the magnitude and rate of reverse tilt accumulation and formation of scarp reversals; thus, we developed a thermo-mechanical numerical simulation of FZ evolution.

2.3.4 Numerical Model

We model the thermal subsidence of three lithosphere blocks separated by two, closely spaced FZs using the 2-D finite difference, marker-in-cell code SiStER (Olive et al., 2016). SiStER solves the equations of conservation of mass, momentum, and energy for an incompressible, visco-elastic-plastic material

$$\frac{\partial v_i}{\partial x_i} = 0, \tag{2.11}$$

$$\frac{\partial \sigma_{ij}^{'}}{\partial x_j} - \frac{\partial P}{\partial x_i} + \rho g_i = 0, \tag{2.12}$$

$$\rho C_p \frac{DT}{Dt} = \frac{\partial}{\partial x_i}\left(k \frac{\partial T}{\partial x_i}\right), \tag{2.13}$$

where v indicates velocity, $\sigma_{ij}^{'}$ denotes deviatoric stress (indices i and j indicate the vertical or horizontal direction respectively; repeated indices indicate summation), and T is temperature. Density, heat capacity, and thermal conductivity are indicated by ρ, c_p, and k, respectively. On the left-hand side of Equation 2.13, $\frac{DT}{Dt}$ is the material time-derivative of T.

Rheologically, we simulate deformation of a visco-elastic-plastic material. Viscous deformation is simulated using a temperature-dependent Newtonian rheology,

$$\eta_{Newt} = A e^{\frac{E}{RT}}, \tag{2.14}$$

where η is viscosity, A is the pre-exponential constant, E is the activation energy, and R the gas constant. Elasticity is incorporated by assuming that the lithosphere behaves

as a Maxwell solid and placing source terms for the elastic stresses on the right-hand size of the momentum equation (e.g., Moresi et al., 2003; Olive et al., 2016).

Plastic deformation occurs when stresses surpass the brittle yield stress determined by a Drucker-Prager failure criterion

$$\sigma_y = BP_L + C \tag{2.15}$$

where P_L is the lithostatic pressure, determined by integrating overburden densities with depth for each solution, and constants B and C are defined as

$$B = sin\phi, \tag{2.16}$$

$$C = C_0 \cos\phi, \tag{2.17}$$

$$\phi = \tan^{-1}\mu_a \tag{2.18}$$

where C_0 is cohesion and ϕ is the friction angle. The apparent coefficient of friction μ_a (Equation 2.18) is a material constant similar to the one used in the analytical model. When and where material fails plastically we introduce a plastic viscosity η_{plas}

$$\eta_{plas} = \frac{\sigma_y}{\ddot{\epsilon_{II}}}, \tag{2.19}$$

where $\ddot{\epsilon_{II}}$ is the second invariant of the strain rate. At each point, the effective viscosity is defined as a harmonic average of the plastic (Equation 2.19) and material viscosities (Equation 2.14)

$$\eta_{eff} = \left(\frac{1}{\eta_{Newt}} + \frac{1}{\eta_{plas}}\right)^{-1}. \tag{2.20}$$

The above formulation yields elastic-plastic behavior in the cold lithosphere and viscous deformation in the warmer asthenosphere. Equations are solved in non-dimensional form using parameter scales appropriate to the thermal subsidence problem (Table 2.2). Further model details can be found in Olive et al. (2016).

Model initial and boundary conditions (Figure 2.4) are designed to isolate the thermomechanical evolution of two closely-spaced FZs. The initial thermal profile is prescribed by a half-space cooling model (Turcotte and Schubert, 2002) determined by the age of each lithosphere block. Above the lithosphere layer lies a low density, low viscosity "sticky air" layer (Crameri et al., 2012), which allows for the development of surface topography. Along the top boundary we impose zero tangential velocities and a prescribed inflow equal to the subsidence rate of the oldest lithosphere in the domain. This inflow condition minimizes movement of the sticky air layer across the domain (which has an aspect ratio of 6:1) as a response to differential subsidence between young and old lithosphere. The bottom boundary is shear traction-free and open to flow with a Winkler foundation (based on isostatic equilibrium) constraining pressure. Along the vertical sides of the domain, we impose mixed boundary conditions. In the sticky air layer and where the rock material is viscous, the sides are traction free (open), allowing inflow to compensate for subsidence on the younger side of the domain. In the elastic portions of the domain (i.e., the lithosphere, as determined by the model Maxwell time) and ten numerical cells above and below, the sides have zero shear tractions to allow for vertical subsidence and prescribed normal velocities that differ between model types (thermal subsidence $\pm$ extension or compression). The model domain (600 km x 100 km) is discretized over 300 x 50 nodes with spatially varying grid refinement; in the x dimension, grid spacing varies from 1 km between 280-320 km (centered on the FZs) and 2 km elsewhere, while in the y direction grid spacing is 500 m in the upper 60 km of the domain and 2 km elsewhere. A sensitivity

test (Table 2.3) with a further halving of the refined grid spacing (500 m in x and 250 m in y) yielded identical model results.

FZs are simulated in one of two ways: 1) a discontinuity in thermal structure with no difference in material properties between the FZ and the surrounding lithosphere, and 2) a discontinuity in thermal structure and a 2 km wide by 20 km deep region of weak material. The width of each weak zone is similar to the 2 km wide damage zone observed in inversions of seismic refraction data at the Gofar TF (Roland et al., 2012) and the depth is chosen to exceed the depth to the brittle-ductile transition. By specifying the plasticity parameters within these weak zones, we control the degree of coupling between adjacent pieces of lithosphere. Material within weak zones has zero cohesion ($C_0 = 0$ in Equation 2.17), such that the yield stress is directly controlled by the apparent coefficient of friction (μ_a, in Equation 2.18). In using an apparent coefficient of friction, we include undifferentiated processes (i.e., alteration or poroelastic effects) that would act to modify frictional resistance or reduce the normal force across the FZs (e.g., Beeler et al., 2000). To initialize deformation within weak FZs, we fix the strain rate in the weak material to the predicted differential subsidence rate between the oldest and youngest lithosphere divided by the width of the weak zone for ten time steps (<100 kyr model time). After this time, continued deformation within the weak zones occurs dynamically. Additional material parameters are listed (Table 2.2).

Guided by results from our analytical model and observations at the Clarion and Murray FZs, we examine a range of values for coefficient of friction and FZ age offsets. Our analytical model suggests that FZs must be very weak to allow reverse tilts (i.e., low coefficient of friction) and that the buoyancy-driven torque is controlled primarily by the age offset between the interior block and the old (cold) side. Using spreading rates (Rowan and Rowley, 2014) and available crustal ages (Müller et al., 2008), we find a maximum age offset along the Clarion FZ of 10 Myr. Thus, in our simulations we test

Table 2.2: Non-dimensional scales and material parameters.

Parameter	Notation	Value (units)
Reference viscosity	η_0	1×10^{20} Pa s
Reference velocity	v_0	1×10^{-7} m s^{-1}
Reference density	ρ_0	3300 kg m^{-3}
Domain height	H_0	100 km
Gravitational acceleration	g	9.8 m s^{-2}
Shear modulus[1]	G	30 GPa
Thermal conductivity[1]	k	3.0 W m^{-1} K^{-1}
Heat capacity[1]	C_p	1000 kg m^2 K^{-1} s^{-2}
Pre-exponential	A	1×10^{-3}
Activation energy[1]	E	540 kJ mol^{-1}
Gas constant	R	8.314 J mol^{-1} K^{-1}
Apparent coefficient of friction	μ_a	0.001, 0.01, 0.1, 0.56
Sticky air density[2]	ρ_{sticky}	0.01 kg m^{-3}
Sticky air viscosity[2]	η_{sticky}	1×10^{18} Pa s
Cohesion[3]	C_0	0–44 MPa
Coefficient of thermal expansion[4]	α	1×10^{-5} K^{-1}

[1] Turcotte and Schubert (2002);
[2] Crameri et al. (2012);
[3] Lavier and Buck (2002);
[4] Choi et al. (2008).

values of the FZ coefficient of friction of 0.001, 0.01, 0.1, and 0.58, and examine old side age differentials of 2, 5, and 8 Myr relative to an initially 2 Myr old ITSC block (the young side differential is fixed at 2 Myr). Additionally, we test ITSC block lengths of 20, 30, and 40 km (block width at Clarion and Murray range from 20 to 40 km). In models with tectonic motions, we test compression and extension rates between 1×10^{-13}–1×10^{-10} m/s, covering a range of rates estimated from Pacific-Farallon rotation poles (Rowan and Rowley, 2014) and predicted TF obliquity at the Clarion and Murray FZs.

2.4 Results

To facilitate comparison of model results with seafloor observables, we report the tilt angle of the simulated ITSC block over time (Figure 2.8) and whether or not scarp

reversal occurs in a given model run (Table 2.3, Figure 2.9). Positive tilt angles (Figure 2.8) indicate ITSC blocks dipping down towards the young side of the FZ (consistent with a locked fault scenario). Conversely, negative tilt values (Figure 2.8) indicate ITSC blocks dipping down towards the old side of the FZ (reverse tilt). Tilt angles reported below have an error of $\pm 0.025^{\circ}$, based on the length of the interior block and assuming a marker advective error of ± 1 grid cell up or down.

Cases simulating strong, locked FZs (i.e., a thermal step, but no weak zone) accumulate positive tilt with time (Figure 2.8A). Interior blocks tilt down towards the young side of the FZ with flexure controlled young-side concave upward bend and an old-side concave downward bend (Figure 2.8B). Tilt increases with time at a progressively slower rate as the difference in subsidence rates (i.e., cooling rates) between the old and young sides of the FZ decreases.

Cases simulating weak, uncoupled FZs (i.e., a thermal step, zero cohesion, and small μ_a; Figure 2.8B and 2.8C) show similar behavior to strong locked faults for $\mu_a \geq 0.01$. In these cases, the central model block only tilts in the positive direction, but to a lesser degree than the fully-coupled model with no weak zone. Tilt angles achieve a maximum value by 1 Myr model time and, within error, remain unchanged until the model is stopped at 10 Myr. For models with a value of $\mu_a = 0.001$, interior blocks exhibit reverse tilts (Figure 2.8C). To confirm that lateral thermal diffusion is responsible for the modeled reverse tilts, we reduced the value of thermal diffusivity in the x direction (Table 2.3); for values of thermal diffusivity near zero, reverse tilts do not occur.

Next, we examine cases with constant FZ $\mu_a = 0.001$, but different values of block length and old-side FZ age-offset. Increasing ITSC block length (distance between FZs) does not significantly change the rate of tilt accumulation or final tilt angle, within error (Figure 2.8D). Regardless of block length, increasing old side age offset increases the rate of tilt accumulation and enhances the negative tilt angle (0.7° more negative in the 10

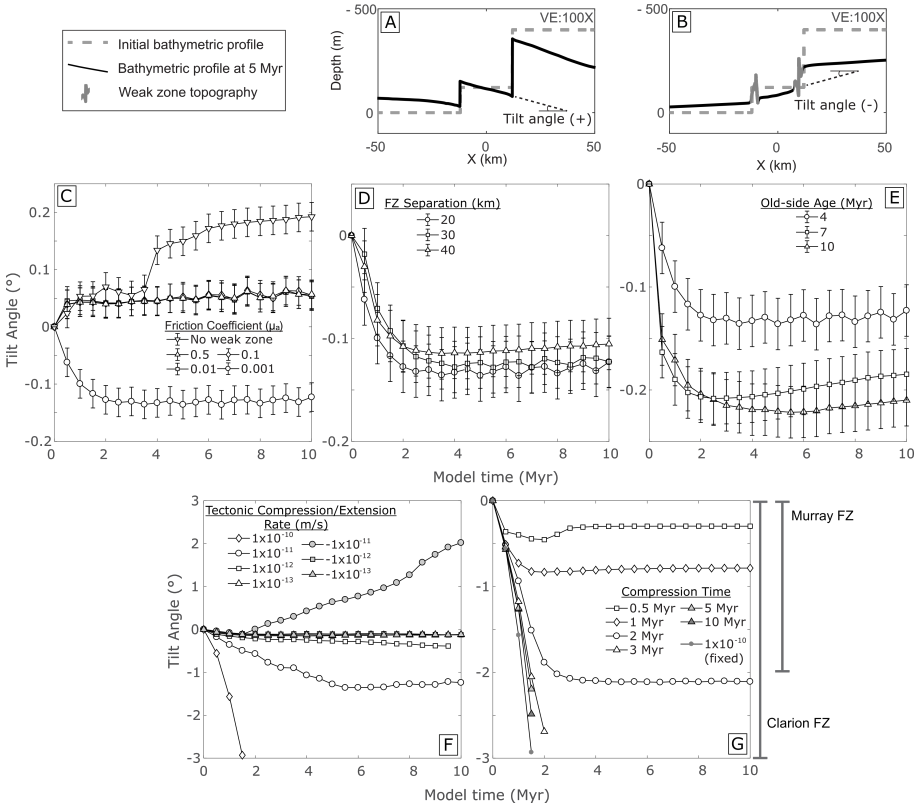

Figure 2.8: Numerical model results (note that only a small detail region of the model domain is shown here). (A–B) Model topography outputs (heavy black line) after 5 Myr model time for the pure thermal subsidence case with (A) no weak zones imposed and (B) weak zones with $\mu_a = 0.001$. Initial topography (dashed gray line) assumes isostatic equilibrium for each block. Tilt angles, the diagnostic feature of the "reverse tilt" bathymetric profile, are measured clockwise positive from horizontal. Negative tilt (seen in the weak model, B) is opposite of the predictions for a (A) strong, locked fault model. The weak zone implementation used here generates spurious topography at the FZs (light gray, B) and is ignored in our analysis. (C–G) Model results are reported as interior block tilt angle versus time relative to (C) coefficient of friction (fixed block length 20 km and age offsets 2 Myr), (D) fracture zone spacing (fixed $u_a = 0.001$ and age offsets 2 Myrs), (E) age offset between the interior and oldest block (fixed $\mu_a = 0.001$, block length 20 km, young side offset 2 Myr), (F) constant tectonic compression (+) or extension (-) rates (fixed $\mu_a = 0.001$, block length 20 km, age offsets 2 Myr), and (G) tectonic compression that diminishes over time (same fixed parameters as in F). Error bars in (C–G) are determined by the model grid resolution, assuming topography markers advect $\pm$ 1 vertical grid cell over the length of the interior block. Error bars are smaller than the symbol size in (F–G). Measurements of tilt angle are only considered valid where lithosphere failure does not occur (F–G, cases that stop at 2 Myr). Reverse tilt ranges for the Clarion and Murray FZs are indicated with grey bars.

Table 2.3: Numerical experiments

Model number	FZ μ_a	Comp.(+)/ ext.(−) rate (m s^{-1})	Tectonic period (Myr)	Old side age (Ma)	FZ separation (km)	Scarp Reversal	Tilt extremum ($\pm 0.025°$)
1	0.001	0	-	4	20	No	-0.136
2	0.01	0	-	4	20	No	0.061
3	0.1	0	-	4	20	No	0.064
4	0.5	0	-	4	20	No	0.063
5	0.001	0	-	10	20	No	-0.222
6	0.001	0	-	7	20	No	-0.208
7	0.001	0	-	4	30	No	-0.128
8	0.001	0	-	4	40	No	-0.114
9^A	-	0	-	4	20	No	0.192
10^B	0.001	0	-	4	20	No	0.149
11^C	0.001	0	-	4	20	No	0.149
12	0.001	1×10^{-11}	-	4	20	Yes	-1.358
13	0.001	1×10^{-12}	-	4	20	Yes	-0.388
14	0.001	1×10^{-13}	-	4	20	Yes	-0.151
15	0.5	1×10^{-13}	-	4	20	No	0.073
16	0.01	1×10^{-13}	-	4	20	No	0.068
17	0.001	1×10^{-11}	-	10	20	Yes	-1.032
18	0.001	1×10^{-13}	-	10	20	No	-0.355
19	0.001	-1×10^{-12}	-	4	20	No	-0.129
20	0.001	-1×10^{-11}	-	4	20	No	2.02
21^D	0.001	1×10^{-10}	-	4	20	Yes	-2.932
22	0.001	1×10^{-12}	-	10	20	No	-0.346
23^D	0.001	-1×10^{-10}	-	10	20	No	0.888
24	0.001	-1×10^{-11}	-	10	20	No	0.594
25^D	0.001	1×10^{-10}	-	10	20	Yes	-2.121
26	0.001	-1×10^{-12}	-	10	20	No	-0.213
27^D	0.001	1×10^{-10}	-	4	20	Yes	-2.932
28^D	0.001	5×10^{-11}	-	4	20	Yes	-3.35
29^D	0.001	1×10^{-10}	10	4	20	Yes	-2.486
30	0.001	-1×10^{-13}	-	4	20	No	-0.132
31^D	0.001	1×10^{-10}	5	4	20	Yes	-2.195
32	0.001	1×10^{-10}	2	4	20	Yes	-2.116
33^E	0.001	1×10^{-10}	1	4	20	Yes	-0.833
34^F	0.001	0	-	4	20	No	-0.177
35	0.001	1×10^{-10}	0.5	4	20	Yes	-0.454
36^D	0.001	1×10^{-10}	3	4	20	Yes	-2.689
37	0.5	1×10^{-11}	-	4	20	No	-0.136

Table 2.3 – continued from previous page

Model number	FZ μ_a	Comp.(+)/ ext.(−) rate (m s^{-1})	Tectonic period (Myr)	Old side age (Ma)	FZ separation (km)	Scarp Reversal	Tilt extremum ($\pm 0.025^\circ$)
38	0.1	1×10^{-11}	-	4	20	No	-0.177
39^D	0.1	-1×10^{-11}	-	4	20	No	-0.438
40^D	0.5	-1×10^{-11}	-	4	20	No	-0.086
41	0.1	1×10^{-12}	-	4	20	No	0.071
42	0.5	1×10^{-12}	-	4	20	No	0.067

[A] No weak zones imposed.
[B] $k_x = \frac{k_x}{1e10}$.
[C] $k_x = 0$.
[D] Indicates models where modeled lithosphere failed outsize FZs before 10 Myr.
[E] Model was duplicated and run for 20 Myr to verify long-term stability of the result.
[F] Resolution test, doubled model resolution within the refinement area, otherwise identical to simulation 1.

and 7 Myr cases relative to the 4 Myr case). The most extreme tilt angle occurs at times between 2 Myr and 6 Myr (Figure 2.8E) and decreases slightly over the model run. Scarp reversal does not occur in these models.

To examine the role of changes in plate motion direction on weak, segmented FZs (μ_a=0.001; old-side age offset = 2 Myr), we impose extension (−) or compression (+) on the box sides (e.g., Figure 2.4). Cases with imposed extension exhibit extension rate-dependent behavior (Figure 2.8F). Slow extension rates (extension rates $\geq -1 \times 10^{-11}$ m/s) yield similar tilts (-0.1°) to cases without extension. Cases with extension rates of -1×10^{-11} m/s show continuously increasing tilts up to $+2^\circ$ in the 10 Myr simulation time. Cases with imposed compression also exhibit rate-dependent behavior. For a compression rate of $+1 \times 10^{-11}$ m/s, the interior block accumulates increasingly negative reverse tilt up to -1.36° at 5 Myr. Lower compression rates ($\leq +1 \times 10^{-12}$ m/s) yield results similar to models with no compression ($\geq -0.2^\circ$ reverse tilt). Higher compression rates ($\geq +1 \times 10^{-10}$ m/s) increase the negative tilt accumulation rate, but lithosphere surrounding the modeled weak FZs begins to deform plastically at 1.5 Myr (Figure 2.8F). In summary, relative to thermal subsidence alone, incorporating extension in models with

weak FZs yields small reverse tilts for slow extension rates ($\leq +1 \times 10^{-12}$) and positive tilts for larger extension rates ($+1 \times 10^{-11}$); incorporating compression in models with weak FZs yields increasing magnitudes of reverse tilt with increasing compression rate. Additionally, cases with compression rates $\geq +1 \times 10^{-11}$ m/s are the only cases that exhibit scarp reversal.

Finally, we examine tectonic compression rates that decrease with time, as might be expected as a TF re-orients after a change in spreading direction. We ran a suite of models with identical initial compression rates ($+1 \times 10^{-10}$ m/s), and then linearly decrease the compression rate to zero over a fixed period of time that differs between cases (0.5, 1, 2, 3, 5, and 10 Myr; Figure 2.8G). Upon reaching zero compression rate, the model is allowed to evolve dynamically until reaching a model time of 10 Myr. All models where compression lasts longer than 3 Myr exhibit plastic deformation outside the imposed FZ weak zones after 1.5 myr (Figure 2.8G). Models where tectonic compression ceases within 2 Myr accumulate reverse tilt (up to -2°), which remains for the duration of the model (Figure 2.8G). All decreasing-rate compression cases exhibit scarp reversal. To verify that reverse tilt angles remain steady through time, we ran model 33 (Table 2.3) for 20 Myr; the tilt angle changed by $<0.1^{\circ}$ between 10 and 20 Myr.

2.5 Discussion

2.5.1 Conditions for violating the locked fault model

Many FZs have bathymetric features that are inconsistent with the locked fault model (Kruse et al., 1996), but the underlying causes for many of these unexpected features are poorly known. In particular, along segmented FZs we observe reverse tilts and scarp reversal of ITSC blocks, both of which violate the locked fault model. It is possible that crustal thickness variations due to magmatic overshoots from the adjacent ridge (or other

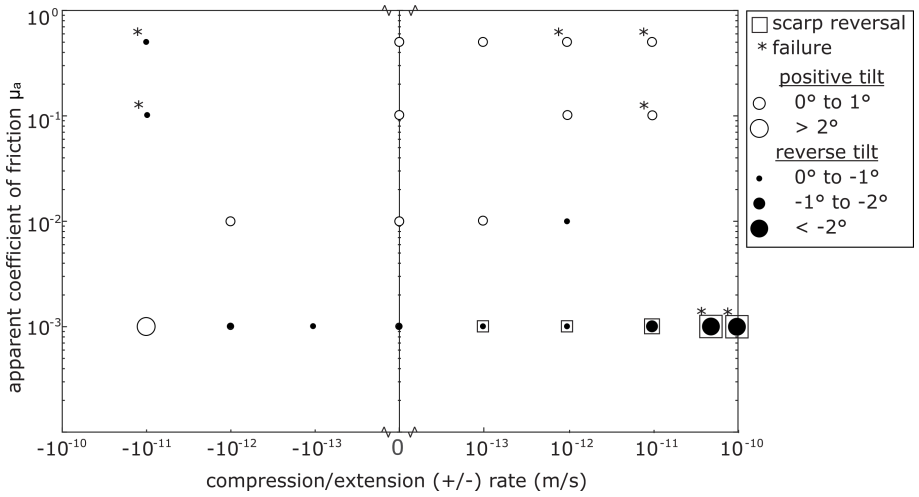

Figure 2.9: Model results plotted as compression/extension rate relative to μ_a suggest that only weak FZs under relatively high compression rates exhibit both reverse tilts and scarp reversals, as observed at Clarion and Murray FZs. Reverse tilt (filled circles) only occurs without lithosphere failure (indicated by stars) in cases with $\mu_a \leq 0.01$ and is amplified by tectonic compression. Scarp reversal (squares) only occurs in compressional models with μ_a=0.001.

magmatic processes) may produce this excess topography (Gregg et al., 2007). However, it is unlikely that sporadic overshoots would yield continuous thickening along the FZ; Pickle et al. (2009) use gravity and seismic data to show that ITSCs in the Quebrada-Discovery-Gofar area are not consistently regions of excess crust. We instead propose an alternative hypothesis which requires only thermal conduction across weak FZs to generate the anomalous bathymetry observed at Clarion and Murray FZs. Based upon our models of weak FZs, we suggest that reverse tilts and scarp reversals occur in very weak, young, segmented FZs and are driven by a combination of tectonic compression and thermal diffusion from the young, warm side of the FZs to the old, colder side. Diffusion creates a buoyancy gradient within the ITSC block that drives a torque counter to the forces produced by thermal subsidence and compression enhances the rotation of the block by enhancing the torque on the block.

Models of very weak FZs (depth-averaged yield strength <3 MPa) subject to tectonic compression result in reverse tilt and scarp reversals consistent with observations at the

Clarion and Murray FZs, but models of strong FZs or weak FZs without compression do not. We find that rapid compression rates ($\geq +1 \times 10^{-11}$ m/s) are required to generate the relatively large reverse tilt angles (>1°) observed, but that compression rates must decrease relatively quickly or lithosphere around the FZs will begin to fail plastically. If such plastic failure occurs along FZs, we would expect formation of observable structures along the FZ; No such structures are observed along the Clarion FZ, but the relatively large valleys along the Murray FZs may be indicative of such deformation.

In general, our results agree with previous estimates of FZ and TF strength. For example, FZs exhibiting reverse tilt features in our models must have yield strengths <3 MPa, in agreement with the Hall and Gurnis (2005) estimate of <10 MPa, but smaller than the Kruse et al. (1996) estimate of 5–40 MPa. However, the Kruse et al. (1996) estimate is restricted to old Pacific FZs (>10 Myr). Yet, our results do not conflict the Kruse et al. (1996) estimates because simulated formation of reverse tilt and scarp reversal features only require low yield strength values for 2–3 Myr after the FZ leaves the active TF; simulated reverse tilt features primarily accumulate within the first 5 Myr (Figure 2.8G). Our model-predicted low FZ strength is also in agreement with the Behn (2002) estimate for 5% coupling across active TFs. We suggest that FZs are likely initially very weak due to intense deformation within the active TF and extensive alteration of upper mantle rocks by circulation of hydrothermal fluids.

2.5.2 The role of upper mantle alteration products in fracture zone strength

Fracture zones and transform faults likely host brittle deformation that extends into mantle rocks (Kirby, 1983; Roland et al., 2010), providing possible pathways for fluids and consequent alteration of peridotite (Bonatti and Honnorez, 1976; Dick, 1989; Cannat and Seyler, 1995; Detrick et al., 1993; Rüpke and Hasenclever, 2017). For example, within

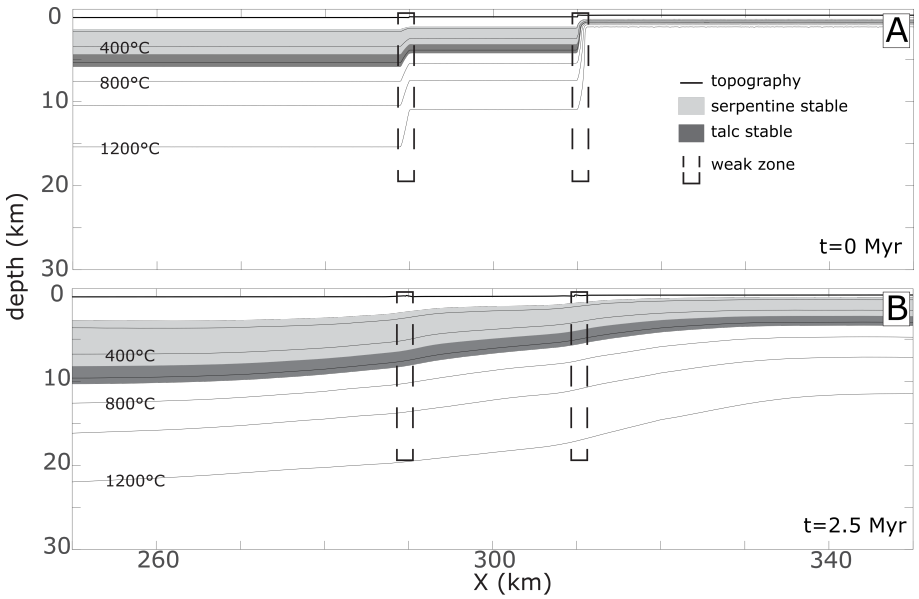

Figure 2.10: Serpentine (light gray) and talc (dark gray) stability fields calculated from Winter (2001) overlaid on modeled isotherms for model case 1 at (A) the initial condition and (B) 2.5 Myr model time. Imposed weak regions are indicated by heavy dashed lines. A majority of the lithosphere above the brittle-ductile transition (700°C isotherm) lies within the stability fields. If the imposed weak zones represent faulted and permeable material, fluid flow in these regions will promote alteration to weaker materials and provide the strength reduction required to generate reverse tilt features.

the active Gofar TF low seismic velocities extend up to 9 km depth (Roland et al., 2010), consistent with enhanced porosity (brittle deformation) and possible alteration of mantle rocks. Fluid circulation may be partly responsible for altered rocks recovered from many TFs; serpentinites have been recovered from the Kane (Karson and Dick, 1983), Fifteen-Twenty (Rona et al., 1987; Escartín et al., 1999), Vema (Bonatti and Honnorez, 1976), and Garrett (Bideau et al., 1991) TFs, while talc has been documented at the Fifteen-Twenty (Bach et al., 2004), St. Paul (D'Orazio et al., 2004), and Conrad (D'Orazio et al., 2004) TFs. Furthermore, heat flow observations within the Ecuador FZ (Kolandaivelu et al., 2017) indicate active hydrothermal circulation in both ponded sediments and the underlying basement rock of the FZ.

Alteration of upper mantle rocks may significantly reduce FZ strength and permit the formation of reverse tilts of ITSC blocks. Although values for the apparent coefficient of friction predicted by our analytical and numerical models are not directly comparable, as the analytical model assumes a discrete slip surface and the numerical model simulates a 2 km-wide shear zone, both models predict that reverse tilts require very small values ($\mu_a < 0.01$), an order of magnitude lower than experimental values from altered peridotite coefficients of friction (μ=0.1 for serpentine or talc, Moore and Lockner (2011)). In our models, serpentine and talc would be stable over large, overlapping depth ranges (1–7 and 5–11 km, respectively, Winter (2001)), and well into the mantle (Figure 2.10), providing a mechanism that might contribute to the weak FZs predicted by our results.

2.5.3 Pore fluid pressure

Model-predicted apparent coefficients of friction suggest an additional mechanism besides alteration is required to weaken fracture zones and allow for thermally generated buoyancy forces to rotate the interior block. By decreasing the effective normal stress across FZs, pore fluid pressures could reduce their frictional strength (Beeler et al., 2000) and permit slip at lower yield stresses. This reduction in yield stress would generate the same net effect of lowering the apparent coefficient of friction (μ_a) in our models. Assuming a coefficient of friction μ=0.1 (lower limits of serpentine or talc, Moore and Lockner (2011)), pore fluid pressures approaching lithostatic values are sufficient to achieve an apparent coefficient of friction of μ_a <0.01, consistent with our model results. Increases to pore fluid pressure could occur due to confinement and high pressures associated with compression across the FZ after a change in plate motion. Indeed, rotation poles (Rowan and Rowley, 2014) predict both Clarion and Murray FZs would have been in tectonic compression early in their evolution. Additionally, the reduction of pore volumes during serpentinization (Zhu et al., 2016) could enhance fluid confinement and overpressures.

Our numerical model does not include pore fluid pressures in our yield criterion formulation, but predicted apparent friction coefficients are consistent with the combination of alteration and poroelastic effects, potentially aided by tectonic compression. In future studies, a more detailed consideration of combined alteration and poroelastic effects on FZ strength should be considered.

2.5.4 Segmented fracture zones host large regions of alteration products

We are limited in our ability to simulate where deformation may promote fluid circulation and alteration by the 2-D nature of our simulations, but the above stability field calculations suggest that altered peridotite could exist in our modeled FZs. Recent results from a 3-D thermomechanical model of a TF suggest that alteration stability fields in a 100 km-long TF can reach 25 km in width (perpendicular to the TF) (Roland et al., 2010); widths much greater than the weak zones in our models. At Clarion, where FZ separation is typically 20 km, the predicted stability zones from Roland et al. (2010)) for each FZ would overlap, indicating that a large fraction of the mantle rocks underlying this segmented FZ could have undergone extensive alteration. At Murray, where the FZ separation is larger, alteration within 25 km of the FZs would cover over half of the ITSC block regions. Taken together, the possibility of pore fluid influences on the strength of altered peridotite and our model results indicate that segmented FZs could be broad regions of extensive upper mantle alteration.

If segmented FZs are regions of enhanced alteration, they will carry greater volumes of hydrated minerals (relative to normal oceanic lithosphere) into the mantle at subduction zones and alter the composition of erupted lavas. Manea et al. (2014) modeled subduction of a single serpentinized FZ and linked overlying variations in B/Zr ratios in volcanic arcs to the enhanced fluid flux from the subducting FZ. Similarly, enhanced boron con-

centrations in lavas erupted in the Aleutian arc overlying the subducting Amlia FZ are thought to be a result of the enhanced fluid contents (Singer et al., 2007). Likewise, melt inclusions at Mt. Shasta have high H_2O contents, which have been linked to subduction of the Blanco TF (Ruscitto et al., 2011). Subduction of a segmented FZ may increase fluid flux into the mantle by several times relative to an unsegmented FZ and impact overlying volcanic processes. Further work is needed to assess the volumes of hydrated minerals likely to subduct and their role on volcanic processes.

2.5.5 Fracture zone topography as an indicator of past tectonic stress

Our results provide several kinematic indicators of past plate motions. Scarp reversal features are indicative of transpressive motions across a FZ and reverse tilts correspond to compression across the FZs. These observations may be used to constrain periods of transpression across FZs where other constraints are not available.

At the Clarion and Murray FZs, predicted changes in plate motion likely caused separate periods of extension and compression along the both the active TF and the young parts of the FZs (e.g., Figure 2.1, 2.4). Consistent with these predictions and those of our theoretical and numerical models, all but the southernmost FZs exhibit reverse tilt and scarp reversal features during periods of compression. Due to the origin of the southernmost FZ at the outermost RTI instead of within the active TF region, it would not experience plate motion-derived compression or tension (e.g., Figure 2.4A). Indeed, the southernmost FZs at Clarion and Murray (Figure 2.1) do not exhibit scarp reversal characteristics.

Based upon the comparison of our model results with details of the Clarion and Murray FZs, we suggest that reverse tilt and scarp reversal features provide a previously unrecognized constraint on the timing and magnitude of changes in relative plate mo-

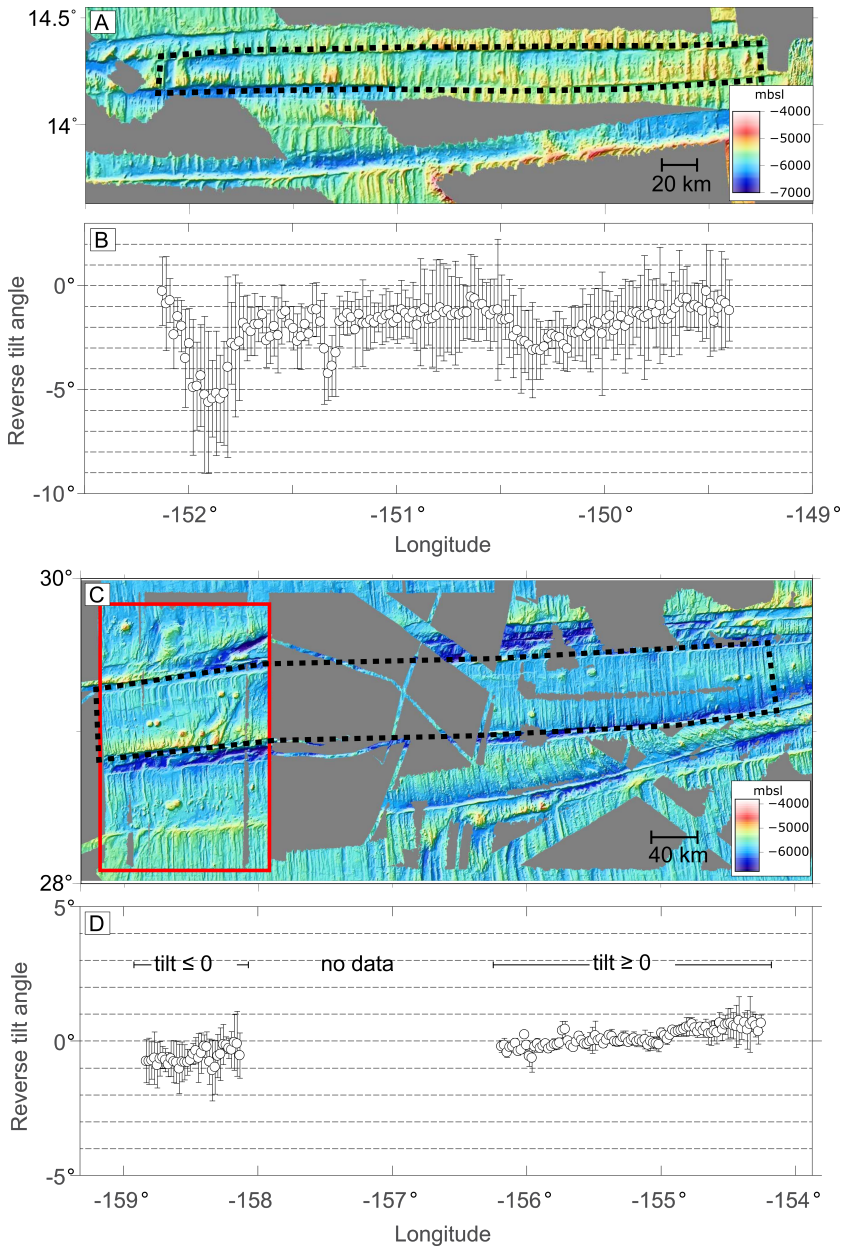

Figure 2.11: At Clarion, the longest uninterrupted section of bathymetry over intra-transform lithosphere (A) shows a reverse tilt (B) that decreases over time. (C) Likewise, the new bathymetric coverage at Murray FZ (red box) reveals reverse tilt features within one intra-transform section. (D) The magnitude of reverse tilt also appears to decrease from west to east in the mapped region. Black dashed lines indicate the intra-transform lithosphere that was used to calculate tilt values. Error bounds on (B) and (D) are determined from the norm of the residuals for a linear fit to each bathymetric cross-section.

tions. The decrease in reverse tilt magnitude over time at both FZs (Figure 2.11) may be an indicator of decreasing compression across the FZs, consistent with re-alignment to a spreading-parallel direction. Such a constraint is particularly valuable during the Cretaceous when magnetic anomalies are unable to provide strong constraints on plate reconstructions. Transpression across an active segmented TF will leave behind distinct anti-symmetric kinematic indicators in the FZs they create: the youngest FZ on either side of the ridge will not exhibit scarp reversals while older FZs will. Additionally, our model results indicate that the magnitude of reverse tilt features correspond roughly to the rate of compression the TF experienced, related to the angle change in spreading direction. In light of these results, collection of further bathymetric data along existing segmented FZs can provide new constraints on changes in tectonic plate motions in regions where magnetic data are unavailable or plate motion models are poorly constrained, especially in the Cretaceous Magnetic Quiet Zone.

2.6 Conclusions

We present observations and analysis of new bathymetry collected aboard the R/V *Onnuri* and the NOAA Ship *Okeanos Explorer* at the segmented Clarion and Murray FZs, respectively. Bathymetry along the segmented portion of the FZs is inconsistent with predictions from a classical locked fault thermal subsidence model for FZ evolution. Interior blocks dip towards the old side of the FZ (north), up to 2° from horizontal, whereas the locked fault model predicts they should dip towards the young side of the FZ (south). Additionally, scarp relationships are also reversed relative to those predicted by thermal subsidence of the lithosphere, in some cases younger lithosphere lies deeper than older lithosphere across a FZ.

Using a 1-D solution to the equation of thermal diffusion across an ITSC block bordered by FZs, we determine the contribution of thermally-driven rotational torques to

the observed reverse tilts at both FZs. Results of these models suggest that formation of reverse tilts requires the FZ interfaces to be very weak, equivalent to a coefficient of friction of 0.01 on a single, flat slip interface.

To further examine the contribution of thermal diffusion as well as that of tectonic compression and extension due to changes in plate spreading directions, we use a thermo-mechanical 2-D numerical model of a visco-elastic-plastic lithosphere split by two closely-spaced FZs. Numerically, reverse tilts and scarp reversals only form for FZs with depth-averaged yield strength of <3 MPa. Small extension rates imposed across the modeled FZs do not significantly modify the ITSC topography, but larger rates ($> +1 \times 10^{-12}$ m/s) increase positive tilts. In contrast, compression imposed across the modeled FZ enhances total reverse tilt and is required to produce scarp reversal.

Reverse tilts up to 2° are produced in the numerical model by applying tectonic compression commensurate with rotation pole estimates of initially high compression rates followed by a decrease to zero as the TF re-orients. A model with an initial tectonic compression rate of -1×10^{-10} m/s that decreases to 0 m/s over 2 Myr produces 2° of reverse tilt.

The apparent coefficients of friction (μ_a) of 0.01–0.001 predicted for weak FZs by our models are too low to be consistent with serpentine and talc alteration of upper mantle rocks and require an additional mechanism to explain their predicted range. Poroelastic effects due to fluid overpressure in the FZs may be responsible. These results, as well as previous seismic and modeling studies, suggest that reverse tilt and scarp reversal features along FZs likely indicate extensive alteration of mantle rocks and the presence of fluids within FZs. We conclude that segmented FZs may inject large swaths of hydrated lithosphere into the mantle at subduction zones.

Chapter 3: Segmenting Fracture Zones

3.1 Introduction

Oceanic TFs commonly strike parallel to plate motion (Menard and Atwater, 1968; Vogt et al., 1969) and orthogonal to the strike of the adjacent ridge segments (Atwater and Macdonald, 1977). However, many TFs are oblique to plate motion (Taylor et al., 1994) causing trans-pressional or trans-tensional stress regimes that result in characteristic structural and magmatic features. Oblique compressional (trans-pressional) TFs develop a distinct central ridge along their length (e.g., Pockalny, 1997; Maia et al., 2016). Oblique tensional (trans-tensional) TFs develop wide, deep extensional basins that are sometimes cut by en-echelon faults, oblique to the strike of the TF (Taylor et al., 1994). In contrast to many plate motion parallel TFs that are amagmatic (e.g., Cannat and Seyler, 1995), oblique-tensional TFs often exhibit intra-transform volcanism (i.e., a "leaky" transform) (e.g., Menard and Atwater, 1969; Hékinian and Bideau, 1995; Perfit et al., 1996; Wendt et al., 1999). Such "leaky transforms" may organize into a series of en echelon strike-slip deformation zones separated by intra-transform spreading centers (ITSCs), a distinct change in the TF morphology that adds new regions of crustal accretion and alters earthquake distributions (Wolfson-Schwehr and Boettcher, 2019). Hereafter, we refer to this process of a single TF splitting into several strike-slip segments as TF segmentation.

TF segmentation is believed to be one possible response to changing plate motions (Tucholke and Schouten, 1988). The Pacific Fracture Zones (FZs), which formed at fast-spreading, large-offset (500 km) TFs, often "branch" from a single trace into several traces separated by seafloor with a typical abyssal hill morphology (e.g., Croon et al., 2008; Kuykendall et al., 1994; Menard and Atwater, 1968; Menard and Atwater, 1969; Tucholke and Schouten, 1988). Magnetic anomalies, seafloor fabric, and the strike of the

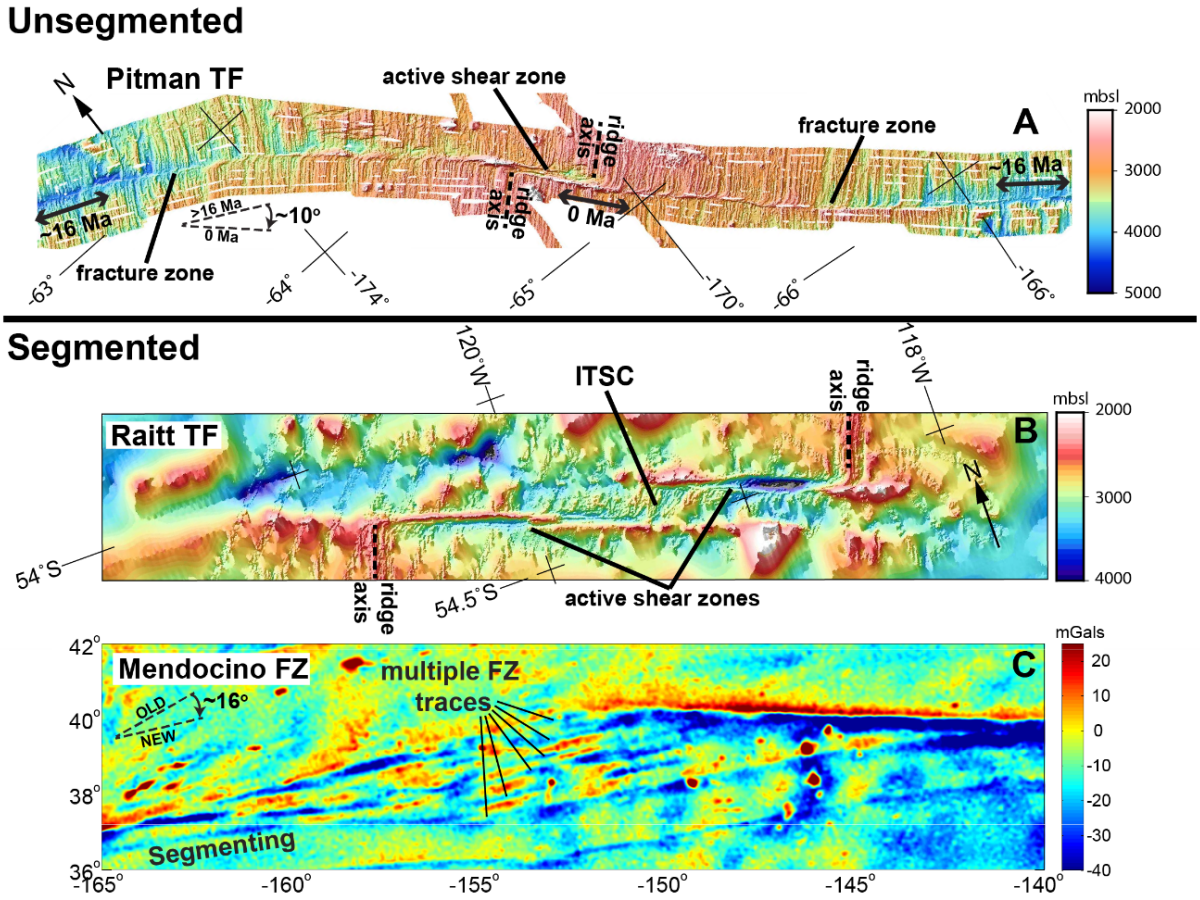

Figure 3.1: Examples of an (A) unsegmented TF (Pitman) that remained parallel to spreading by rotating (double arrows, 10°change), (B) an active, segmented TF (Raitt) that formed two shear zones separated by an ITSC (labeled) after a 4°change, and (C) the satellite-derived gravity anomaly (Sandwell et al., 2014) over the Mendocino FZ, which segmented after a 16°change. Bathymetry is from the Global Multi-Resolution Topography Synthesis (GMRT) (Ryan et al., 2009).

FZs indicate that FZ branching occurs after a change in spreading direction (Jordahl et al., 1995; Kuykendall et al., 1994; Menard and Atwater, 1968). Searle, 1983 built upon this idea to suggest that several, smaller offset, segmented TFs along the East Pacific Rise (e.g., Siqueiros, Quebrada, Discovery, and Gofar) branched due to trans-tension after changes in plate motion; the formerly oblique single trace TFs branched into several smaller, spreading parallel transform segments separated by ITSCs. Even though trans-tension appears to cause TF segmentation, the primary controls on how this dynamic process occurs are poorly constrained.

Although observations do not constrain the physical evolution of TFs after a change in plate motion direction (Figure 3.2), several hypotheses exist for trans-tensional TFs: 1) rotating to return to a primarily spreading-parallel orientation (Tucholke and Schouten, 1988); 2) slow widening of the original TF and formation of a rhombochasm or overlapping spreading center (Dauteuil et al., 2002; Geli, 1997; Menard and Atwater, 1968; Menard and Atwater, 1969); 3) enhanced magmatic accretion on inside corners of ridge-transform intersections (RTIs) leading to TF rotation (Gerya, 2013); and 4) creation and/or propagation of ridge and transform segments to form smaller, spreading parallel transform segments separated by actively spreading ITSCs (McCarthy et al., 1996; Searle, 1983; Tucholke and Schouten, 1988). Based upon their detailed study of the Kane FZ, Tucholke and Schouten, 1988 hypothesized that TF branching only occurs for rotations in the plate motion direction that are rapid and large enough that a new spreading-parallel TF could not be accommodated within the already existing transform valley.

For both trans-pressional and trans-tensional TFs, few constraints exist on the time scales required to adapt to plate-motion changes. Pockalny (1997) suggest that trans-pressional TFs should completely re-orient over a time equal to 1/2 the age offset of the TF. Alternatively, other workers conclude that adjustment to plate motion changes should be geologically instantaneous (e.g., Collette, 1974; Menard and Atwater, 1968).

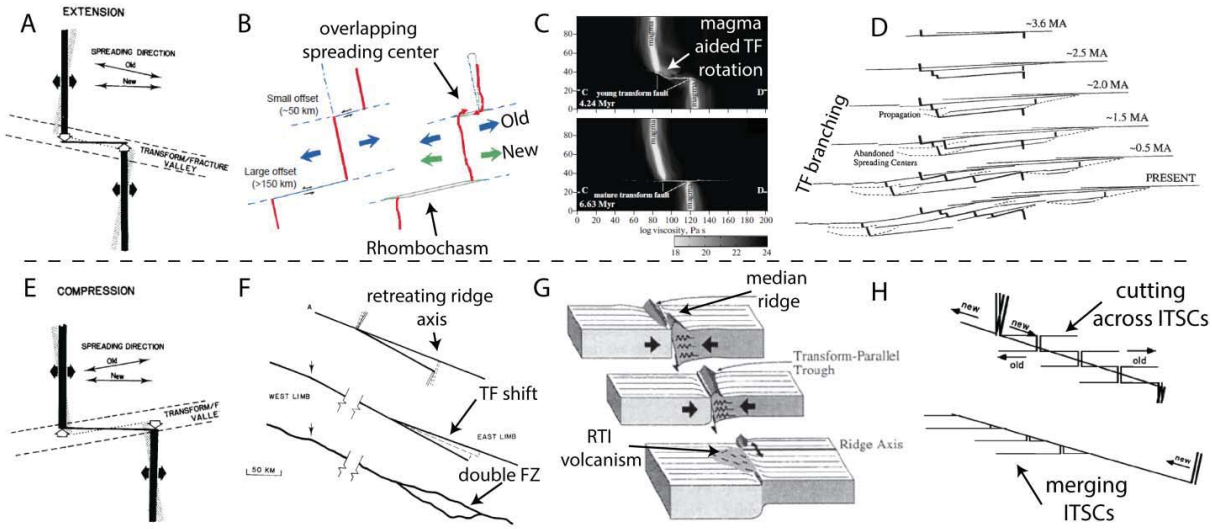

Figure 3.2: After a change in plate motion direction, tran-tensional TFs are hypothesized to (A) rotate if a change can be accommodated within the existing TF valley (Tucholke and Schouten, 1988), (B) slowly widen and form a rhomobochasm or OSCs due to ridge propagation (Menard and Atwater, 1968; Geli, 1997), (C) rotate by magmatic accretion on the inside corners (Gerya, 2013), and (D) branch into several transform segments separated by ITSCs (Searle, 1983; Pockalny, 1997). Trans-pressional TFs are hypothesized to (E) rotate if a change can be accommodated within the existing TF valley (Tucholke and Schouten, 1988), (F) shift to a new location by propagating through older crust and ridge axes retreat (Tucholke and Schouten, 1988), (G) form a median ridge to accommodate compression (Pockalny, 1997), and (H) if already segmented to shear through the existing ITSCs or for the ITSCs to slowly merge into one TF (McCarthy et al., 1996)

Observations at the Clarion FZ (Morrow et al., 2019) show a reduction in number of TF strands and ITSCs over 15 million years. It is unclear from observations how long TFs require to adjust to changes in plate motions, a process which is likely impacted by spreading rate, rheology, and magmatism.

Here, I present a compilation of TF and FZ measurements and comparisons between TF morphology and past plate motions, with the goal of characterizing the primary influences (rheology, magmatism, etc.) on TF morphology during and after an opening (transtensional) change in spreading direction. I use this compilation to infer the conditions that lead to the oblique TF morphologic responses (A-D, Figure 3.2) described above. In particular, I aim to determine the primary tectonic and magmatic controls that define when a TF will segment into multiple strike-slip offsets as opposed to accommodating a change in plate motion via another mechanism.

3.2 Factors affecting transform fault response to changes in plate motion

3.2.1 Spreading rate

Several TF characteristics, including length and predicted mechanical coupling, are a function of spreading rate. In addition to tension or compression imposed by plate motion obliquity, spreading rate at a TF will affect the stresses, and thus the deformation, along the fault and in the neighboring lithosphere (e.g., Behn, 2002). No TFs currently exist at the fastest (>145 mm/yr) (Naar and Hey, 1989) or at the slowest (<20 mm/yr) spreading rates (Dick et al., 2003). Along the slow-spreading Mid-Atlantic Ridge (MAR), where the axis is relatively cool and strong, TFs are commonly shorter (50 km) than along the fast-spreading East Pacific Rise (EPR) (100s of km) (Fox and Gallo, 1984). Indeed, it is suggested that higher strain rates and thinner lithosphere at fast-slipping TFs may

promote complex, temporally unstable TF geometries (Fox and Gallo, 1984), including segmented TFs.

3.2.2 Rheology

The rheology of the oceanic lithosphere is strongly temperature-dependent and, thus, the overall strength of a TF is believed to be a function of its thermal structure (e.g., Gregg et al., 2006; Behn et al., 2007). Early numerical models calculated the flow of a constant viscosity mantle beneath a TF (Morgan and Forsyth, 1988). This simplified rheology yields a lithosphere that is warmest and thinnest at RTIs. In contrast, using a model with a strongly temperature-dependent mantle viscosity and brittle deformation of the crust, Behn et al. (2007) concluded that the opposite was true; they predicted the thinnest and warmest sub-transform lithosphere to be beneath transform centers. Extending the model of Behn et al. (2007) by including the effect of hydrothermal cooling, Roland et al., 2010 concluded that the isotherms beneath TFs are likely to be nearly flat, consistent with seismicity from both segmented and unsegmented TFs including the Blanco, Chain, Kane, Orozco, Quebrada-Discovery-Gofar, and Romanche TFs (Abercrombie and Ekström, 2001; Braunmiller and Nábělek, 2008; Roland et al., 2012; Tréhu and Purdy, 1984; Wilcock et al., 1990). If segmentation and spreading initiate within a TF valley, they will likely focus at the weakest (and possibly warmest) location along the TF trace.

3.2.3 Magmatism

Magmatism likely also plays a role in TF rheology, especially at oblique, opening mode TFs where melts may pool from up to 100 km away (Gregg et al., 2009). Intra-transform magmatism is hypothesized to alter the rheology of TF lithosphere in at least two ways: 1) repeated penetration of relatively cool lithosphere by warm magma will thermally weaken the lithosphere (e.g., Mittelstaedt et al., 2008; Mittelstaedt et al., 2011), and 2) magmatic events with a low temporal frequency will provide time for magma to cool and

may form a weld that will locally strengthen a section of a TF (Fornari et al., 1989). The more dominant of these two scenarios will depend partly upon the magma flux to the TF. The magma flux to a TF can be estimated by comparing crustal thickness within the TF to that of the nearby ridge axis. Indeed, gravity inferred crustal thicknesses are greater than average along several intermediate- and fast-slipping TFs such as the Siqueiros and Garrett TFs (Gregg et al., 2007). For example, the fast-slipping Quebrada-Discovery-Gofar area along the EPR has positive gravity anomalies in some areas that indicate thin or denser than average crust (Pickle et al., 2009). At slow spreading ridges, studies of unsegmented TFs such as the Kane, Oceanographer, and Vema TFs, commonly find thin or absent crust (Bryan, 1981; Detrick and Cormier, 1982; Kuo and Forsyth, 1988; Sinha and Louden, 1983). The observed differences in magma supply to TFs may yield a variable influence of intra-transform magmatism on TF evolution. Introducing magmatically-accommodated spreading within a TF that originally hosted no ITSC will alter the thermal structure and mechanical strength of the fault.

3.2.4 Thermal stresses and coupling across transform faults

Since early interpretation of TFs as thermal contraction cracks in the lithosphere (Turcotte, 1974), the influences of thermal stresses on TFs have been well studied. Thermal stresses due to contraction of the oceanic lithosphere as it cools and moves away from a ridge axis (e.g., Choi et al., 2008) also likely contribute to TF stresses. The component of thermal stresses parallel to plate motion is likely accommodated by normal faulting at the ridge axis, with the remaining thermal contraction causing a ridge-parallel tension to develop in the plate (e.g., Turcotte, 1974; Sandwell, 1986). Thermal stresses will increase tension perpendicular to trans-tensional oblique TFs, but somewhat lessen compression perpendicular to tran-pressional oblique TFs; the magnitude of these changes, however, will depend upon factors such as the TF age offset, length, and spreading rate.

Transform fault coupling likely plays an important role in responses to changing plate motions. Using a numerical model of a ridge-transform-ridge system, Behn (2002) compared model predicted fault planes to observed normal and oblique faults at TFs and concluded that transforms are only 5% coupled. The conclusion of weak TFs is supported by observations showing that the global seismic moment release along oceanic TFs only accounts for 15% of plate motions, thus, 85% of motion across TFs is accommodated by "quiet" aseismic slip and creep events, an indication of low mechanical coupling (Boettcher and Jordan, 2004). Segmentation divides the seismogenic zone of a TF (Wolfson-Schwehr and Boettcher, 2019), but it is unclear how much this division alters total coupling across the TF.

3.3 Methods

To constrain the relationships between TF segmentation and changes in plate motion, I measure the length, number of FZ traces, and obliquity of 38 TFs along active spreading ridges (15 segmented, 23 unsegmented). TF obliquity is measured as the angle between the relative plate motion vector and the strike of the great circle connecting the RTI; positive and negative obliquities indicate trans-tension and trans-pression, respectively. Transform length is taken as the great circle distance between (Figure 3.3, inset). RTI locations were selected by projecting a great circle along the adjoining MOR segment (at the axial high, in the case of fast-spreading ridges, and the center of the axial valley in the case of slow-spreading ridges) and the strike-slip segment (determined as the linear center valley of the strike-slip deformation zone).

Using published plate motion data (Tucholke and Schouten, 1988; Searle et al., 1993; Lonsdale, 1994; Tebbens and Cande, 1997; Pockalny, 1997) and isochron observations (Müller et al., 2008), I also measure relative changes in FZ and TF obliquity over time. For each FZ, I use available high-resolution and satellite-derived bathymetry (GMRT Ryan

et al. (2009)) to determine the change in FZ azimuth, measured as a great circle along the deepest trace of the FZ. Where published changes in plate motion are not available, changes are approximated as the minimum azimuth change of magnetic isochrons before and after the FZ segments. The minimum change region is bounded by the earliest indication of widening within the FZ and the earliest indication that widening between adjacent FZs ceases.

A stable, unsegmented TF is typically sub-parallel to spreading and has a transform domain (i.e., all transform parallel structures, including the transform valley) 10-40 km wide (Fox and Gallo, 1984). After a change in relative plate motion direction (or during, depending on the duration of the change), the TF will initially be oblique to the new spreading direction; this angular change in plate motion direction must be accommodated by the TF (i.e., the TF must re-orient to spreading parallel). To quantify the necessary TF reorientation, or accommodation, after a plate motion change, I define a predicted accommodation length as the tangent of the angular change in plate motion multiplied by the transform length (i.e., the approximate distance one end of a TF must rotate to align with a new spreading direction assuming the other end is fixed, Figure 3.5, inset). When measuring a FZ instead of an active TF, I take the original TF length as the FZ-parallel great circle distance corresponding to the offset of a single isochron across the FZ (Müller et al., 2008). After the TF structure reaches a new equilibrium (i.e., the FZ is parallel to plate motion), I measure the observed accommodation length (i.e., the total spreading perpendicular width of the new transform domain). When measuring the observed accommodation length, a FZ with several traces (e.g., Mendocino; Figure 3.1) or a TF with several segments are considered part of one TF system if they are $<$50 km apart (e.g., Wolfson-Schwehr and Boettcher, 2019). I measure width at FZs as the distance separating the outermost strike slip traces (defined by their deepest trace on the seafloor). I separate Molokai FZ into two different measurements (Maui and Oahu traces)

based on observations suggesting that the Molokai FZ represents two segmented FZs that are relatively close, but kinematically distinct from each other (Searle et al., 1993).

3.4 Results

Measurements for 38 TFs and FZs (Table 3.1) show a critical range where segmented and unsegmented overlap. No un-segmented TFs exist for obliquities >3.8° and no segmented TFs for obliquities <1.4°. Additionally, TFs with more segments are longer and often more oblique to spreading direction. There is not a clear distinction between the two populations in overall TF length.

Angular opening rate measurements also divide segmented and unsegmented TFs and FZs. In the collected data, all TFs subjected to an opening change in relative spreading direction (hereinafter opening rate) faster than 0.91°/Myr segmented; TFs that experienced an opening rate slower than 0.80°/Myr did not segment 3.4. TFs that experienced opening rates of 0.80-0.91°/Myr (Kane, Heezen, Raitt, Tharp, and Udintsev) sometimes segmented, and sometimes accommodated the change in other ways (e.g., rotation). Interestingly, over this narrow range of rates (0.80-0.91°/Myr), the span of total angular change in plate motion direction is large (4° up to 30°) with no relationship to segmentation.

Accommodation length measurements show a separation between segmented and unsegmented TFs and FZs 3.5. Segmented TFs have similar predicted and observed accommodation lengths, with values falling approximately along a 1:1 line, while unsegmented TFs have observed accommodation lengths that are smaller than predicted (above the 1:1 line).

3.5 Discussion

As plate motion changes in an opening sense across a TF, the primarily strike-slip region within the principal transform deformation zone (the immediate ∼10–20 km re-

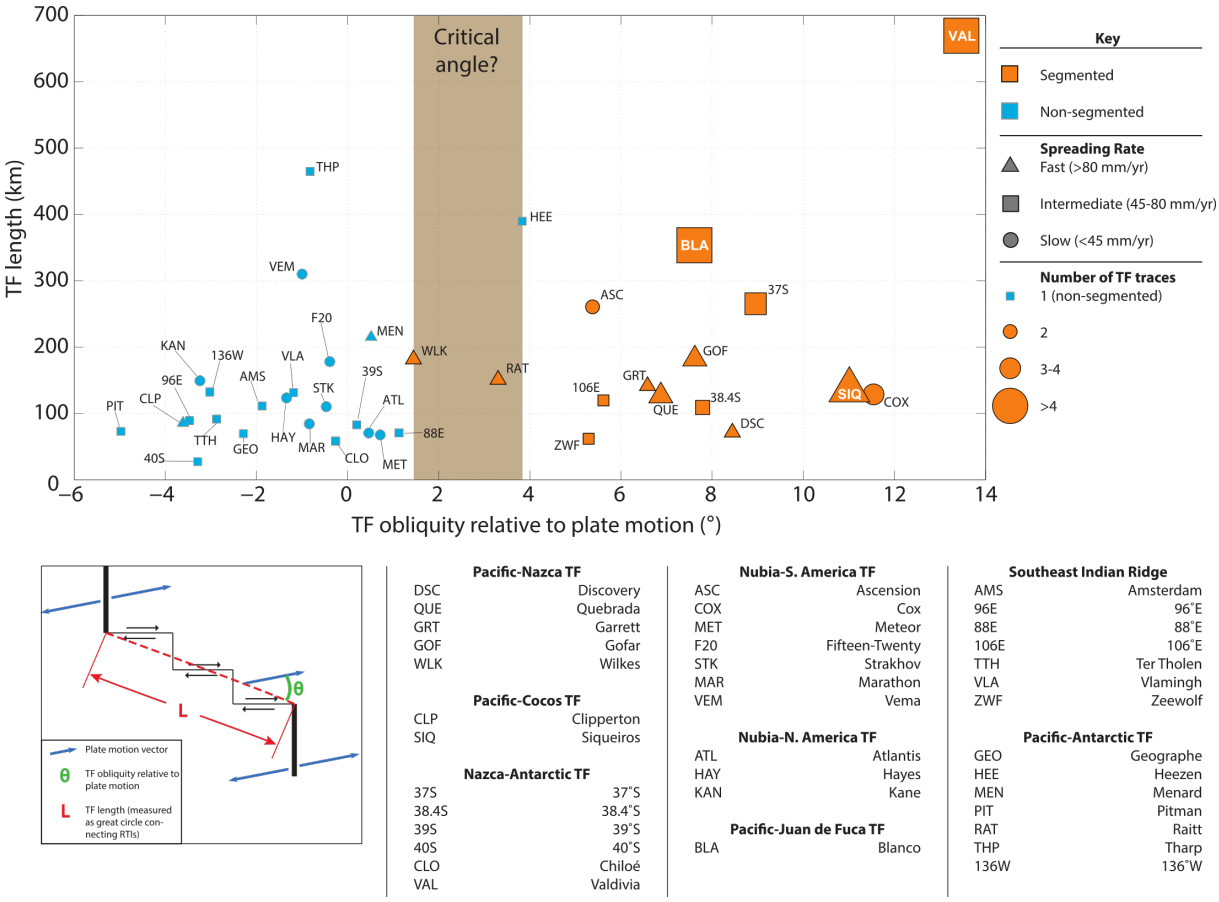

Figure 3.3: Measurements show segmented TFs are >1.4° oblique to plate motion and non-segmented TFs are <3.8° oblique to plate motion, suggesting a critical angle for TF segmentation. In general, TFs with more segments (symbol size) are longer or more oblique. Here, obliquity and TF length is measured from (inset) ridge tip to ridge tip for the 38 measured TFs.

Table 3.1: Active transform fault obliquities

TF/FZ	Fault length (km)	Obliquity (°)	No. of ITSCs
106°E	119.85	5.62	1
Hayes	123.50	-1.34	0
Meteor	67.80	0.72	0
38.4°S	109.03	7.80	1
37°S	264.81	8.96	3
39°S	83.04	0.20	0
40°S	27.48	-3.29	0
43°S	58.54	-0.26	0
88°E	70.85	1.13	0
96°E	89.32	-3.47	0
Amsterdam	111.49	-1.88	0
Ascension	260.80	5.38	1
Atlantis	70.79	0.47	0
Blanco	353.49	7.61	4
Clipperton	85.23	-3.61	0
Cox	128.94	11.54	2
Discovery	72.32	8.44	1
Fifteen-Twenty	178.18	-0.39	0
Geographe	69.83	-2.29	0
Gofar	184.77	7.62	2
Garrett	142.32	6.58	1
Heezen	389.85	3.83	0
Kane	149.45	-3.24	0
Marathon	84.43	-0.84	0
Menard	214.90	0.52	0
136°W	132.53	-3.02	0
171°W	73.11	-4.97	0
Quebrada	129.18	6.87	3
Raitt	151.74	3.30	1
Siqueiros	141.85	11.01	4
Strakhov	110.40	-0.47	0
Tharp	465.02	-0.82	0
Ter Tholen	91.68	-2.87	0
Valdivia	669.49	13.47	8
Vema	310.34	-1.00	0
Vlamingh	131.56	-1.19	0
Wilkes	182.47	1.44	1
Zeewolf	62.04	5.29	1

TF fault measurements from GMRT synthesis (Ryan et al., 2009), plate motions from DeMets et al. (2010).

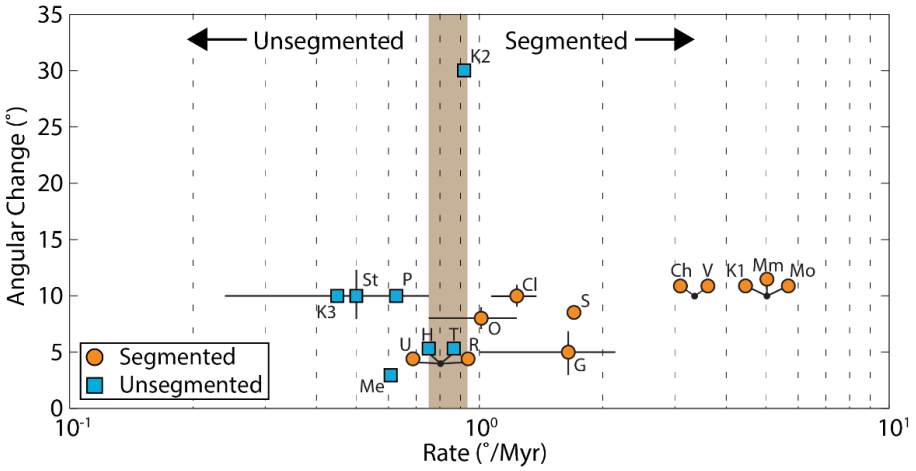

Figure 3.4: A critical rate of change in plate motion direction is necessary to segment TFs (vertical, brown bar). This data supports the hypothesis of Tucholke and Schouten (1988) that TFs will rotate, instead of segmenting, for slow or small changes in the direction of plate motion. Rates of change (note the log scale) are from the references in table 3.2 or measured as the change in magnetic isochron azimuth divided by the time between isochrons. Error bars on rates are estimated by an increase or decrease in the time to change plate motion direction by one additional isochron or by published uncertainties where historical motions are used. For cases with a succession of small changes (e.g., Cande et al., 1995) we plot the sum of changes over the total time period. Included TFs and sources include: K1, K2, K3 – Kane FZ during the Cretaceous Magnetic Quiet Zone (CMQZ), from the CMQZ to chron 25, and from chron 6 to present (Tucholke and Schouten, 1988); S – Strakhov TF; Cl – Clarion FZ; Mo, Mm – Molokai FZ Oahu and Maui strands (Searle et al., 1993); R – Raitt TF, H – Heezen TF, T – Tharp TF, U – Udintsev TF (Lonsdale, 1994); O – 106°E TF, Southeast Indian Ridge; G – Garrett TF; V – Valdivia TF, Ch – Chiloe FZ (Tebbens and Cande, 1997); P – Pitman TF (Cande et al., 1995); Me – Menard TF (Croon et al., 2008); S – Siqueiros TF (Pockalny, 1997).

Table 3.2: Transform fault and fracture zone opening rates

TF/FZ	Length (km)	Angular change (°)	Rate °/Myr	Pred. opening (km)	Obs. opening (km)
Kane FZ[1]	160	10	0.455	27.784	4
c6-present Strakhov[1]	208	10	0.5	36.119	20
c18-present Kane FZ[2]	150	30	0.910	75	18
CMQZ to c25 Clarion FZ[1]	250	10	1.25	43.412	70
c34 Kane FZ[2]	158	10	5	27.436	20
CMQZ Molokai FZ[3]	530	10	5	92.034	100
Oahu trace c34 Molokai FZ[3]	70	10	5	12.155	18
Maui trace c34 Raitt[4]	145	4	0.8	10.115	8
Heezen[4]	380	4	0.8	26.507	10
Tharp[4]	480	4	0.8	33.483	10
Udintsev[4]	320	4	0.8	22.322	15
106°E[1]	80	8	1	11.134	14
Garrett[1]	130	7	2.333	15.843	15
Valdivia[1]	695	10	3.333	120.685	126
Chiloe FZ[1]	86	10	3.333	14.934	18
Guafo[1]	275	10	3.333	47.753	45
Pitman[1]	87	10	0.625	15.107	8.8
Menard[5]	223	3	0.6	11.671	6
Siqueiros[6]	130	8.5	1.7	19.215	21

[1] Measured from GMRT Synthesis (Ryan et al., 2009) and seafloor age map (Müller, 2008)
[2] Tucholke and Schouten (1988)
[3] Searle et al. (1993)
[4] Lonsdale (1994)
[5] Cande et al. (1995)
[6] Croon et al. (2008)

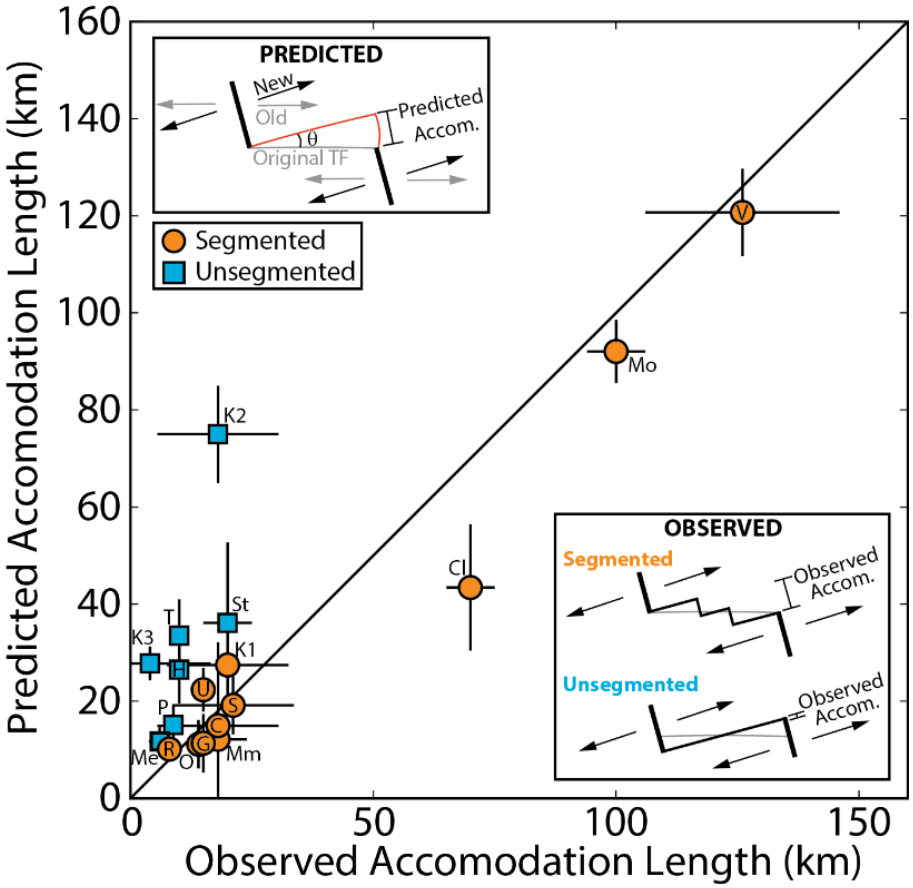

Figure 3.5: Observed versus predicted accommodation length for (orange circles) segmented and (blue squares) unsegmented TFs and FZs. Predicted length is calculated as the tangent of the angular change in plate motion direction multiplied by the TF length at the time of the change (inset, upper left); where published TF lengths are unavailable, we use the mean offset across the FZ of the two isochrons bounding the period of interest (Müller et al., 2008). Observed length is measured as the mean width of the transform system (inset, lower right) after a change in plate motion direction. Where published changes in plate motion direction are unavailable, the angular change is taken as the difference in FZ strike before and after a plate motion change. Estimated errors for the above measurements and calculations are determined by uncertainties in plate motions. Colors and abbreviations are as in Figure 3.4.

gion surrounding the strike-slip trace of the TF) experiences a TF-perpendicular opening component. Transform faults that segment appear to do so under a limited range of transtensional (opening) conditions. Our findings indicate that segmented TFs exist only when a single TF connecting ridge tips would have to be >4°oblique to plate motion, implying that excessively-oblique TFs are not stable. However, large changes in plate motion direction (up to 30°) have been accommodated without segmentation (Figure 3.4). The opening rate across a TF appears to be a stronger predictor of TF segmentation than the magnitude of total opening. Our observations provide quantitative constraints on the Tucholke and Schouten (1988) hypothesis, that the magnitude (>4°) and rate (>0.9° Myr^{-1}) of opening are first order determining factors for TF segmentation, and suggest that rate of opening is the primary control. Magnitude and rate of opening conditions control the style of TF response to changing plate motion (Figure 3.2D versus A-C). Within the limited overlapping ranges in Figure 3.3 and 3.4, additional controls may influence the preferred response to changing plate motions.

Transtensional opening across a TF is accommodated by extension and, in the early stages of opening, oblique normal faulting around the TF (e.g., Mittelstaedt et al., 2012). Continued extension likely leads to decompression melting beneath the TF, melts that will ascend and presumably form an ITSC under the right conditions. Propagating melts to the surface requires sufficient melt volumes to form an effective pathway, and thus there may be a critical amount of melt production required to induce formation of a spreading center within a TF valley. Since melt production and ascent occur on relatively short timescales compared to changes in plate motions, there may be a relationship between opening rate, the rate of melt production and extraction, and some critical amount of melt supply to form an ITSC. Repeated penetration by melts warms the lithosphere and focuses deformation (e.g., Mittelstaedt et al., 2011), potentially leading to the formation of a spreading center. Without a critical opening (and thus extensional) rate, insufficient

melt is produced and does not form a connected extraction network, and may not serve to focus deformation and initiate spreading. Alternatively, the rate of plate motion rotation may exceed the TFs ability to shift and accommodate the new spreading direction. Thus, ITSC formation may out-pace the TF's adjustment rate, leading to segmentation.

Ridge tip and TF trace propagation or retreat likely exerts a significant control on TF segmentation. Accommodation measurements (Figure 3.5) indicate that segmented TFs accommodate nearly the entire change in relative plate motion direction by forming new transform segments separated by ITSCs or pull apart basins, while unsegmented TFs were able to rotate or to break through the crust to establish a new, single segment TF parallel to spreading. TFs that did not segment do not widen significantly 3.5, suggesting that the accommodated opening motions are taken up by ridge propagation and TF rotation or diffuse extension outside the TF domain. This distinction separates two different modes of accommodation, implying a balance where creating new strike slip offsets and spreading centers becomes a more favorable accommodation mode than propagating existing ridge tips. For example, the Clarion FZ undergoes two changes in plate motion near the end of the late Cretaceous, one opening and one closing (Morrow et al., 2019). The opening change is accommodated by segmenting, while the closing change occurs concurrently with significant lengthening of the TF ($\sim$100 km offset to $\sim$400 km offset). Although the comparison between an opening and a closing change is a limited comparison, propagating ridge tips during the closing motion and not during the opening motion may be a function of the rate of opening and closing.

In a simplified crack propagation model, crack propagation is always favored in thinner or weaker regions of material (Griffith, 1921). Formation of an ITSC by propagation (ignoring the initial formation process) from within the PTDZ outwards into oceanic lithosphere will likely always be energetically favorable over propagating ridge tips into older lithosphere at the edges of the same TF. Griffith's fracture theory (Griffith, 1921)

and subsequent Linear Elastic Fracture Mechanics (LEFM) approximations indicate that crack propagation is dependent on the ambient stress field. Older lithosphere will have a higher integrated lithostatic pressure (strength) in the brittle deformation zone due to its increased thickness. However, dike propagation theory (Buck, 2006) also postulates that propagation only occurs so long as there is sufficient magma supply to drive overpressure in the propagating dike. Treating a propagating mid-ocean ridge (or ITSC) as a single crack-propagating dike is a significant over-simplification, but the underlying principles may be the same. The relatively robust magmatic system at a ridge tip may meet the supply needs for propagating the ridge tip and reorienting a TF during a change in plate motion until sufficient oblique extension yields a robust magmatic supply within the TF that can supply a crack-propagating overpressure. At that time, it will be more energetically favorable to propagate ITSCs into younger lithosphere and segment a TF instead of rotating the TF and propagating ridge tips at ends of the TF. Thus, the rate of extension may control magmatic production and mode of TF response to changing plate motion (e.g., Tucholke and Schouten, 1988). A detailed model that accounts for melt generation and transport is required to further investigate this hypothesis.

3.6 Conclusions

TF segmentation does not appear to depend upon the maximum magnitude of a change in plate motion direction, but likely requires a minimum value. There may be a threshold rate of change of plate motion direction (0.75-0.95°/Myr) beyond which TFs will segment. Near this threshold value, rheology, local structure, and/or magmatism, may determine if segmentation develops. TFs that segment accommodate nearly all the angular change in plate motion direction through development of new transform segments separated by small pull apart basins or ITSCs, with minimal ridge propagation from the original ridge-transform intersections. Unsegmented TFs accommodate changes

in plate motion direction by rotation or possibly by breaking through existing crust to form a new, single-segment transform that is parallel to spreading, resulting in observed accommodation lengths that are smaller than predicted accommodation lengths.

Chapter 4: Visco-elastic-plastic Models of Transform Faults in 3-D

4.1 Introduction

Transform faults are first order features of Earth's mid-ocean ridge system. Transform faults are consistently nearly parallel to seafloor spreading direction and very often orthogonal to adjacent spreading centers. In fact, the orthogonal relationship between TFs and MORs is so prevalent in natural systems across a wide range of spreading rates and ridge morphologies, that is has been considered an intrinsic property of divergent boundaries (e.g., Oldenburg and Brune, 1972). Despite being a fundamental feature of mid-ocean ridges, the origins of orthogonal ridge-TF spreading patterns are poorly understood. Some researchers attribute their formation to inherited structures from continental breakup (e.g., Behn and Lin, 2000), while others suggest the pattern is an emergent property of the oceanic lithosphere (e.g., Gerya, 2010b). These hypotheses arise from observations as well as analog and numerical models of TF initiation and spreading center evolution.

Early analog models characterize the formation of TF offsets in paraffin waxes or sand and putty. For example, in experiments using cooling paraffin wax as an analog for the Earth's lithosphere, TFs nucleated spontaneously along pre-existing spreading centers (Oldenburg and Brune, 1972). Formation of an orthogonal TF pattern was restricted to waxes with relatively high ratios of tensile strength to shear strength (Oldenburg and Brune, 1975; Freund and Merzer, 1976). Microstructures in the waxes where TFs formed were optically anisotropic, supporting a physical mechanism for relatively weak shear strength that was not present in waxes where TFs failed to form (Freund and Merzer,

1976). Based upon the presence of anisotropy in the above wax experiments, observations of seismic anisotropy in the upper mantle were taken to indicate that the oceanic lithosphere shares this same anisotropic strength relationship (Freund and Merzer, 1976). Subsequent investigations (Shemenda and Grocholsky, 1994; Ragnarsson et al., 1996; Katz et al., 2005) attempting to reproduce Oldenburg and Brune's [1972] work or investigating other ridge structures (microplates, in Katz et al. (2005)), have varying success producing an emergent orthogonal ridge-TF pattern, suggesting that an underlying essential physical characteristic of Oldenburg and Brune (1972) original models is still not well understood. Recently, experiments in colloidal aqueous dispersions produced orthogonal TFs at scales corresponding to Earth materials with an evolving visco-elastic rheology (Sibrant et al., 2018).

Experiments employing a layer each of sand and putty have also been used to investigate the formation and evolution of orthogonal ridge-TF systems. Two-layer experiments are designed to simulate brittle (sand) material overlying a viscous mantle (putty). Results from these experiments indicate that orthogonal TF systems form only when a predefined weak zone is initially placed between spreading ridges (e.g., Dauteuil et al., 2002; Marques et al., 2007). Without this weak zone, oblique features emerge linking two spreading centers and preventing orthogonal TF formation. However, unlike the aforementioned wax models, these two-layer experiments do not simulate accretionary processes; no new material is added at the spreading center location over time. While many interpret these models as indicators that TFs must nucleate from an inherited structure or weakness, the comparison to different results in wax models and actively-accreting ridges on Earth may be limited, due to different strain scaling (i.e., TFs in nature experience much larger strains over millions of years, as compared to models).

More recent numerical models suggest additional complex controls on the origin, orthogonality, and evolution of oceanic TFs. Hieronymus (2004), using 2-D models of

seafloor spreading, suggests that weakening the moduli controlling extension (Young's Modulus) at a different rate than that controlling shear (shear modulus) is fundamental to creating the orthogonal ridge-TF geometry. Like early wax models (Oldenburg and Brune, 1975), Hieronymus (2004) also found that TFs must be weaker in shear than the plate is in tension to stabilize TFs. Choi et al. (2008) present one of the first 3-D numerical models with spontaneous TF formation and showed that the interplay between ridge-perpendicular (spreading) stresses and ridge parallel (cooling) stresses controlled the formation of orthogonal TFs, overlapping spreading centers, or oblique connecting ridges. Models by Choi et al. (2008) were limited to early TF formation (<100 kyrs) and did not address long-term stability of orthogonal ridge-TF systems. The Choi et al. (2008) models share a key conclusion with Hieronymus (2004): orthogonal TF formation in elastic materials is dependent on TFs (shear structures) that are mechanically weaker than adjacent ridges (extensional structures).

The first numerical model with stable TF systems simulated the long-term evolution of a single spreading center in 3-D (Gerya, 2010b) using a visco-plastic rheology at ultra-slow to intermediate spreading rates (1.9 to 7.6 cm/year). In these models, a dynamical instability in ridge spreading and accretion eventually grows into an orthogonal ridge-TF offset. Asymmetric accretion drives migration of ridge segments away from the center of the domain, resulting in TF emergence. Building on this work, Püthe and Gerya (2014) explored the dynamic propagation of two ridge segments in a temperature-dependent, visco-plastic rheology. Their results also produced orthogonal ridge-TF systems under a restricted range of several key parameters including spreading rate, damage healing rates, and the effective Nusselt number of the lithosphere.

Recent numerical models show the importance of elasticity to numerical models of long-term lithosphere deformation that aim to simulate specific fault behaviors in the seafloor (Olive et al., 2016). In particular, visco-plastic models ignore elastic lithosphere flexure

and generate normal faulting topography that can be highly spreading rate dependent and sensitive to the size of the model domain (Gerya, 2010a; Püthe and Gerya, 2014). In contrast to these results, observations and additional modeling studies indicate that fault offset, life span, and resulting topography should be independent of spreading rate and dependent only on the thickness of the faulting layer (Lavier et al., 2000; Behn and Ito, 2008; Olive et al., 2014; Olive et al., 2016). Olive et al. (2016) propose that a visco-plastic rheology is not sufficient for simulating the formation and evolution of normal faults in oceanic lithosphere. The extension to transform faults is unclear but considering the similar scale between ridge normal faults and TFs (i.e., brittle features on the order of 10s to 100s of kms), elasticity likely plays a significant role in TF formation.

Here, we present a series of numerical models in visco-elastic-plastic rheologies designed to initiate an orthogonal ridge-TF geometry. The elastic material in our models does not have a preferred strength or weakness in shear (e.g., Hieronymus, 2004; Choi et al., 2008). Our goal is to determine if elastic materials can maintain an orthogonal ridge-TF-ridge structure without being weaker in shear than in tension, and, if so, under what plastic failure criterion. We compare our results to other models of TF formation and evolution (Hieronymus, 2004; Choi et al., 2008; Gerya, 2010b; Püthe and Gerya, 2014) to elucidate physical characteristics responsible for the notable orthogonal pattern of ridges and TFs in nature.

4.2 Methods

We model a section of mid-ocean ridge offset by a single transform fault using the finite-difference code LaMEM (Kaus et al., 2016). Our goal in this model is to discern what conditions allow for the development of an orthogonal ridge-TF-ridge geometry in a visco-elastic-plastic rheology with no preferential weakness in shear.

4.2.1 Governing equations

LaMEM solves the equations for conservation of mass, momentum and energy on a fully-staggered grid [e.g., Gerya 2010],

$$\frac{\partial v_i}{\partial x_i} = 0 \tag{4.1}$$

$$\frac{\partial \sigma'_{ij}}{\partial x_j} - \frac{\partial P}{\partial x_i} + \rho g = 0 \tag{4.2}$$

$$\rho C_p \frac{DT}{Dt} = \frac{\partial}{\partial x_i}\left(k \frac{\partial T}{\partial x_i}\right) \tag{4.3}$$

where v indicates velocity, σ'_{ij} denotes deviatoric stress (indices i and j indicate the vertical or horizontal direction respectively; repeated indices indicate summation), and T is temperature. Pressure, density, heat capacity, and thermal conductivity are indicated by P, ρ, c_p, and k, respectively; g is gravitational acceleration. On the left-hand side of Equation 4.3, $\frac{DT}{Dt}$ is the material time-derivative of T.

Rheologically, we simulate deformation of a visco-elastic-plastic material and deviatoric stresses are related to strain rates in the constitutive equation

$$\dot{\epsilon}_{ij} = \dot{\epsilon}^{el}_{ij} + \dot{\epsilon}^{vs}_{ij} + \dot{\epsilon}^{pl}_{ij} = \frac{\overset{\diamond}{\tau}_{ij}}{2G} + \dot{\epsilon}^{vs}_{ij}\frac{\tau_{ij}}{\tau_{II}} + \dot{\epsilon}^{pl}_{ij}\frac{\tau_{ij}}{\tau_{II}}, \tag{4.4}$$

where the deviatoric strain rate tensor is

$$\dot{\epsilon}_{ij} = \frac{1}{2}\left(\frac{\partial v_i}{\partial x_j} + \frac{\partial v_j}{\partial x_i}\right) - \frac{1}{3}\frac{\partial v_k}{\partial x_k}\delta_{ij}, \tag{4.5}$$

and $\dot{\epsilon}_{ij}^{el}$, $\dot{\epsilon}_{ij}^{vs}$, $\dot{\epsilon}_{ij}^{pl}$ are the elastic, viscous, and plastic components, G is the elastic shear modulus, and the subscript $_{II}$ denotes the root of the second invariant of the respective tensor. The Jaumann objective stress rate is

$$\overset{\diamond}{\tau}_{ij} = \frac{\partial \tau_{ij}}{\partial t} + \tau_{ik}\omega_{kj} - \omega_{ik}\tau_{kj}, \tag{4.6}$$

and the spin tensor ω_{ij} is

$$\omega_{ij} = \frac{1}{2}\Big(\frac{\partial v_i}{x_j} - \frac{\partial v_j}{x_i}\Big), \tag{4.7}$$

where indices i, k, and j indicate the x, y, and z directions and repeated indices indicate summation; ω_{ik} and ω_{kj} in Eq. 4.6 follow the same convention. The magnitude of the viscous strain rate is defined using a fixed viscosity

$$\dot{\epsilon}_{ij}^{vs} = \eta\tau_{II} \tag{4.8}$$

where η is the material viscosity. The plastic strain rate $\dot{\epsilon}_{ij}^{pl}$ is determined using a Drucker-Prager yield criterion

$$\tau_{II} \leq \tau_Y = P\sin\phi + C\cos\phi \tag{4.9}$$

where ϕ is the angle of internal friction and C is cohesion. Plastic deformation is tracked through time and yielding is simulated by lowering the viscosity in a material when the yield stress is met (Equation 4.9). With increasing plastic strain accumulation, material cohesion C is reduced by

$$C = C_0 + C_{init}(1 - \frac{\epsilon_{APS} - \epsilon_{crit}}{\epsilon_{max} - \epsilon_{crit}}), \tag{4.10}$$

where ϵ_{APS} is accumulated plastic strain, ϵ_{crit} is the critical strain defining the onset of plastic failure, ϵ_{max} is the maximum plastic strain (corresponding to maximum weakening and cohesion reduction), C_{init} is initial material cohesion, and C_0 is the minimum (fully weakened) material cohesion.

A prescribed healing rate reduces plastic strain over time in the models according to

$$\epsilon_{APS} = \epsilon_{APS}\left(1 - \frac{dt}{t_{heal}}\right) \tag{4.11}$$

where dt is the model time step, and t_{heal} is the healing rate.

The above equations are discretized on a fully-staggered finite difference grid (Gerya, 2009). Material properties are advected using a marker-in-cell method with a conservative velocity interpolation scheme. Elasticity is implemented using a Maxwell relation where the effective strain rate

$$\dot{\epsilon}^*_{ij} = \dot{\epsilon}_{ij} + \frac{\tau^*_{ij}}{2G\Delta t}, \tag{4.12}$$

accounts for elastic stresses stored and advected with the material from the previous time step (indicated by n). The elastic history stress from the previous time step τ^n_{ij} is advected to account for rigid body rotation via

$$\tau^*_{ij} = \tau^n_{ij} + \Delta t(\omega_{ik}\tau^n_{kj} - \tau^n_{ik}\omega_{kj}). \tag{4.13}$$

The effective viscosity and updated stresses are calculated using the effective strain rate

$$\tau_{ij} = 2\eta^*\dot{\epsilon}^*_{ij}, \tag{4.14}$$

where effective viscosity is

$$\eta_{eff} = min\left[\left(\frac{1}{G\Delta t} + \frac{1}{\eta_{visc}}\right)^{-1}, \frac{\tau_Y}{2\dot{\epsilon}^*_{II}}\right]. \tag{4.15}$$

The system of equations is solved with a preconditioned Jacobian-Free Newton-Krylov (JFNK) method using the PETSc SNES solver framework (Katz et al., 2007; Balay et al., 2011; Kaus et al., 2016),

$$\mathbf{A}_{-1}\mathbf{J}(\bar{\mathbf{x}}_k)\partial\bar{\mathbf{x}}_k = -\mathbf{A}_{-1}\bar{\mathbf{r}}\bar{\mathbf{x}}_k \tag{4.16}$$

$$\bar{\mathbf{x}}_{k+1} = \bar{\mathbf{x}}_k + \alpha\partial\bar{\mathbf{x}}_k \tag{4.17}$$

where $\mathbf{A}$ is a preconditioning matrix, $\bar{\mathbf{x}}$ is the solution vector, $\alpha\partial\bar{\mathbf{x}}_k$ is the correction for each JFNK iteration, $\bar{\mathbf{r}}$ is the residual, α is a tuning factor for line-search length, and k is the iteration number. The Jacobian $\mathbf{J} = \partial\bar{\mathbf{r}}/\partial\bar{\mathbf{x}}$ is defined analytically to improve computational speed.

The preconditioning matrix $\mathbf{A}$ is obtained by discretizing equations 4.1–4.3,

$$\mathbf{A} = \begin{pmatrix} \mathbf{K} & \mathbf{G} & 0 \\ \mathbf{D} & \mathbf{C} & 0 \\ 0 & 0 & \mathbf{E} \end{pmatrix} \tag{4.18}$$

where $\mathbf{K}$, $\mathbf{C}$, and $\mathbf{E}$ are the velocity, pressure, and temperature block stiffness matrices. $\mathbf{G}$ is the pressure gradient matrix and $\mathbf{D}$ is the velocity divergence matrix. LaMEM employs a multigrid method to reduce computational time [Kaus et al., 2016].

Accretion of new lithosphere material at the ridges is approximated by converting asthenosphere material to lithosphere material when marker temperature T falls below 700°C.

4.2.2 Model setup

The model domain (Figure 4.1) is 156 x 156 x 64 kilometers, discretized over 128 x 128 x 64 nodes. Initial conditions prescribe a half-space cooling model with an age profile designed to focus deformation into an initial ridge-TF-ridge geometry. Three materials exist in the domain : (1) a five km-thick low-viscosity (1×10^{17} Pa s), low-density sticky air layer (Crameri et al., 2012) (2) a eight km-thick high-viscosity (1×10^{24} Pa s) elastic-plastic lithosphere layer, and (3) a low viscosity (1×10^{18} Pa s) asthenosphere that fills the remaining 51 km of the domain. The depth to the base of the lithosphere is set to the depth of the 800°C isotherm with the initial thermal profile calculated as a half-space cooling model (Turcotte and Schubert, 2002) with a uniform age of 0.5 Myr. In a 20 km-wide region offset by an 80 km-wide TF at the center of the domain, the age of the cooling model decreases to 0.1 Myr, creating an offset notch (∼3 km thick at the thinnest region) designed to localize deformation into an orthogonal ridge-TF-ridge geometry (Figure 4.1).

Model boundary conditions simulate seafloor spreading. Spreading velocity is imposed on the x faces and a free slip condition is imposed on the y faces. Outflow of lithosphere and asthenosphere material is balanced by a corresponding inflow condition on the bottom of the domain,

$$v_z = \frac{59}{78} v_x. \tag{4.19}$$

On the top of the domain, sticky air is allowed to flow in freely (open top) to replace material departing from the sides of the domain.

Parameters varied in the numerical model include spreading rate, thermal conductivity of the lithosphere (asthenosphere has a fixed conductivity), the rate of cohesion weakening with plastic strain, the onset of cohesion weakening, and the healing rate for accumulated plastic strain. Fixed model parameters are listed in Table 4.1. Models are run for a

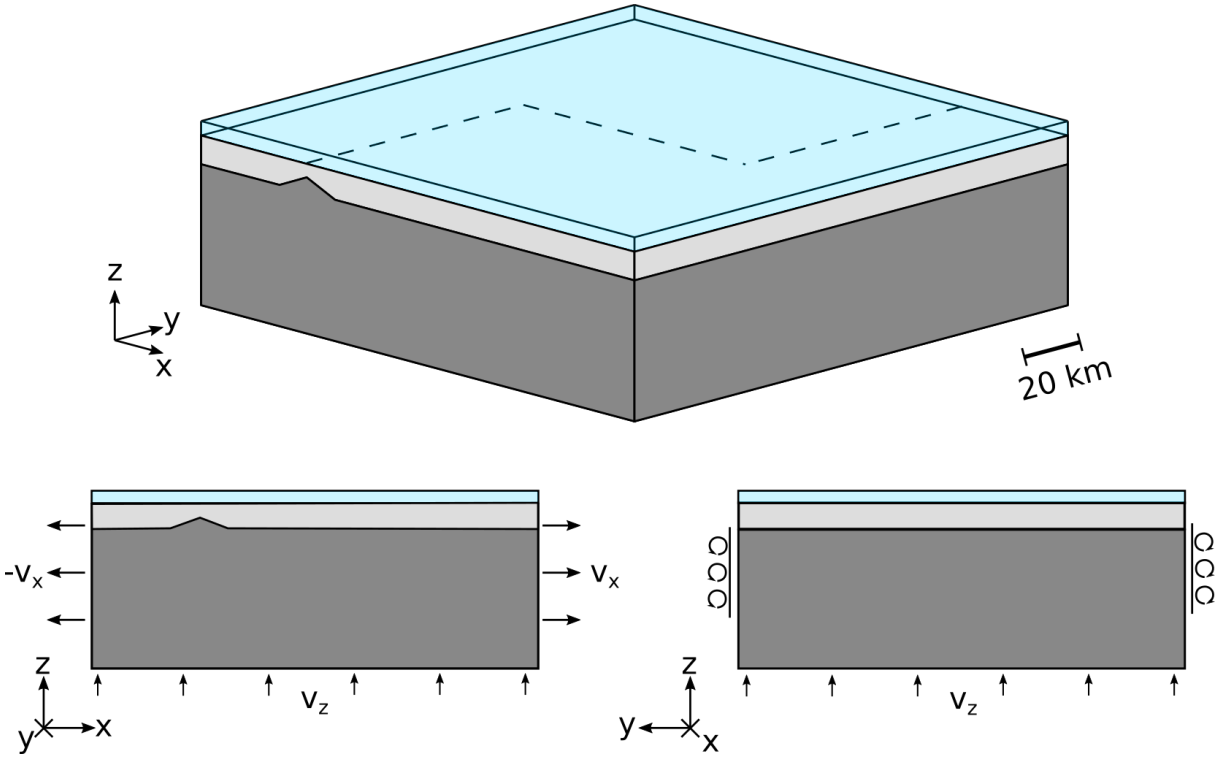

Figure 4.1: Numerical model setup. A low-viscosity, low-density sticky air layer (blue) overlies a high-viscosity lithosphere layer (light gray). The lower part of the domain is comprised of a low-viscosity asthenosphere (dark gray). A notch in the lithosphere follows the trace of the dotted line, designed to initiate an orthogonal ridge-TF-ridge geometry. Spreading is imposed on the x faces, while the y faces are free-slip. An inflow condition on the bottom of the domain compensates the lithosphere and asthenosphere material leaving the sides of the domain, while an open inflow condition along the top boundary compensates the material leaving in the sticky air layer.

Table 4.1: Model parameters and constants

Parameter	Description	Value (units)
η_0	Reference viscosity	1×10^{20} Pa s
T_0	Reference temperature	1300°C
L_0	Reference length	1 km
σ_0	Reference stress	1×10^9 Pa
dt	Time step	0.01 Myr
η_{min}	Minimum viscosity	1×10^{17} Pa s
η_{max}	Maximum viscosity	1×10^{26} Pa s
ρ_{sticky}	Sticky air density	0.001 kg m^{-3}
η_{sticky}	Sticky air viscosity	1×10^{17} Pa s
ρ_{lith}	Lithosphere density	3100 kg m^{-3}
η_{lith}	Lithosphere viscosity	1×10^{24} Pa s
ρ_{asth}	Asthenosphere density	3200 kg m^{-3}
η_{asth}	Asthenosphere viscosity	1×10^{18} Pa s
k	Thermal conductivity	1 W m^{-1} K^{-1}
G	Shear modulus	1×10^{10} Pa
ν	Poisson's ratio	0.25
C_0	Initial cohesion	3×10^7 Pa
C_{min}	Failed cohesion	2×10^6 Pa
ϕ	Friction angle	30°
α	Thermal expansivity	3×10^{-5} K^{-1}
C_p	Heat capacity	1000 kg m^2 K^{-1} s^{-2}

minimum of 4 Myr or as long as they continue to converge numerically (convergence criterion of $<1 \times 10^{-5}$ norm of the linear Newton solves); some models do not achieve 4 Myr (Table 4.2).

4.3 Results

Each model produces a qualitatively similar result (Figure 4.2, 4.3, and 4.4). The orthogonal weakness initiates as a strike slip transform fault. Ridge tips adjacent to the TF migrate towards the domain edges and strike slip motion along the TF transitions to oblique spreading within the first 0.5 Myr (Figure 4.2). Each end of the TF curves towards the retreating ridges, eventually producing a sinusoidal spreading center (Figure

4.4). For all models, pure strike slip motion is not maintained anywhere along the initial TF offset.

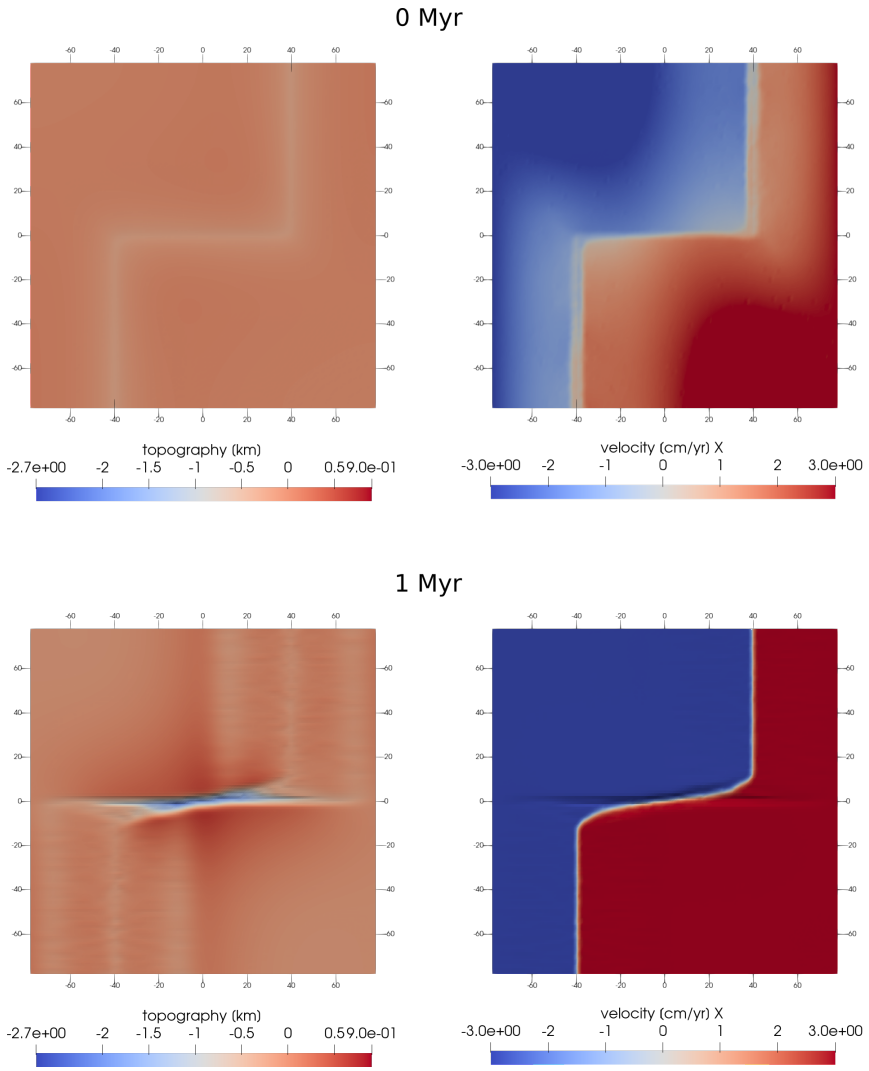

Figure 4.2: Representative lithosphere surface topography (left) and x velocity (right) at model initialization (top) and 1 Myr (bottom) for simulation 2 (Table 4.2). The orthogonal TF begins migrating towards a sinusoidal oblique spreading center shortly after spreading initiates.

To quantify the orthogonal-to-oblique spreading transition described above, we compare the magnitude of x velocities along two profiles taken across the model domain parallel to the y axis. One velocity profile is taken through the center of the domain, along the y axis (Figure 4.5, a-a'). The other profile is taken along the y axis two kilome-

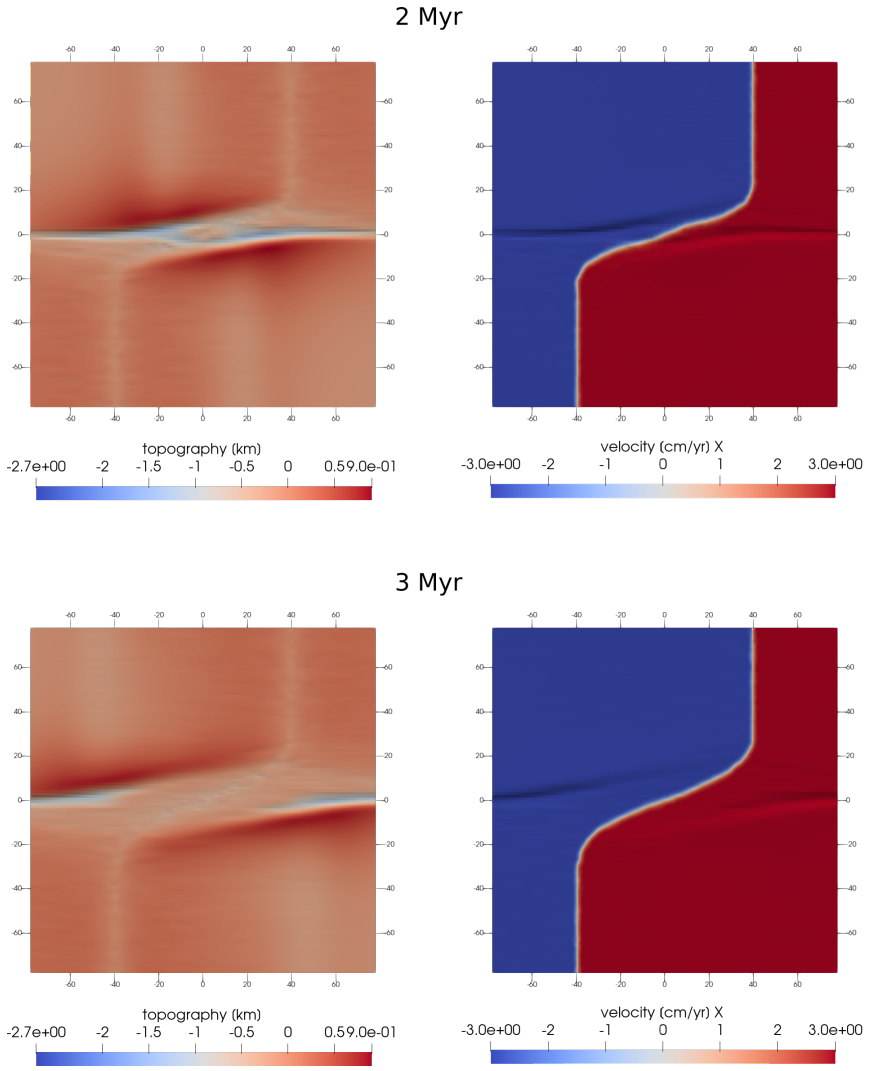

Figure 4.3: Representative lithosphere surface topography (left) and x velocity (right) at 2 Myr (top) and 3 Myr (bottom) for simulation 2 (Table 4.2). The orthogonal TF continues developing into a sinusoidal oblique spreading center and the original strike slip trace (deeper region in 2 Myr topography) converts to a spreading center.

ters from the spreading center, towards the center of the model domain (Figure 4.5, b-b'). For an idealized R -TF-R system where orthogonality between the TF and the ridge sections is maintained, x velocities along each profile are always identical. Here, the R-TF-R system reshapes into an oblique spreading center causing the velocity profile along the b-b' section to differ from a-a'. We normalize the measured velocities to spreading rate and measure the integrated difference in velocities along profile pairs (Figure 4.6). We report

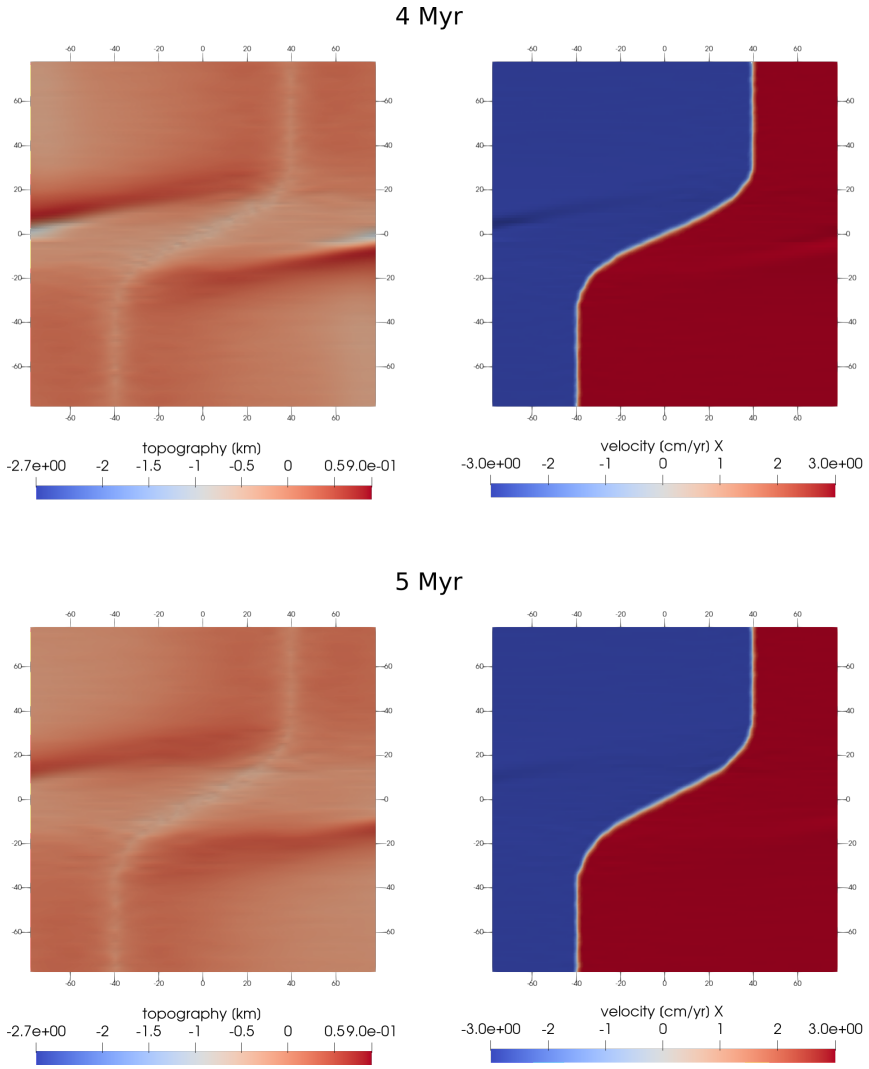

Figure 4.4: Representative lithosphere surface topography (left) and x velocity (right) at 4 Myr (top) and 5 Myr (bottom) for simulation 2 (Table 4.2). The sinusoidal portion of the oblique spreading center lengthens, with the center portion at 45° oblique to spreading direction.

this distance as a measure of divergence from orthogonality and hereinafter refer to this measurement as the integrated orthogonality. In the extreme case where a single ridge crosses diagonally through the domain, the integrated orthogonality difference in velocity profiles has a maximum of 128 km, representing the least orthogonal case. Likewise, a perfectly orthogonal TF offsetting two ridges will have zero integrated orthogonality. We determine the integrated orthogonality for each time step after 0.25 Myr (Figure 4.7) and

fit a least squares line to each model. The slope of this line (Table 4.2) quantifies the rate at which the ridge system departs from the orthogonal starting condition (orthogonality departure rate).

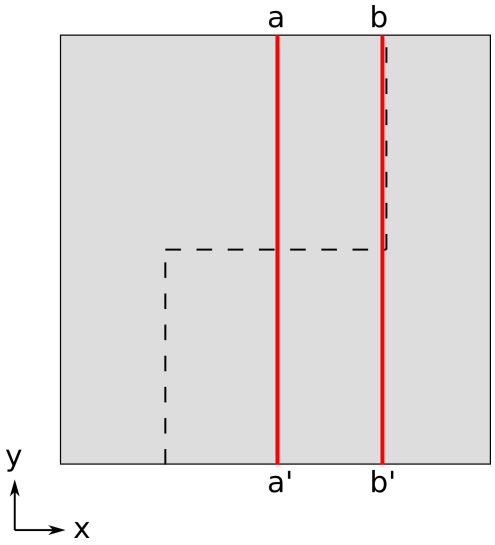

Figure 4.5: To quantify the evolution of the orthogonal R-TF-R system into an oblique spreading center, we compare two velocity profiles taken across the model domain, a-a' and b-b'.

Models results indicate several parameters affect orthogonality departure rate. Lower healing rates (models 9 and 11, models 2 and 13, Figure 4.7) yield higher orthogonality departure rates. Earlier onset of plastic failure (models 10 and 14), also yields higher orthogonality departure rates. Higher thermal conductivity in the model lithosphere reduces orthogonality departure rates (models 5 and 17), while an increase in the amount of plastic strain required to fully weaken the lithosphere (models 9 and 17 as well as models 5 and 6) does not significantly alter the orthogonality departure rate.

4.4 Discussion

Several parameters in our models control rate of orthogonality departure; each parameter relates to specific characteristics of the lithosphere. First, the association of higher thermal conductivity with lower orthogonality departure rate is likely a reflection of the

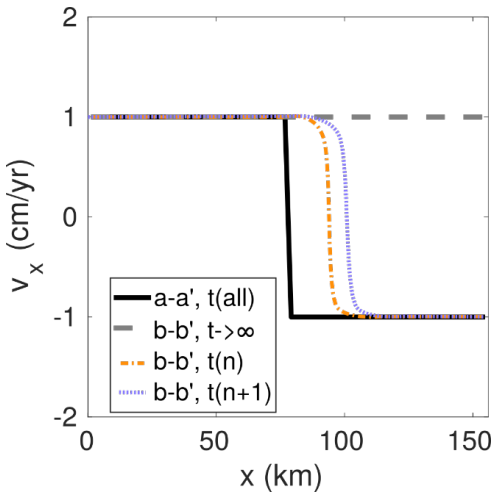

Figure 4.6: The a-a' velocity profile (here plate velocity is 1cm/yr in each direction) is constant for all model times. The initial b-b' profile matches the a-a' profile. The velocity profile b-b' reflects increasing obliquity as model time accrues, gradually rounding out the stepped corners and shifting right (from orange to blue). A theoretical maximum obliquity exists in the condition where the TF corner migrates to the edge of the model domain (grey dashed line).

integrated strength of the lithosphere. Higher thermal conductivity yields a thicker, and thus stronger, elastic layer. Reshaping the initially orthogonal TF requires damage migration away from the initial notched structure (Figure 4.1). Higher thermal conductivity produces thicker lithosphere outside of the notched region, which resists ridge migration.

The onset of plastic failure and critical plastic strain parameters have little effect on orthogonal divergence. Higher values for the onset of plastic failure delay weakening in the elastic material, but only slightly reduce the overall orthogonality departure values at the same model time (Figure 4.7). The orthogonality departure rate in models 10 and 14 are almost identical. Delaying the onset of plastic failure delays system migration, but there is little difference in model behavior after the delay. Critical plastic strain values (Figure 4.7 E and F) also do not affect orthogonality departure rates. Paired models with identical parameters and different critical plastic strains (0.2 and 1.0, models 9 and 17; 1.0 and 0.03, models 5 and 6) share orthogonality departure rates and are equally orthogonal at the same time.

Table 4.2: Model parameters and orthogonality departure rates

Model	Spreading Rate (cm/yr)	Healing rate (1/s)	k (W/m/K)	APS onset	Critical APS	Orthogonality departure rate (km/Myr)	Model end time (Myr)
1	3	1.00×10^{-12}	4	0	1	52.07	1.12
2	3	1.00×10^{-12}	4	0.5	0.2	19.91	6.82
3	2	1.00×10^{-12}	4	0	0.2	25.96	1.30
4	2	1.00×10^{-12}	4	0.5	1	16.01	4.45
5	2	1.00×10^{-12}	4	0	1	17.64	4.15
6	2	1.00×10^{-12}	4	0	0.03	13.74	5.70
7	2	1.00×10^{-14}	4	0	0.2	7.37	1.30
8	2	1.00×10^{-14}	4	0.5	1	19.86	1.30
9	2	1.00×10^{-12}	2	0	0.2	23.88	3.75
10	3	1.00×10^{-14}	2	0	1	19.05	4.17
11	2	1.00×10^{-14}	2	0	0.2	13.41	4.10
12	3	1.00×10^{-14}	4	0	0.2	18.26	4.62
13	3	1.00×10^{-14}	4	0.5	0.2	16.09	4.52
14	3	1.00×10^{-14}	2	0.5	1	16.09	4.52
15	3	1.00×10^{-14}	2	0	0.2	33.15	1.07
16	3	1.00×10^{-12}	2	0	0.2	51.66	1.07
17	2	1.00×10^{-12}	2	0	1	24.63	3.82

Healing rates exert a strong control on oblique TF divergence. In models 9 (healing rate 1×10^{-12} s^{-1}) and 11 (healing rate 1×10^{-14} s^{-1}), larger healing rate corresponds to faster divergence from the orthogonal condition. In models 2 and 13, higher healing rate corresponds to faster orthogonality departure, though model 13 achieves higher orthogonality at model times <2 Myr. With larger healing rates, damaged weak zones strengthen slower. Slower strengthening broadens the zone of plastic failure (e.g., Lavier et al., 2000) making it easier for the length of the TF undergoing strike slip motion to shorten.

Modeled transform faults exist only in material with a preferred weakening orientation or in models where the TF is inherently weaker than adjacent ridges (Freund and Merzer, 1976). Indeed, in our elastic materials, orthogonal transform faults are not maintained in any of the tested conditions and parameter combinations.

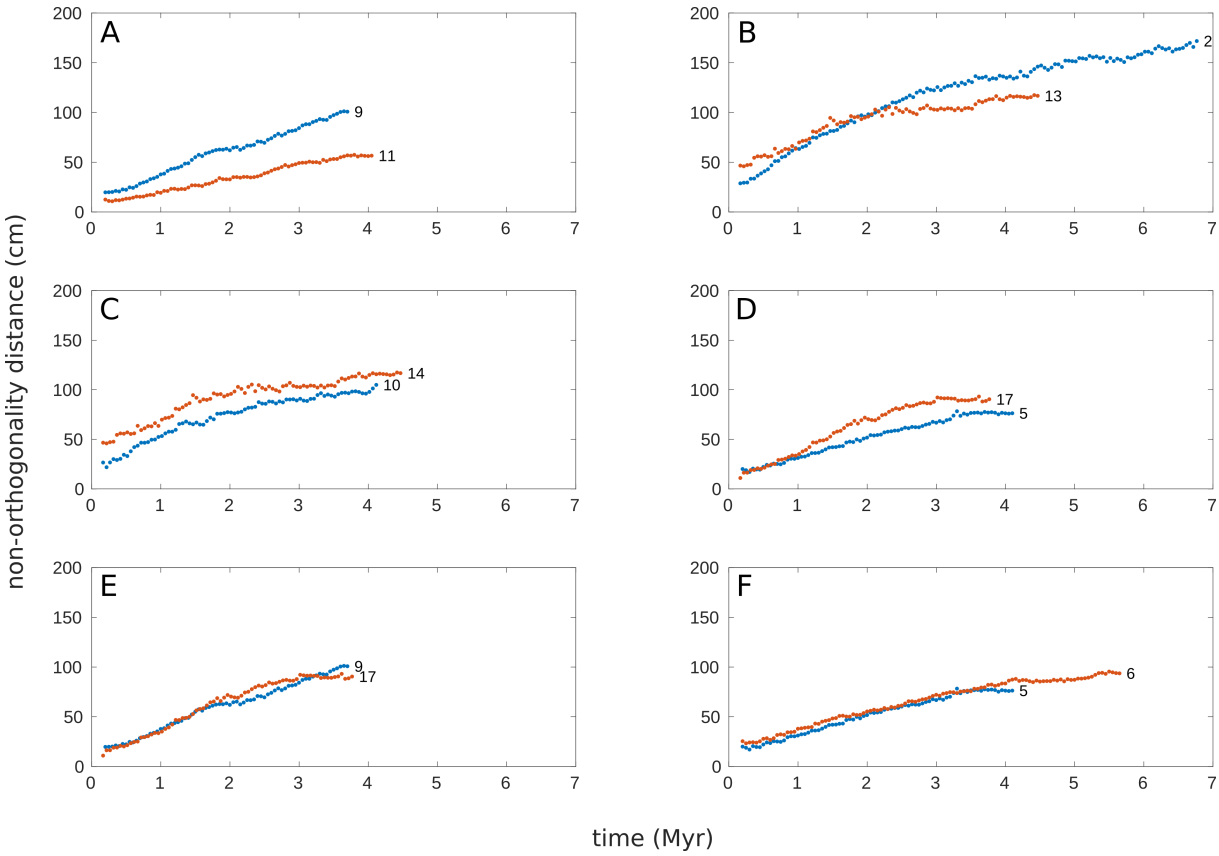

Figure 4.7: Numerical model comparisons. All models increase non-orthogonality with time . (A) Model 9 has a higher rate than Model 11. (B) Model 2 has a higher healing rate than Model 13. (C) Model 10 has an earlier onset of plastic failure, lower overall non-orthogonality, and greater orthogonality divergence rate than Model 14. (D) Model 5 has higher thermal conductivity than Model 17. (E) Models 9 has a smaller critical APS, but almost identical orthogonality divergence as Model 17. (F) Model 6 has a much smaller critical APS than Model 5, but almost the same orthogonality divergence rate.

4.4.1 Comparisons with previous models

A critical evaluation of model success in reproducing oceanic TFs involves evaluating model stability over long periods of time, as TF offsets on Earth exist for millions of years. While our early (<100 kyr) results are qualitatively similar to results from Choi et al. (2008), our simulations fail to produce stable, long-lived orthogonal TFs. To date, only one numerical model has produced long-term (millions of years) models of TF formation and stable evolution (Gerya, 2010b; Püthe and Gerya, 2014).

Püthe and Gerya (2014) achieve ridge-orthogonal TFs from a similar model setup in an visco-plastic rheology across a similar range of parameters to those presented here. Interestingly, we are unable to reproduce the same orthogonal ridge-TF-ridge pattern. Some key differences between the two models may be responsible. First, Püthe and Gerya (2014) simulate a mechanically weak magma chamber within their models, in locations where partial melting is expected (e.g., Katz et al., 2003). The methodology inherently produces a small region of low density, low viscosity material within the lithosphere that may serve to anchor ridge locations. It appears that the migration of this low density, low viscosity chamber from both ridge tips in some of the Püthe and Gerya (2014) models leads to results qualitatively similar to ours, yielding a sinusoidal spreading center. Second, Püthe and Gerya (2014) do not include elasticity in their simulated lithosphere. The purpose of this study was to simulate the formation of an orthogonal TF system using a visco-elastic-plastic rheology with no preferential weakness orientation, and we are unable to reproduce the orthogonal systems generated by Püthe and Gerya (2014), which suggests that our model is missing a fundamental component of the physics involved, or that forming orthogonal TFs in elastic media is fundamentally different from forming TFs in a visco-plastic media.

In an earlier version of the same visco-plastic model (Gerya, 2010b), orthogonal TFs appeared spontaneously along an initially straight spreading center due to dynamic instabilities. These results suggested that TFs are inherently spontaneous results of asymmetric accretion on spreading centers. However, our results suggest something quite different – an initial TF preferentially transitions to a spreading center, and the spreading-only configuration is the long-term stable condition. Again, this may be a result of including elasticity in lithosphere rheology. Hieronymus (2004) suggests that orthogonal TF formation is dependent upon a difference in shear and tensile strength in the elastic lithosphere, a physical characteristic that we did not employ in our models.

Accounting for preferential weakness in shear in future numerical models may be accomplished in at least two ways in the numerical code presented here. First, implementing shear modulus weakening (instead of cohesion weakening) may add the preferential shearing weakness described by Hieronymus (2004) as essential to TF formation. Alternatively, adding an orthogonal thermal stress (e.g., Choi et al., 2008) formulation may serve the same purpose, effectively reducing the normal stress across the TF and thus weakening it relative to the ridge segments. Implementing either of these options in LaMEM requires some careful consideration to impacts on other features of the code. For example, the thermal stress condition will depend on the assumed distance between the modeled TF and the next location relieving thermal stresses (i.e., the nearest TF outside the model domain). Exploring these implementations and comparing results to the existing suite of results presented here is a promising route for future investigations.

4.5 Conclusions

We have presented results of a series of numerical models simulating the evolution of an initially orthogonal ridge-TF-ridge system in a visco-elastic-plastic lithosphere. Results indicate that an orthogonal ridge-TF-ridge system is not stable over time in models that do not have a preferred weakness orientation (i.e., are weaker in shear than in tension). All model parameters yield TFs that evolve towards an oblique, sinusoidal ridge structure with the rate of migration controlled primarily by the thermal conductivity of the elastic layer and the healing time implemented in the plasticity formulation. The onset of plastic failure and the rate of cohesion loss do not affect how fast the system departs from orthogonality. Our results support conclusions that TF formation is dependent on the oceanic lithosphere being weaker in shear than in tension (e.g., Hieronymus, 2004; Choi et al., 2008).

Chapter 5: Plume Volume Fluxes

5.1 Introduction

Many hotspot volcanoes form by partial melting of upwelling mantle plumes (e.g., Richards et al., 1989; Condie, 2001). Though originally envisioned as stationary conduits of buoyant, upwelling material (Wilson, 1963; Morgan, 1971; Sleep, 1990), detailed observations (Vogt, 1971; White and Lovell, 1997; White, 1997; O'Connor et al., 2000; O'Connor et al., 2002), advances in our understanding of mantle rheologic influences on plume structure (Keken et al., 1992; Keken and Gable, 1995), and systematic numerical studies (Ito, 2001) suggest that mantle plumes may have temporally variable mass flux and melt production.

Early observations along the Reykjanes Ridge south of Iceland revealed a series of V-shaped ridges propagating away from the hotspot (Vogt, 1971). Subsequent investigations attribute the V-shaped ridges to thermal fluctuations in the Iceland plume (White, 1997), a conclusion supported by observations of corresponding pulses in sediment deposition rates (White and Lovell, 1997) and crustal thickness variations in the Norwegian Sea, as measured by seismic reflection and gravity anomaly observations (Parkin et al., 2007). Off the coast of Scotland, O'Connor et al. (2000) interpret seamount emplacement over 5-10 million-year periods as possible indicators of periodic fluctuations in mass flux within the Iceland plume. Jones et al. (2002) produced a model suggesting that time-dependent pulsations in the Iceland plume stalk below 100 km depth are responsible for generating V-shaped ridges in gravity-derived crustal thickness observations at Iceland. In contrast, Hey et al. (2010) observe asymmetric accretion along the V-shaped ridges at Iceland and suggest that rifting processes, not pulsations in the Iceland plume, are responsible for temporal variations in crustal thickness. Escartín et al., 2001b observed Iceland-like V-

shaped ridges and variations of crustal thickness near the Azores hotspot, suggesting they may be a result of periodic temperature and/or flux variations in the Azores plume.

Studies that attempt to quantify hotspot melt production and plume flux over time at Hawaii (White, 1993a; Van Ark and Lin, 2004; Vidal and Bonneville, 2004), Iceland (Mjelde and Faleide, 2009), and the NinetyEast Ridge (Sreejith and Krishna, 2015) find further evidence of plume variability. For example, Van Ark and Lin (2004) use bathymetry and estimates of crustal thickness from satellite-derived gravity to suggest that igneous volume flux along the Hawaiian-Emperor seamount chain varies between 0 and 8 m^3/s over time scales of 6–30 Myr, consistent with earlier Airy isostatic estimates of 0.95–5.08 m^3/s (White, 1993a). Unlike White (1993a) and Van Ark and Lin (2004), Vidal and Bonneville (2004) quantified melt production at the Hawaiian hotspot using a filtering method to isolate the volcanic edifice while accounting for the isostatic and/or flexural root of the edifice and approximating the swell amplitude of the hotspot. Their calculations predict an increase in Hawaiian hotspot swell amplitude since 30 Ma and 5 Myr oscillations in magma production. Using a residual separation filtering method, Wessel (2016) estimated melt production since 40 Ma along the Hawaiian hotspot track and concluded that Hawaiian magma production has steadily increased since 20 Ma, with periodic variations in melt flux over short time scales of 1–2 Myr.

In other works, researchers estimate the volumetric flux of Iceland and along the NinetyEast Ridge. Using a compilation of magmatic thickness measurements from a variety of observations, Mjelde and Faleide (2009) estimate melt production from the Iceland hotspot in the North Atlantic, indicating a maximum rate of 55.5 m^3/s and a minimum of 4 m^3/s (though the maximum is associated with early-stage rifting). Sreejith and Krishna (2015) calculate magma production rates from satellite gravity-derived crustal thickness estimates along the NinetyEast Ridge and predict production rates between 2 and 15 m^3/s, with fluctuations over periods of 5–16 Myr.

Hotspots have temporal variations in their melt production, but the underlying causes of melt production variations are unclear. The above studies attribute temporal variability in melt production to a range of processes including along-track changes in lithosphere properties (e.g., age and thickness), responses to plate motion changes during plate reorganizations, flux variations intrinsic to the plume conduit or its source, or a combination of these processes. Discerning between these possible causes for hotspot melt flux variations requires a systematic, comparative study; we are unaware of a study using a consistent methodology at multiple hotspots. Mjelde and Faleide (2009) compare their Iceland melt flux power spectrum with flux power spectrum from Hawaii (Van Ark and Lin, 2004) and suggest that co-pulsations within the two spectra are results of a periodic release of heat from the Earth's core. However, the Mjelde and Faleide (2009) methodology differs from Van Ark and Lin (2004). Mjelde and Faleide (2009) give estimates that are primarily derived from seismic mapping efforts across large sections of Greenland, in some cases estimating the extents of unexposed flows. Van Ark and Lin (2004) determine the volcanic edifice volume from residual separation filtering and crustal thicknesses along the Hawaiian track using gravity anomaly data. Given the methodological difference, the comparability of these results is unclear.

Here, we calculate and analyze volumetric melt production over time at twelve hotspots using the same methodology for each, resulting in a comparative data set. Using age data and global satellite observations, we filter bathymetry and model gravity anomaly data to constrain melt production over time. This study seeks to comparatively quantify hotspot melt production over time at twelve hotspots and investigate temporal relationships in melt production between different hotspots.

5.2 Methods

5.2.1 Along track hotspot melt production

We estimate the melt production along a hotspot chain by isolating three volumetric contributions: the volcano edifice, volcanic infill of plate flexure (e.g., Watts, 1978) and magmatic underplating within or beneath the oceanic crust (e.g., Leahy et al., 2010) (Figure 5.1). We define the edifice as any volcanic constructive feature that rises above the long-wavelength shape of the seafloor. The infill volume includes material contained within the flexural "moat" surrounding the edifice and the volume of volcanic material below the edifice, but above the surface of the flexed crust. The underplating volume refers to any anomalous, low-density material within or below the oceanic crust. The method does not differentiate the source of melts, each volume is assumed to result from emplacement of volcanic material that formed during partial melting within a rising plume conduit.

To isolate volcanic edifices from the regional bathymetry (e.g., fracture zones, the hotspot swell, etc.), we follow the Optimized Residual Separation (ORS) method of Wessel (2016). Starting with a regional grid of bathymetry and topography from the Global Multi-Resolution Topography (GMRT) synthesis (Ryan et al., 2009), we first mask any continental features. Then, a series of median and Gaussian filter pairs with increasing width are employed to separate out regional bathymetry from the localized edifice. As filter width increases, more and larger small-wavelength features (residual seamounts and volcanic ridges) will pass through the filter, until the filter wavelength exceeds the size of these features and begins passing long-wavelength features (regional), such as the cooling and thermal subsidence curve of the lithosphere (wavelength 1000s of kms). Features such as seamounts and volcanic ridges have a high volume to surface area ratio, due to

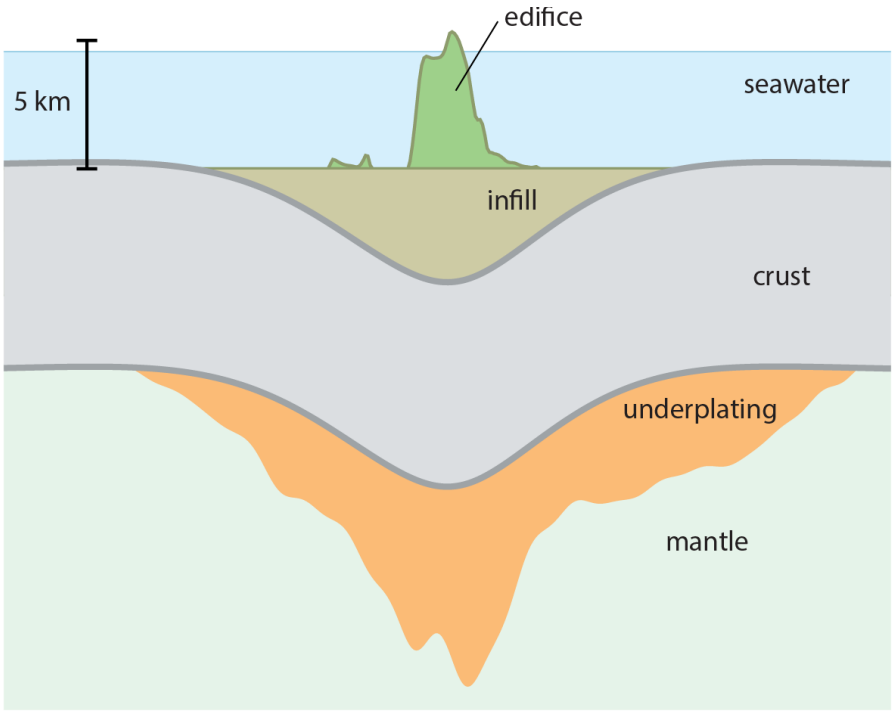

Figure 5.1: Generalized hotspot volumes (vertical axis not to scale). Edifice volume (green) includes positive relief from the seafloor. Infill volume (brown) is the volume contained within the flexural depression surrounding the edifice. Underplating volume (orange) is any gravity-derived mass deficit within or below the crust.

their shape, while long-wavelength features have smaller volume to surface area ratios. Wessel (1998) showed that a mathematically optimal and reproducible separation exists at the wavelength corresponding to a maximum in the residual grid volume to surface area ratio. Thus, the Optimized Residual Separation (ORS) method separates the volcanic edifice from regional features in a unique and reproducible way. We filter the complete topography grid (with previously-masked continental components returned, so that there are no major discontinuities in the grid during later steps) using the ORS-determined optimal filter width. To eliminate contributions from any remaining topographic features that are noted in the literature to be unrelated to a particular hotspot, we manually select the region around the edifices (Figure 5.2).

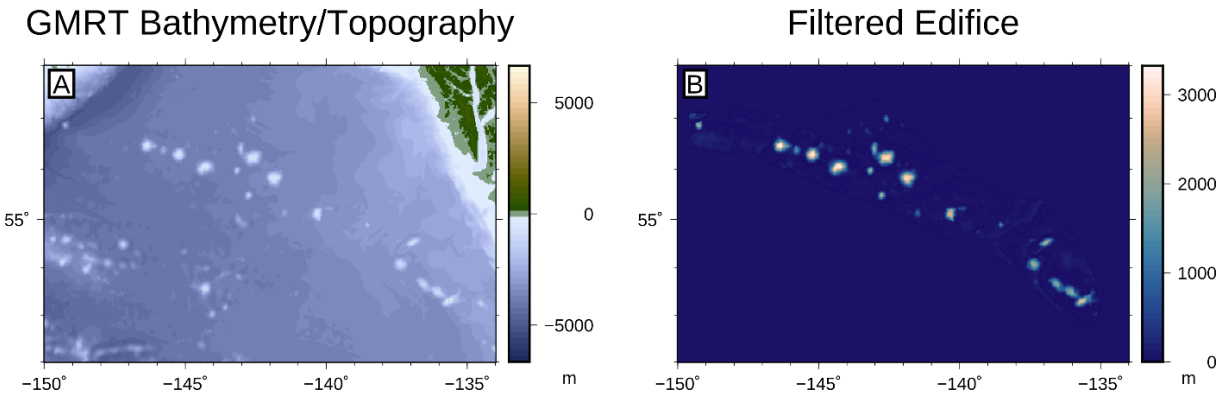

Figure 5.2: Bathymetry/topography filtering method at the Bowie hotspot track. From the GMRT synthesis, (A) bathymetry and topography for each hotspot is filtered and trimmed to isolate the (B) hotspot edifice from other features.

Hidden infill volumes are calculated using a spectral flexural calculation (Vidal and Bonneville, 2004; Wessel, 2001; Wessel, 2016). Following the Wessel (2016) formulation, the differential equation for plate flexure is solved in the wavenumber domain,

$$C(\mathbf{k}) = AU(\mathbf{k})\phi(\mathbf{k}), \tag{5.1}$$

where $\mathbf{k}$ is the wavenumber vector, U is the edifice load, and C is the deflection of the plate as a response to that load. A is the Airy isostatic ratio

$$A = \xi \frac{\rho_i - \rho_w}{\rho_m - \rho_e}, \tag{5.2}$$

where ρ_i, ρ_w, ρ_m, and ρ_e are the densities of the infill material, water, mantle, and the edifice, respectively. To reduce over- or under-estimating the flexural wavelength by choosing either the edifice or infill density for the spectral calculation (which requires uniform density), we adopt a compromise approach (Wessel, 2001) to handle density contrasts between the edifice and infill, scaling the Airy ratio A by ξ,

$$\xi = \sqrt{\frac{\rho_i - \rho_w}{\rho_m - \rho_e}}. \tag{5.3}$$

This scaling balances endmember cases using strictly the edifice or the infill density to determine the wavenumber in Equation 5.1, effectively introducing the ratio of the maximum amplitudes of deflection for point loads for each of the densities as a correction (Wessel, 2001). Thus, where our calculation would over-estimate flexural wavelength (in the case where ρ_i is the uniform density load) or over-estimate deflection amplitude (in the case where ρ_e is the uniform density load), we achieve a compromise that accounts for the majority of the infilling material having a density ρ_i and a small region of material directly underneath the volcanic edifice having a density ρ_i (Wessel, 2001).

The isostatic and flexural response function is

$$\phi(\mathbf{k}) = [1 + (|\mathbf{k}|/k_e)^4]^{-1}, \tag{5.4}$$

where k_e, the radial flexural wavenumber is

$$k_e = \left[\frac{\rho_m - \rho_e)g}{D}\right]^{\frac{1}{4}}, \tag{5.5}$$

and g is the acceleration due to gravity. D is the flexural rigidity of the lithosphere, defined as

$$D = \frac{ET_e^3}{12(1-\nu^2)}, \tag{5.6}$$

where E is Young's modulus and ν is Poisson's ratio.

Elastic thickness T_e of the lithosphere at loading time is determined in a half space cooling model as

$$T_e = \text{erf}^{-1}\left(T_{el}/T_m\right)2\sqrt{\kappa\Delta t}, \tag{5.7}$$

where T_{el} is the depth to the 400°C isotherm (assuming the base of the elastic lithosphere corresponds to an isotherm, e.g., Watts (1978)), T_m is the mantle potential temperature, κ is thermal diffusivity, and Δt is the loading age (age of the seafloor when the volcanic edifice was emplaced). Plate flexure is calculated assuming fixed densities for the edifice/oceanic crust and infill volume (2800 kg/m^3 and 2300 kg/m^3, respectively; Table 5.1).

Table 5.1: Melt volume parameters and constants

Parameter	Description	Value (units)
g	Gravitational acceleration	9.8 m s^{-2}
κ	Thermal diffusivity	1×10^{-6} m^{2}s^{-1}
E	Young's modulus	2×10^{10} Pa
ρ_m	Mantle density	3300 kg m^{-3}
ρ_e	Edifice density	2800 kg m^{-3}
ρ_w	Water density	1035 kg m^{-3}
ρ_i	Infill/Sediment density	2300 kg m^{-3}
ρ_u	Underplating density	3000 kg m^{-3}
ν	Poisson's ratio	0.25
T_{el}	Elastic isotherm	400°C
T_m	Mantle potential temperature	1300°C

Lithosphere loading age Δt is the age of the lithosphere at the time of volcanic emplacement, calculated with available data. Available age data from hotspot edifices are collated along-track. We then fit a linear polynomial to the age dates against longitude or latitude (depending on the primary orientation of the hotspot island/seamount chain); this polynomial is used as the "hotspot track" for each subsequent calculation. Every 20 km along track (or 10 in cases where the separation between age points is <20 km), we average seafloor age (Müller et al., 2008) within a 1-degree radius using a linear weighting scheme (i.e., age data closest to the selected along-track point is weighted one and age data at the maximum radial distance is weighted zero). At each point, loading age is the difference between the linearly-interpolated edifice ages and the average seafloor age.

After establishing the loading age, we calculate plate flexure due to the edifice load and effective elastic plate thickness associated with each loading age along the entire hotspot track. In other words, plate flexure is calculated over the hotspot track repeatedly with the same load, but with each calculation using an effective elastic thickness based upon the loading age every 20 km. At the same locations where we have determined loading age (e.g., every 20 km along track), the calculated flexure solutions are blended together using a weighted scheme such that in a surrounding 2° box (henceforth referred to as "regional box"), the flexure profile is calculated using the loading age at the chosen point and any area outside the box is weighted at 1/2. The resulting blends are combined such that the region immediately surrounding the point of interest will have a flexure profile determined by its loading age. Where one point's regional box overlaps its neighbor's, equal weighting is given to both flexure grids. Outside the specified point's box (generally beyond the flexural depression created by the edifice), flexure is determined as an equal weighting of grids for all loading ages. This method produces an along-track flexure grid that varies continuously with loading age and the elastic thickness of the lithosphere (Figure 5.3). Where the loading age is equal to the age of the lithosphere, we assume Airy isostatic compensation of the edifice (Vidal and Bonneville, 2004).

$$c_0 = \frac{\rho_i - \rho_w}{\rho_m - \rho_e} u(\mathbf{x}) = Au(\mathbf{x}). \tag{5.8}$$

Infill volume is then determined from the resultant flexure or isostatic grids. In the flexure case, we take the volume above the blended flexure profile to the zero datum (i.e., infill volume is assumed to completely fill the flexure depression). In the isostatic case, infill volume is the volume of the compensating root.

Finally, the underplating (or hidden) volume is determined by first creating a forward gravity model, removing this model from the observed free-air gravity anomaly, and inverting the residual for the thickness of a single layer or underplating material

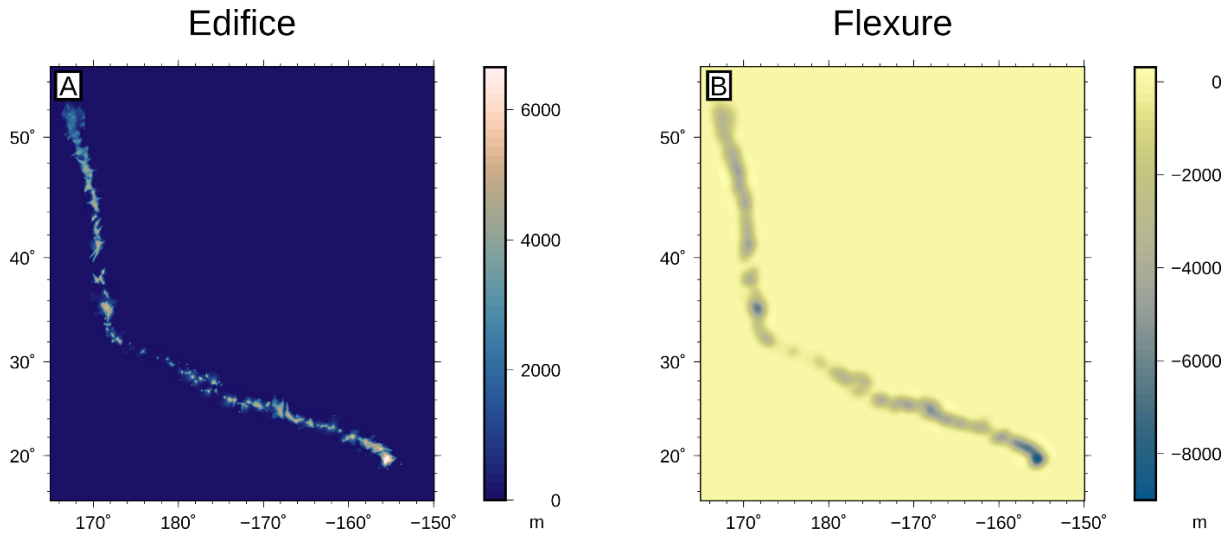

Figure 5.3: Flexure calculation method demonstrated at the Hawaiian hotspot track. The volcanic edifice (A) is treated as a load on an elastic plate with an elastic thickness determined by the plate's age and the loading age of volcanic material. The flexure profile (B) represents the deflection of the elastic plate due to the edifice load.

with assumed constant density contrast. Using the GMRT grid (Ryan et al., 2009), the global sediment grid (Whittaker et al., 2013), a global seafloor age grid (Müller et al., 2008), and our calculated flexure profile, we construct a forward gravity model using the Parker-Oldenburg iterative method for density interfaces (Parker, 1972; Oldenburg, 1974; Nagendra et al., 1996; Gómez-Ortiz and Agarwal, 2005). Our model includes density contrast contributions from the air/rock interface, sediment/water interface, water/rock interface, and crust/mantle interface. The air/rock interface contribution is determined by the subaerial topography using a density contrast of 2800 kg/m^3. The sediment/water interface contribution is determined from the GMRT grid and is defined using a density contrast of 1265 kg/m^3. While some regions have a negligible sediment contribution (i.e., regions far from continental input), some hotspots have significant sediment inputs overlaying the seafloor. In cases where the sediment grid predicts zero sediment thickness, we assume one meter of sediment overlies the seafloor (the spectral method requires a grid with no gaps or regions of zero thickness; the contribution from a one-meter layer will

be negligible). We then subtract the sediment thickness from the bathymetric grid and use a contrast of 500 kg/m^3 to determine the gravity anomaly contribution from the sediment/rock interface. This approach assumes that material filling the flexural depression (around, but not under the volcanic load) and not accounted for by the global sediment thickness map is comprised entirely of dense rock instead of a more realistic combination of edifice talus and sediments. We use our calculated flexure profile to constrain the shape of the crust/mantle interface (density contrast 500 kg/m^3) assuming a crustal thickness average of 7 km below average seafloor depth. We remove our forward model from the observed free-air gravity anomaly (Bonvalot et al., 2012) and assume that any remaining relative gravity anomaly contributions are contributions from low-density, hidden volumes in the mantle (i.e., underplating).

The thicknesses of underplating material are calculated by inverting the residual gravity anomaly values for the thickness of a sub-crustal layer. We use a modified version of the 3DINVER program (Gómez-Ortiz and Agarwal, 2005), which applies the Parker-Oldenburg iterative method to gravity anomaly observations (Figure 5.4). We use a density contrast of 300 kg/m^3 (mantle material 3300 kg/m^3 and underplating material 3000 kg/m^3) and assume the anomaly is at a depth in the Earth determined by the median depth of our calculated flexure profile. This compromise accounts for underplated material below the crust, but not directly beneath the deepest part of the flexure profile. The 3DINVER program requires a square observation region with a number of grid points equal to a power of two. To address this, we omni-directionally reflect our resulting gravity grid and re-sample a 2^{n+1} square grid from the new larger grid, where n is the highest power of 2 less than the smallest original grid dimension (i.e., if the gravity grid had a dimension of 100x200 nodes, we would resample the omni-reflected grid at 128x128 nodes). The reflection method yields spurious inversion results around the edges of the inversion grid, but with sufficient grid space (>500 km buffer added to each grid) around

the hotspot track, we can safely rely on the interior results. The resulting layer thickness calculation yields a non-unique measurement, as gravity residuals may be matched with a range of density anomalies. However, similar techniques are used to estimate crustal thickness along mid-oceanic ridges and are reasonably successful when compared with seismic data.

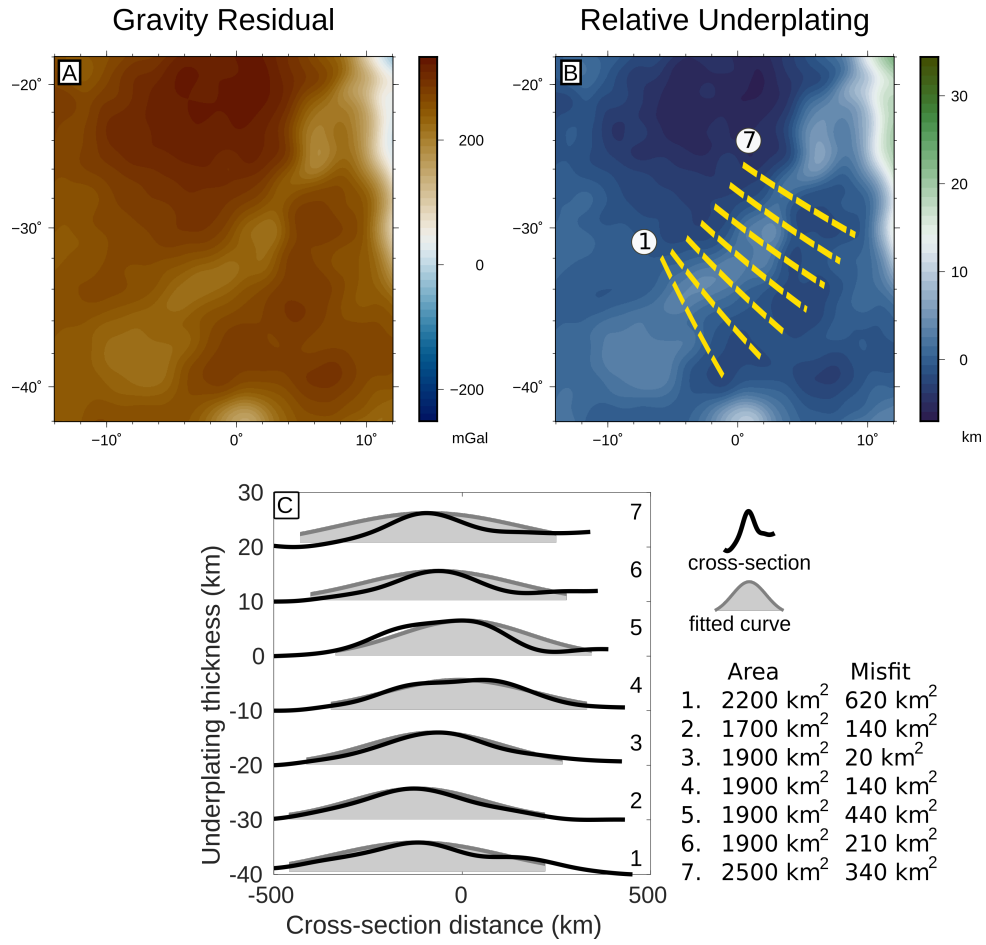

Figure 5.4: Underplating calculation. (A) Residual from gravity model after removing bathymetry, flexed crust, sediment, and correction for age of lithosphere. (B) Inversion result shows a relative thickness of low-density material at depth under the hotspot track. Yellow dashed lines (1-7) correspond to a selection of cross-profiles (C). Profiles 1-7 (black lines, offset by 10 km for clarity) and their corresponding Gaussian curve fits (gray shaded curves). Curve areas and misfit relative to inversion are reported for each profile. Gaussian misfits are greater when the curve is asymmetric (5) or the base level changes significantly across the profile (7).

The nature of this calculation yields an estimate of volume, but we are unable to determine the precise location of the low-density anomalies we constrain - they may be contained in the mantle or exist as dikes or sills within the lithosphere. Here we are treating the volume as a single, uniform density layer buried at depth. This is the volumetric component with the highest uncertainty. In some cases (see individualized results below), this calculation yields a result that is indistinguishable from noise, and we assume no significant underplating volume is present.

Volume contributions from the edifice, infill, and underplating material are calculated taking a hotspot-track perpendicular slice every 4 km from each of the three resultant grids: edifice, flexure, and underplating. Edifice and infill slices are subsequently used as-is from their respective grids, but slices from the gravity grid must be treated to remove edge effects and account for non-uniqueness in the resultant grid. The underplating grid generally has an arbitrary average value with a thickened region along the hotspot track. To remove spurious edge effects from each slice along the underplating grid and to measure only the relative thickness of underplating, we subtract the mean from each cross section and fit a Gaussian curve centered on the largest peak of each slice (Figure 5.4). We then take the area under the curve as the representative underplating profile. This method reduces edge effect contributions from non-hotspot features and mismatches in the background underplating signal contributed by bathymetric features that are not part of the underplating signal. Each along-track slice from each of the three grids is integrated numerically using the trapezoid method and multiplied by the slice separation distance to produce a volume measurement along the hotspot track (Figure 5.4). We do not report underplating volumes at hotspots with a total along-track average below 1000 km^3.

5.2.2 Power spectrum analysis of melt volumes

To analyze the temporal variability in our melt volumes, we use a Lomb-Scargle periodogram (Lomb, 1976; Scargle, 1982) to isolate statistically significant frequencies of plume melt volume variations. We use the Lomb-Scargle method as our along-track sampling is irregularly spaced. The periodogram isolates the most powerful frequency ranges in each volume component (i.e., edifice, infill, and underplating) and the total volumes. Power spectral peaks (Table 5.2) are only reported if they fall above the 90% confidence interval for false alarm probabilities (FAP), determined as the probability that a dataset with no signal and normally-distributed noise would yield a spectral peak due to random alignment of noise (Scargle, 1982). Spectral peaks with higher frequencies (smaller periods) than the reciprocal of half of the graphically-determined maximum temporal spacing between adjacent volcanoes along a hotspot track (e.g., the time it takes the tectonic plate to move half the distance between volcanoes) are excluded from the results; these peaks may be related to the details of the volume summation method or lithosphere- and smaller-scale magmatic processes, but are unlikely related to mantle plume dynamics. Note that one over the Nyquist frequency of our melt volume time series is always smaller than the above intra-volcano time. Additionally, we exclude periodicity peaks at frequencies approaching (>90%) the temporal length of the hotspot signal.

Our method for calculating volumetric contributions relies on several assumptions and expressly avoids accounting for many of the specific features or data sets at individual hotspots to maintain a melt volume flux estimate that is directly comparable between hotspots. While we acknowledge that our approach of not including all applicable data at a particular hotspot could be viewed as a weakness, we stress the importance of applying the same methodological analysis to global data sets to obtain measurements that can be reliably compared against each other.

Table 5.2: Melt volume spectral peaks

Hotspot	Edifice (Myr^{-1})	Infill (Myr^{-1})	Underplating (Myr^{-1})	Total volume spectral peaks (Myr^{-1})
Bowie	0.066	0.066		0.066
Cobb	0.12	0.12		0.12
Easter-Salas	0.067	0.067	0.057	0.067
	0.115	0.115	0.105	0.115
	0.163	0.163	0.153	0.153
	0.211	0.211	0.201	0.201
	0.393	0.393		0.393
Foundation	0.096	0.096	0.124	0.11
	0.165	0.165	0.193	0.179
	0.303	0.248	0.289	0.289
	0.358	0.303	0.675	0.358
	0.758	0.358	0.758	0.675
		0.427		0.758
		0.758		
Galápagos	0.098	0.098	0.11	0.11
	0.184	0.184	0.019	0.019
Hawaii	0.019	0.019	0.037	0.044
	0.044	0.044	0.047	0.062
	0.069	0.062	0.062	0.087
	0.084	0.069	0.075	0.106
	0.106	0.084	0.09	0.121
	0.121	0.106	0.106	0.146
	0.146	0.121	0.118	0.171
	0.174	0.146	0.143	0.19
	0.187	0.171	0.168	0.202
	0.224	0.187	0.202	0.221
	0.24	0.224	0.221	0.28
	0.255	0.237	0.246	0.311
	0.277		0.28	0.405
	0.311		0.308	0.42
	0.346		0.343	0.448
	0.383		0.383	0.464
	0.402		0.405	
	0.42		0.42	
	0.47		0.433	
			0.448	
			0.464	

Table 5.2 – continued from previous page

Hotspot	Edifice (Myr^{-1})	Infill (Myr^{-1})	Underplating (Myr^{-1})	Total volume spectral peaks (Myr^{-1})
			0.473	
Kerguelen	0.015	0.015	0.017	0.023
	0.023	0.023	0.029	0.044
	0.033	0.033	0.046	
Louisville	0.038	0.038		0.038
	0.055	0.055		0.055
	0.072	0.072		0.072
	0.137	0.137		0.137
	0.205	0.16		0.16
		0.201		0.201
Marquesas	0.373	0.373		0.373
	0.513			
	0.793			
Réunion	0.034	0.034	0.034	0.034
	0.064	0.064		0.064
St. Helena	0.031	0.031		0.031
	0.048	0.048		0.048
	0.073	0.073		0.073
Tristan	0.02	0.02	0.02	0.02
	0.033	0.033	0.038	0.033
	0.046	0.046		0.046
	0.071	0.071		0.096
	0.099	0.099		

5.3 Hotspot Results

Here we present our estimated melt fluxes, average melt fluxes, and spectral analyses of melt flux variations for each individual hotspot. Prior to these results, we present a short introduction to each hotspot with relevant information about the tectonic history and details of the underlying mantle plumes. We then present the comparative results of our combined study, which aims to compare relative volumetric outputs over time between different plumes.

5.3.1 Bowie

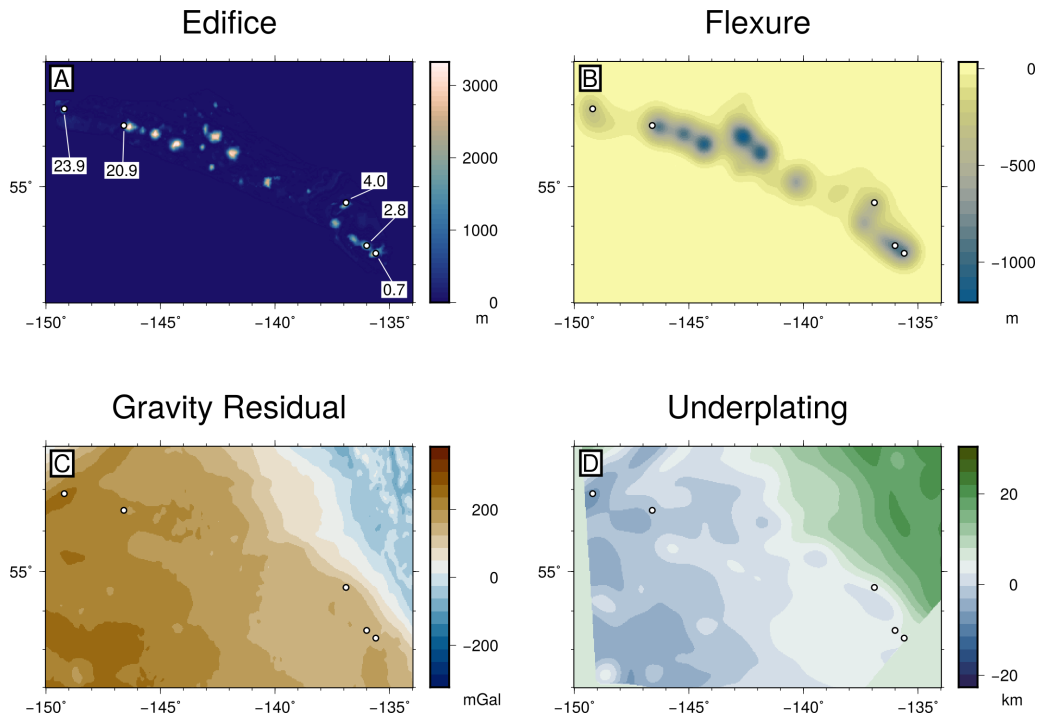

Figure 5.5: Resultant maps for Bowie hotspot. (A) Volcanic edifice and hotspot age samples. (B) Calculated flexure profile. (C) Gravity residual map. (D) Underplating relative thickness map

The Bowie hotspot track (also referred to as the Kodiak-Bowie Seamount Chain) strikes northwest across the northern Pacific Ocean from a presumed plume location of 53°N 135°W (Zhao, 2007) 5.5. P-wave travel time anomalies are interpreted to indicate the presence of a thermal anomaly of 300°C reaching beneath the 660 km discontinuity, suggesting a lower mantle origin of the Bowie plume (Nataf and Vandecar, 1993). Similarly, tomographic inversions find a low-velocity zone beneath the Bowie hotspot extending into the lower mantle (Zhao, 2007). At greater depths, a large low-velocity region extends from 1300 km depth to the core-mantle boundary, but its connection to shallower ($\leq$660 km) low velocity anomalies beneath the Bowie hotspot is tentative (Zhao, 2007). Based upon the gap in anomalously low velocities between 660 km and 1300 km depth, some

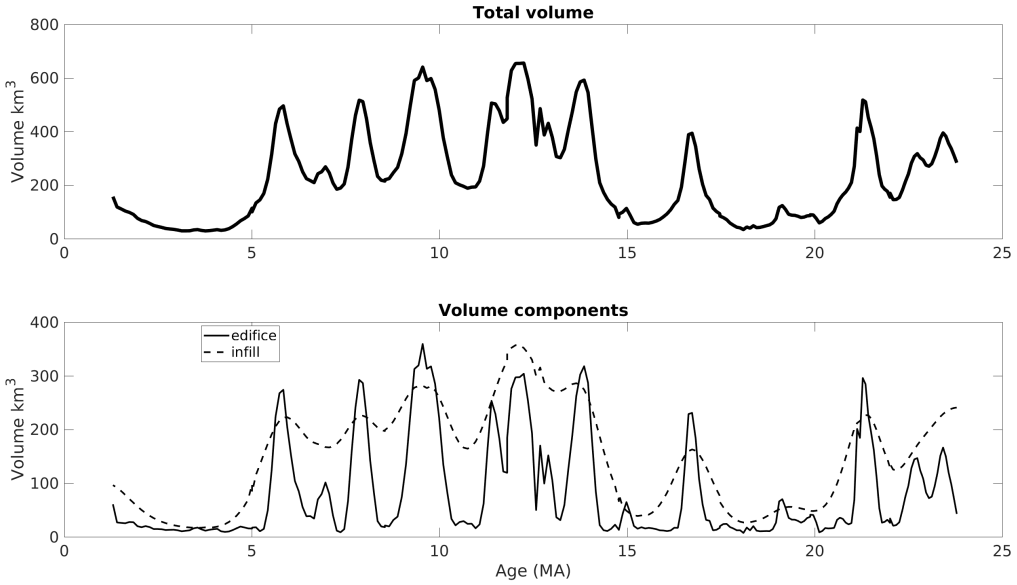

Figure 5.6: Bowie hotspot melt volumes with time. (Top) Total melt volume. (Bottom) Separated volume components

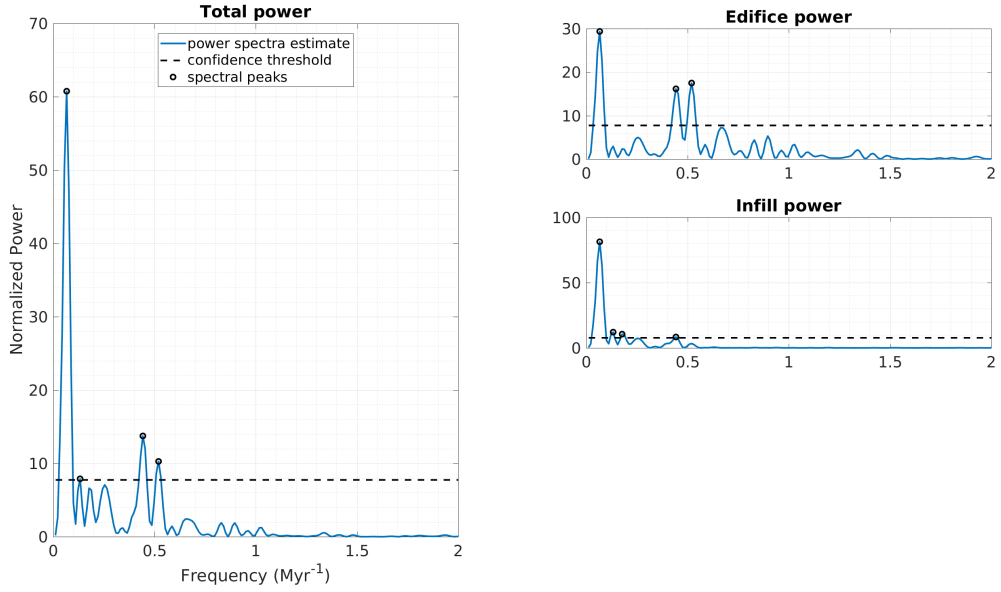

Figure 5.7: Power spectra for the Bowie hotspot. (Left) Total volume power spectra, with FAP confidence (dashed line) and spectral peaks (circles). (Right) Separated volume component power spectra.

studies argue that the Bowie plume is not rooted at the core-mantle boundary (Montelli et al., 2006). Sampled seamounts and one DSDP hole (DSDP 178) along the track provide K/Ar ages of 0–23 Myr (Turner et al., 1980).

Average melt flux for the Bowie hotspot track is 0.31 m^3/s. Melt volumes along the Bowie hotspot track vary over time, with low melt outputs from 5 Ma to 1 Ma. The Bowie hotspot volcanic edifice has one significant spectral peak at 0.066 Myr^{-1}. Other significant peaks occur at frequencies above the hotspot volcano spacing criterion and are discounted. Infill volume also exhibits a significant spectral peak at 0.066 Myr^{-1}, with additional peaks at frequencies of 0.210 Myr^{-1} and 0.310 Myr^{-1}. Underplating analysis at the Bowie hotspot yielded results below our minimum along-track average criterion. The sum of all volume contributions yields significant spectral peaks at 0.066, 0.199, and 0.310 Myr^{-1}.

5.3.2 Cobb

The Cobb hotspot track shares many characteristics with the nearby Bowie hotspot. The current hypothesized plume location is 46°N 130°W, coincident with Axial Seamount on the Juan de Fuca ridge (Zhao, 2007); the hotspot seamount track roughly parallels that of Bowie with a roughly northwest strike. There is an 800 km discontinuity in the seamount chain between the Eickelberg/Forster seamounts and Miller seamount (Desonie and Duncan, 1990). A connection between the Miller seamount and the Cobb hotspot was established based on the age of the seamount and its geochemical composition (Dalrymple et al., 1987). However, we do not include the Pathfinder-Gilbert-Parker seamount chain (located south/southeast of the Cobb-Eikelberg chain) in our analysis, as it is unclear from the single age constraint at Pathfinder whether this seamount chain is part of the Cobb hotspot (Dalrymple et al., 1987).

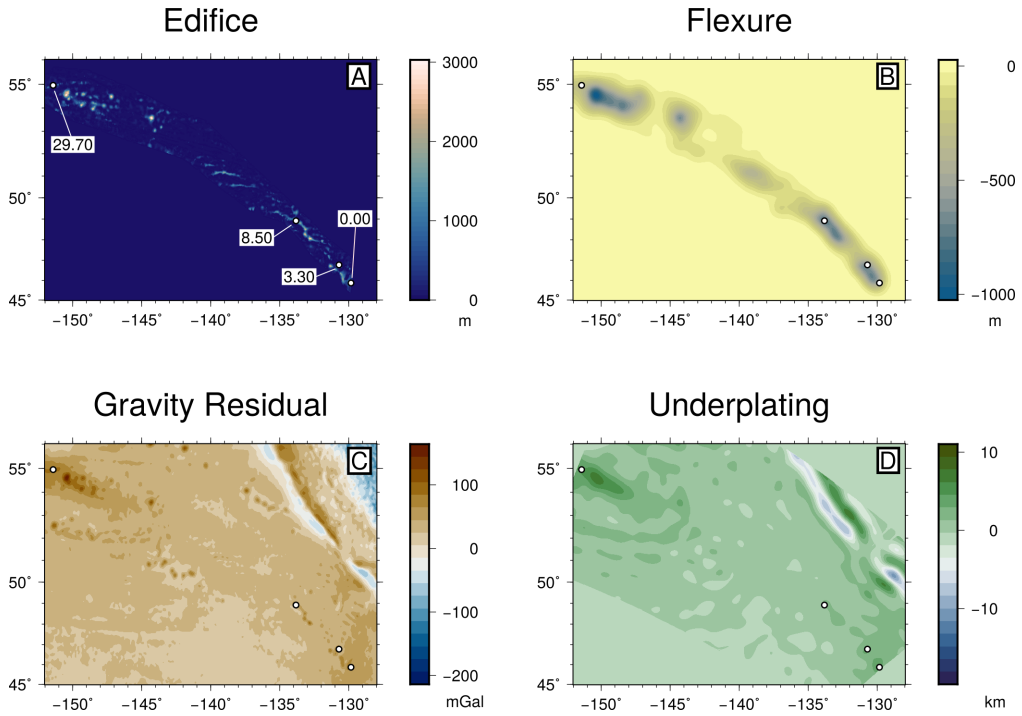

Figure 5.8: Resultant maps for Cobb hotspot. (A) Volcanic edifice and hotspot age samples. (B) Calculated flexure profile. (C) Gravity residual map. (D) Underplating relative thickness map

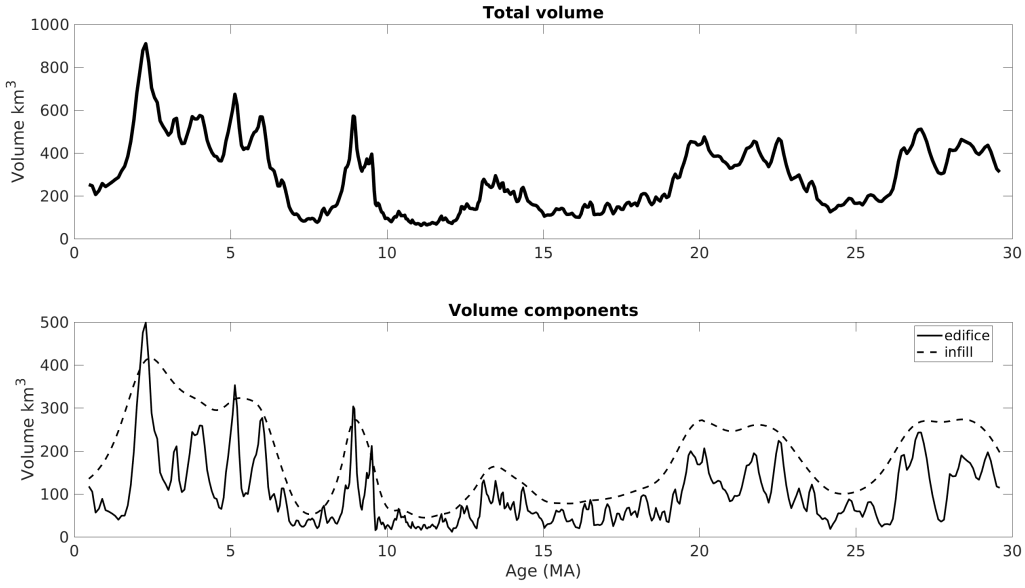

Figure 5.9: Cobb hotspot melt volumes with time. (Top) Total melt volume. (Bottom) Separated volume components

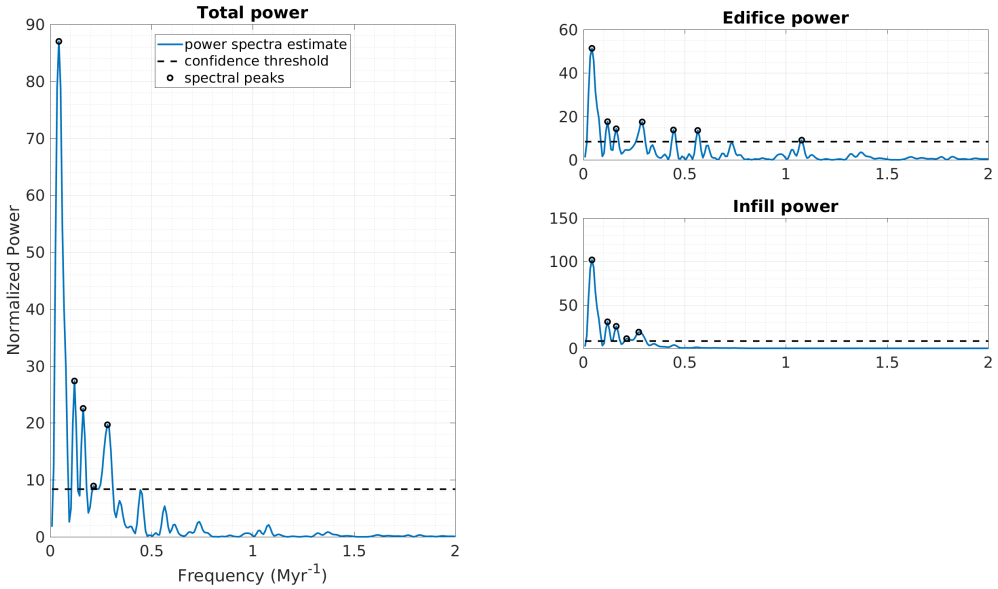

Figure 5.10: Power spectra for the Cobb hotspot. (Left) Total volume power spectra, with FAP confidence (dashed line) and spectral peaks (circles). (Right) Separated volume component power spectra.

Average melt flux for the Cobb hotspot track is 2.10 m^3/s. Melt volumes at Cobb are larger prior to 25 Ma and after 10 Ma, with a period of low melt output in between. Recent melt volumes show an increase in melt volumes relative to the period from 18–12 Ma. The Cobb hotspot volcanic edifice has one spectral peak at 0.120 Myr^{-1}, which also appears in the infill power spectra. Like the neighboring Bowie hotspot, no significant underplating signal can be distinguished. One total volume spectral peak exists for the Cobb hotspot at 0.120 Myr^{-1}.

5.3.3 Easter-Salas

The Easter-Salas hotspot track strikes east from a hypothesized plume located at 27°S 108°W (Montelli et al., 2006; Zhao, 2007) (though the exact location of the plume is debated (e.g., Ray et al. (e.g., 2012), Haase and Devey (1996), and Haase et al. (1996). Seismic velocity anomalies suggest the plume extends to a depth of 2800 km (Montelli et al., 2006), into the lower mantle (Zhao, 2007). The 30 Myr history of the Easter-

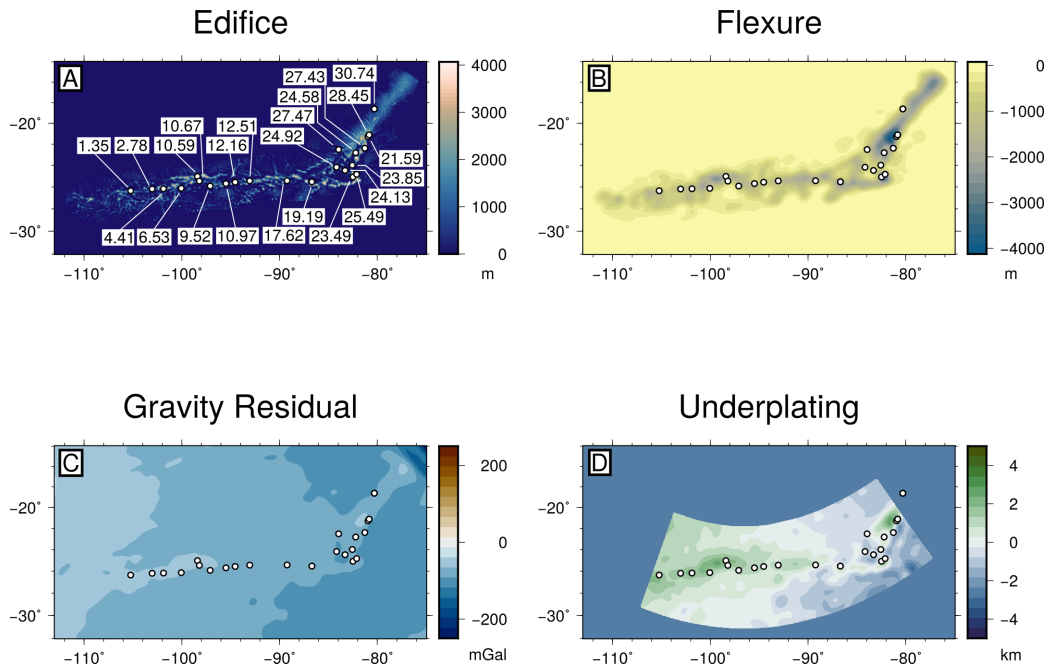

Figure 5.11: Resultant maps for Easter-Salas hotspot. (A) Volcanic edifice and hotspot age samples. (B) Calculated flexure profile. (C) Gravity residual map. (D) Underplating relative thickness map

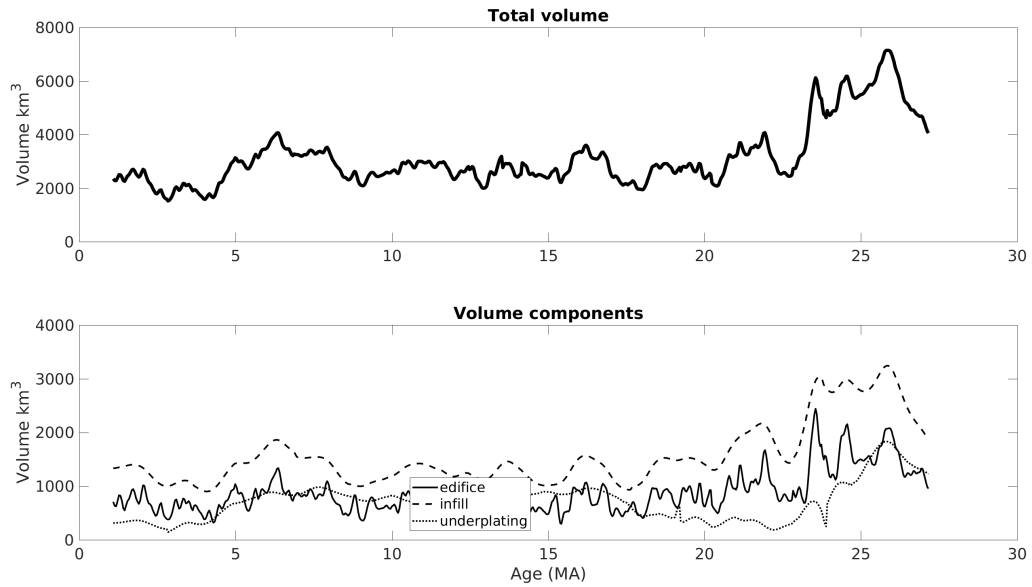

Figure 5.12: Easter hotspot melt volumes with time. (Top) Total melt volume. (Bottom) Separated volume components

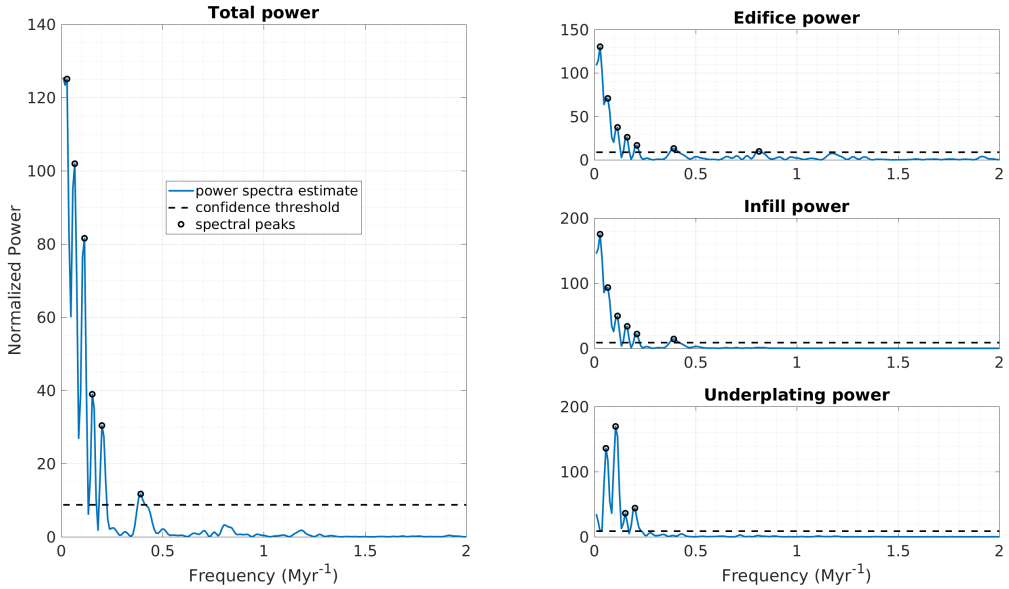

Figure 5.13: Power spectra for the Easter-Salas hotspot. (Left) Total volume power spectra, with FAP confidence (dashed line) and spectral peaks (circles). (Right) Separated volume component power spectra.

Salas hotspot track, as determined by Ar-Ar dated dredge samples (Ray et al., 2012), is complicated by tectonic processes, including crossing the Nazca FZ and past plate boundary reorganizations, which left the Easter microplate 100 km west of the youngest extent of hotspot-related volcanism (Kruse et al., 1997; Liu, 1996). A large bend in the hotspot track at the dividing line between the Nazca Ridge and the Easter Seamount Chain (now recognized as volcanic products of the same hotspot, O'Connor et al. (1995)) appears contemporaneous with breakup of the Farallon plate (Barckhausen et al., 2008) and a change in plate motion at 23 Ma (Wessel and Kroenke, 2000). The corresponding plume location is uncertain, some researchers invoke radiogenic isotope compositions at Salas y Gomez to support the claim that the hotspot is located nearest Salas y Gomez and that Easter Island is a manifestation of interaction between the plume and the adjacent spreading center (Kingsley et al., 2007; Kingsley et al., 2002; Hanan and Schilling, 1989; Fontignie and Schilling, 1991; Simons et al., 2002). Other researchers claim that the

volume of Easter Island relative to Salas y Gomez, radiogenic isotopic compositions, and the age progression of the Easter seamount chain supports a hotspot location at or even west of Easter Island (Haase and Devey, 1996; Haase et al., 1996). Plate reconstructions suggest a hotspot location nearer Salas y Gomez (Okal and Cazenave, 1985; Kruse et al., 1997), while tomographic images pins the location to a region between Easter and Salas y Gomez (Montelli et al., 2006). More recent geochemical observations (Ray et al., 2012) conclude that Salas y Gomez lavas are more representative of plume-derived melt compositions and, thus, the plume is likely located at or near Salas y Gomez. However, younger volcanic material exists west of Salas y Gomez (Haase and Devey, 1996) and we take the location of this younger volcanism as an anchoring point for the young end of the hotspot track.

Average melt flux for the Easter-Salas hotspot track is 10.2 m^3/s. After an initial peak in melt volume, the Easter-Salas hotspot track produces lesser melt volumes from 23–5 Ma. Significant volcanic edifice spectral peaks are observed at frequencies of 0.067, 0.115, 0.163, 0.211, and 0.393 Myr^{-1}. These spectral peaks are also present in the infill volumes. Peaks appear in the underplating spectrum at 0.057, 0.105, 0.153, and 0.201 Myr^{-1}. Total volume spectral peaks are observed at 0.067, 0.115, 0.153, 0.201, and 0.393 Myr^{-1}.

5.3.4 Foundation

The Foundation hotspot chain strikes west for 1350 km from its intersection with the Pacific-Antarctic spreading center at 38°S 111°W (O'Connor et al., 2004). Its 21 Myr history is interrupted by ridge interactions and transfer of the Selkirk microplate from the Nazca to the Pacific plate between 20-24 Ma (Mammerickx, 1992; Tebbens and Cande, 1997; Tebbens et al., 1997; O'Connor et al., 1998). Thus, the hotspot track crosses lithosphere with an age range of 17 Ma to 0 Ma (O'Connor et al., 1998). At 4 Ma, the

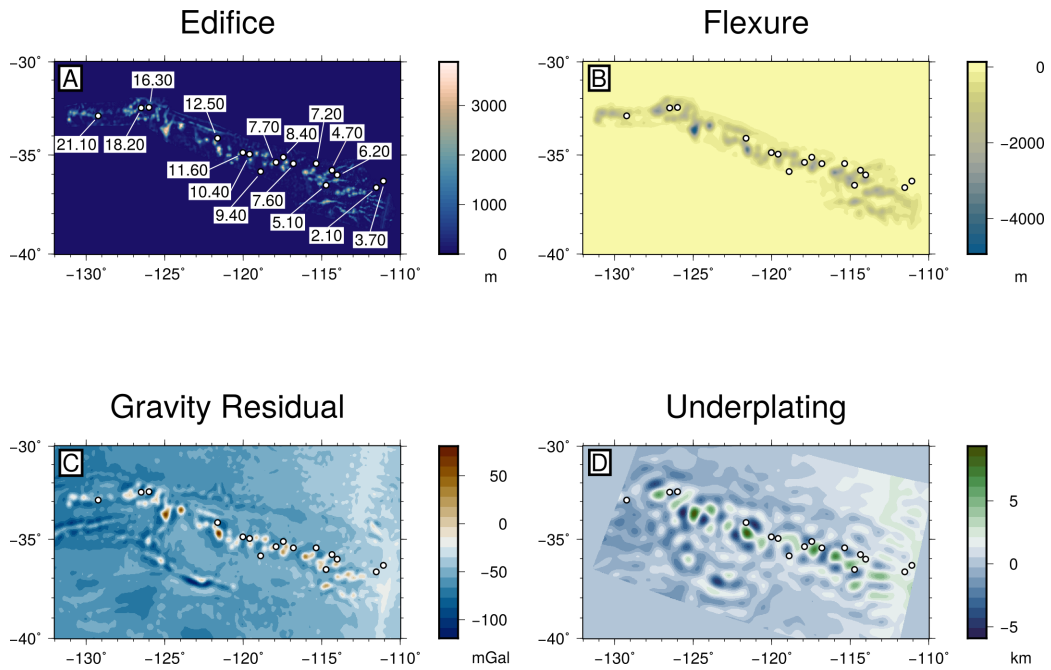

Figure 5.14: Resultant maps for Foundation hotspot. (A) Volcanic edifice and hotspot age samples. (B) Calculated flexure profile. (C) Gravity residual map. (D) Underplating relative thickness map

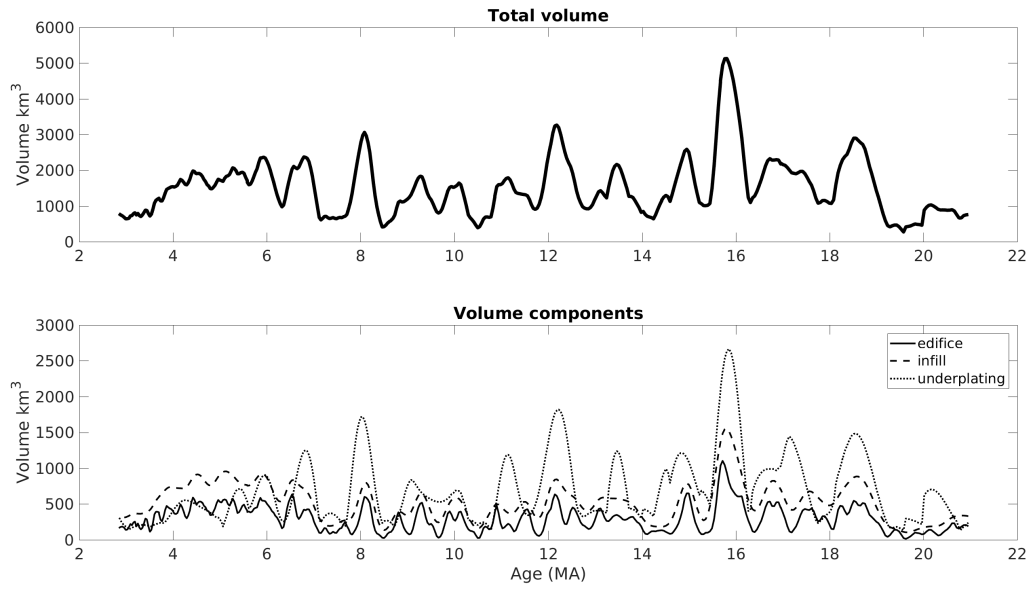

Figure 5.15: Foundation hotspot melt volumes with time. (Top) Total melt volume. (Bottom) Separated volume components

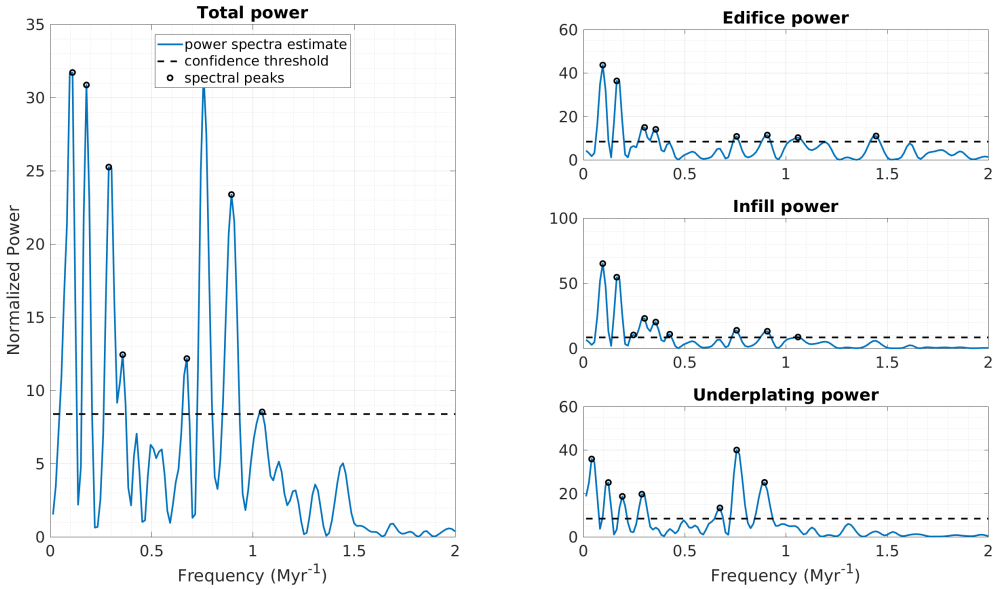

Figure 5.16: Power spectra for the Foundation hotspot. (Left) Total volume power spectra, with FAP confidence (dashed line) and spectral peaks (circles). (Right) Separated volume component power spectra.

hotspot began interacting with the approaching Pacific-Antarctic spreading center (Maia et al., 2000). Volcano morphology during this period shifted from discrete, individual edifices to elongate volcanic ridges, fingering towards the spreading center (Maia et al., 2000). Gravity-derived crustal thickness estimates indicate anomalously thick crust along portion of the spreading center closest to the hotspot track, suggesting that the plume contributes significant material to axial-produced crust (Maia et al., 2000).

Average melt flux for the Foundation hotspot track is 4.90 m^3/s. Melt volumes vary over time with a decrease in the amplitude of variation from 5 Ma to 3 Ma. Significant volumetric power spectra peaks occur in the Foundation volcanic edifice and infill volumes at 0.096, 0.165, 0.303, 0.358, and 0.758 Myr^{-1}. Two additional spectral peaks are observed in the infill volumes at 0.248 and 0.427 Myr^{-1}. Underplating volumes have significant spectral peaks at frequencies of 0.096, 0.165, 0.248, 0.303, 0.358, 0.427, and 0.758 Myr^{-1}.

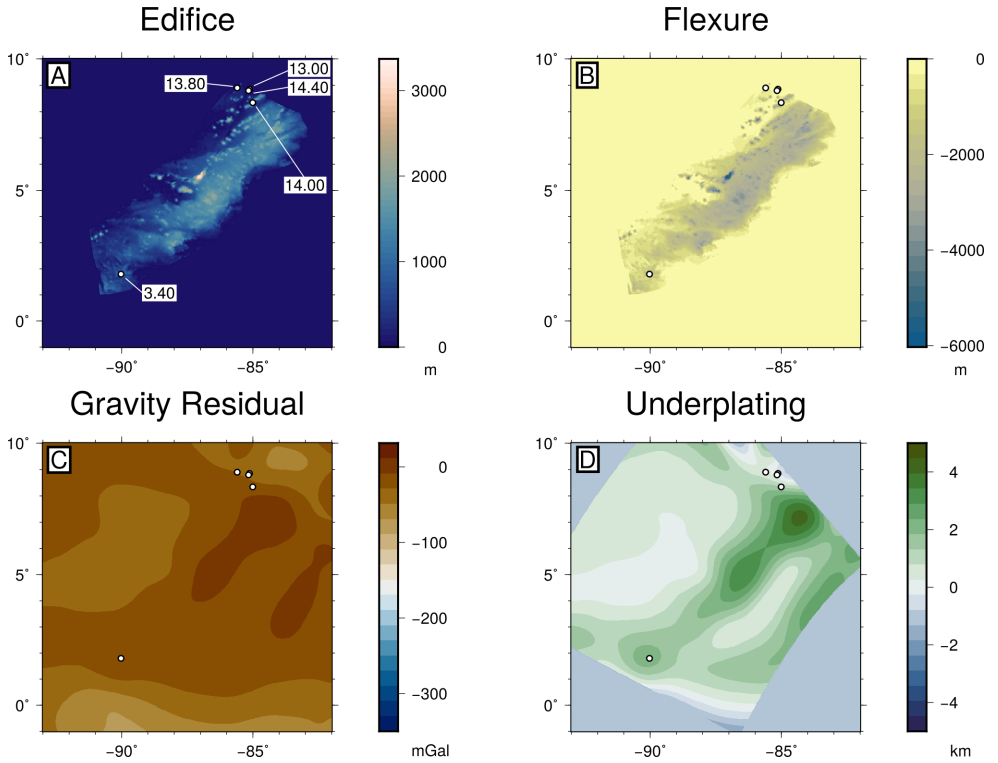

Figure 5.17: Resultant maps for the Cocos track of the Galápagos hotspot. (A) Volcanic edifice and hotspot age samples. (B) Calculated flexure profile. (C) Gravity residual map. (D) Underplating relative thickness map

The total volumetric output at Foundation has spectral peaks at 0.124, 0.193, 0.289, 0.675, and 0.758 Myr^{-1}.

5.3.5 Galápagos

Produced by the mantle plume located at approximately 0°N 92°W, the Galápagos hotspot track is strongly influenced by a history of plume-ridge interaction (Detrick et al., 2002; Sinton et al., 2003; Mittelstaedt et al., 2012). The east-west oriented Galápagos spreading center is located 200 km north of the current plume location and is migrating northeast relative to the plume. Hotspot material lies north and south of the Galápagos spreading center on both the Cocos and Nazca plates (Hoernle et al., 2000). The separated volcanic tracks strike east (Nazca track) and east-northeast (Cocos plate). The oldest expression of the hotspot we consider in our analysis is Malpelo Ridge, located

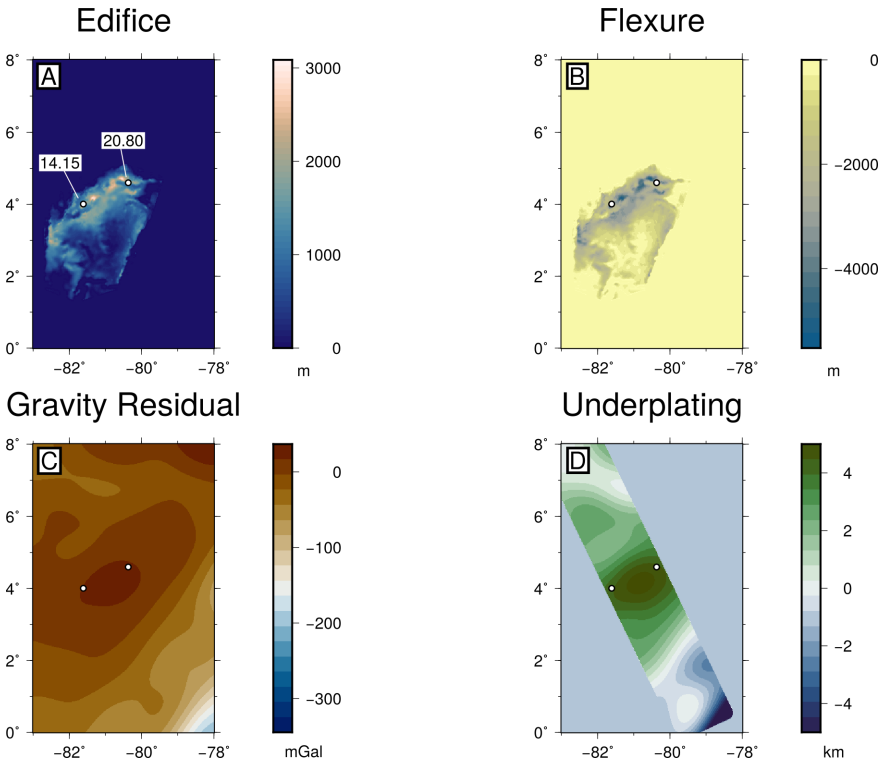

Figure 5.18: Resultant maps for the Malpelo track of the Galápagos hotspot. (A) Volcanic edifice and hotspot age samples. (B) Calculated flexure profile. (C) Gravity residual map. (D) Underplating relative thickness map

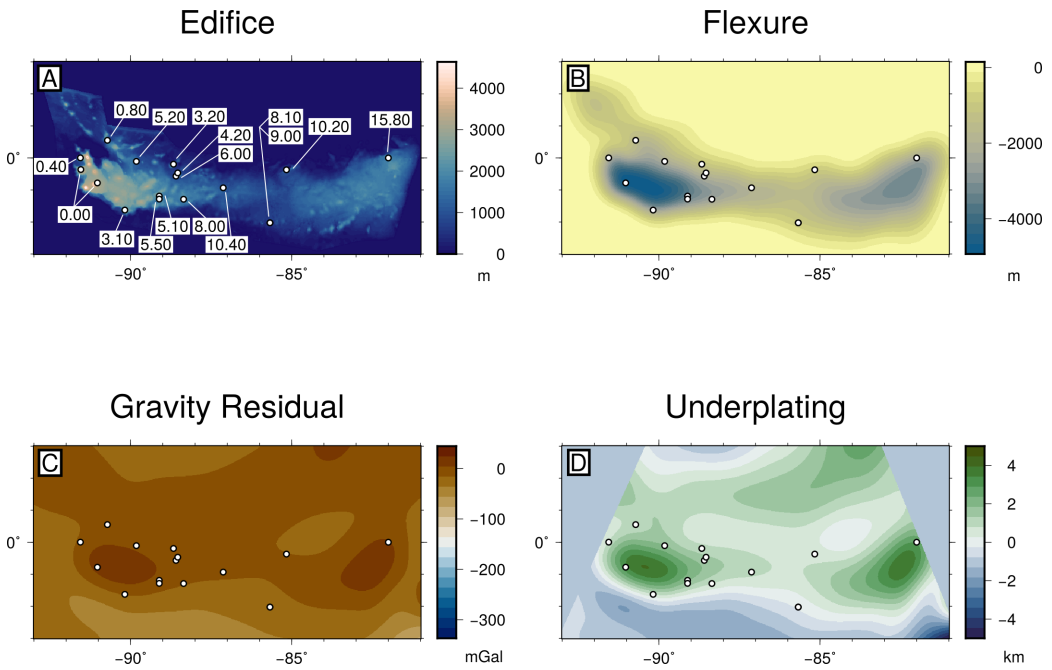

Figure 5.19: Resultant maps for the Nazca track of the Galápagos hotspot. (A) Volcanic edifice and hotspot age samples. (B) Calculated flexure profile. (C) Gravity residual map. (D) Underplating relative thickness map

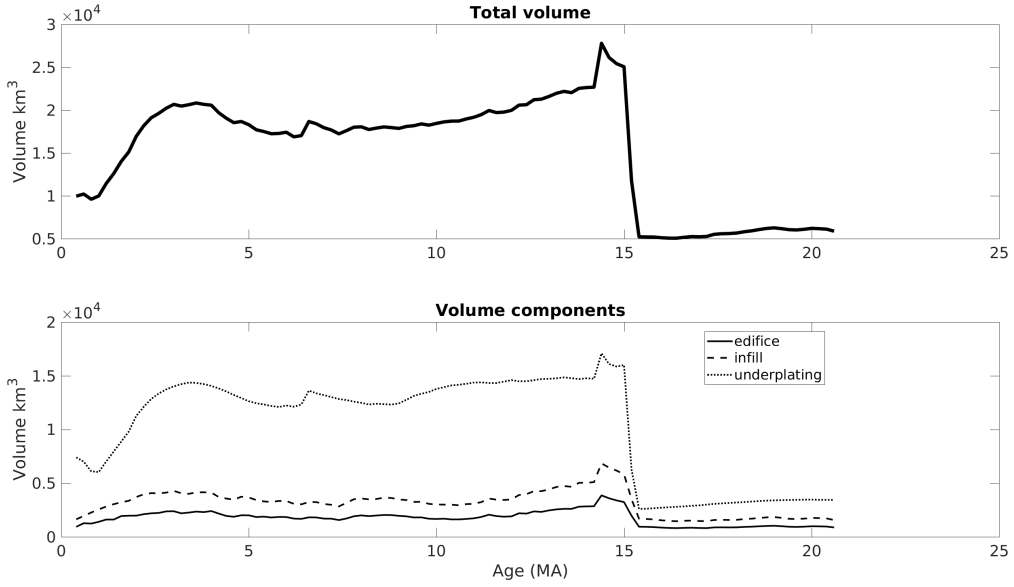

Figure 5.20: Galápagos hotspot melt volumes with time. (Top) Total melt volume. (Bottom) Separated volume components

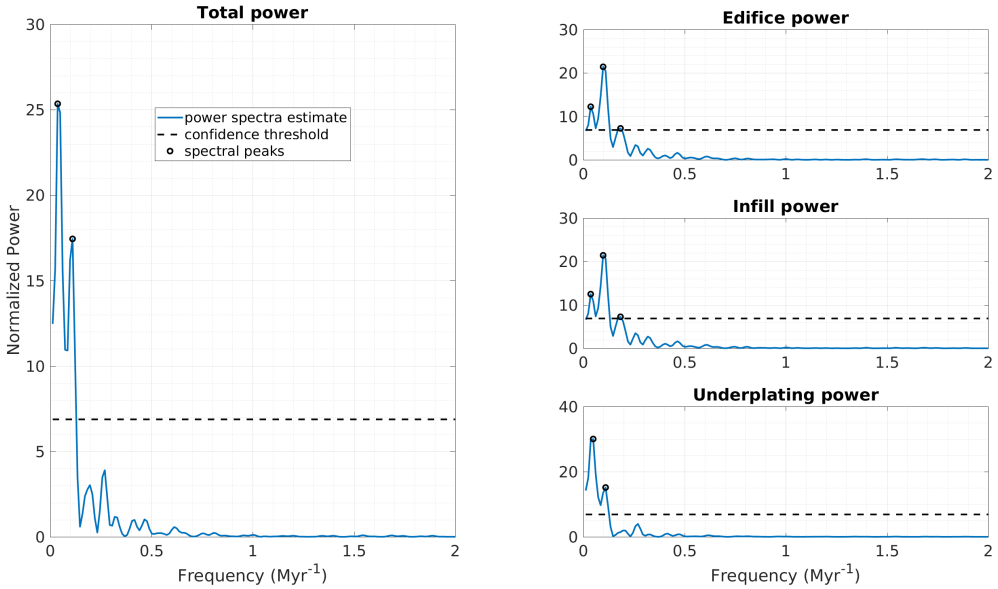

Figure 5.21: Power spectra for the Galápagos hotspot. (Left) Total volume power spectra, with FAP confidence (dashed line) and spectral peaks (circles). (Right) Separated volume component power spectra.

north of Ecuador, immediately adjacent to the Panama Fracture Zone, on the Cocos plate. Malpelo Ridge is believed to be a remnant of the Galápagos hotspot track that has since been isolated from the two other volcanic ridges by ridge jumps and spreading reorganizations (Lonsdale and Fornari, 1980). Limited sampling yields age constraints for Malpelo Ridge around 15–17 Ma. On the Cocos plate, the volcanic expression of the Galápagos hotspot stretches from the Galápagos Transform Fault along the Galápagos Spreading Center northeast towards Costa Rica, where Galápagos-derived seamounts intersect the Middle America Trench (Werner et al., 1999) and accreted on-shore volcanics bear geochemical signatures of the Galápagos plume (Hoernle et al., 2000). On the Nazca plate, the oldest Galápagos expression aside from Malpelo Ridge is the Carnegie Ridge (15 Ma, Sallarès (2003)), an east-west oriented aseismic feature (Sallarès et al., 2005). Current hotspot activity is focused on the western end of the Carnegie ridge where the Galápagos Archipelago sits atop the Galápagos platform, a 3 km thick plateau of basaltic

lava flow (Geist et al., 2008). Tomographic imaging (Zhao, 2007) reveals a low velocity zone underneath the Galápagos hotspot that extends below the 660 km discontinuity. Surface wave tomography images indicate the Galápagos plume is currently tilted towards the Galápagos Spreading Center and its estimated buoyancy flux is at least 2000 kg/s (Villagómez et al., 2007; Villagómez et al., 2014).

Average melt flux for the Galápagos hotspot track is 11.4 m^3/s. Melt output before 15 Myr is constrained only for the Malpelo Ridge. At younger ages, combined Galápagos melt volumes on both the Cocos and Nazca plates are relatively constant, with a notable decrease over the past 2 Myr. The combined Galápagos power spectra (including both Cocos and Nazca tracks) has two spectral peaks in the edifice volume expression at 0.098 and 0.184 Myr^{-1} which is shared with the infill power spectrum. One spectral peak is resolved in the underplating spectrum at 0.119 Myr^{-1} . The total volume expression for the Galápagos hotspot has one spectral peak at 0.110 Myr^{-1} .

5.3.6 Hawaii

The Hawaiian hotspot has been active for >80 million years, leaving a volcanic hotspot trace along the Pacific plate from the hotspot's current location (19.4°N 155.3°W) through the Emperor seamounts to eventual subduction at the Aleutian arc. Beneath the proposed plume location, a well-resolved low-velocity zone extends to the core-mantle boundary (Zhao, 2007). The Hawaiian hotspot track crosses multiple FZs, remnants of the Pacific-Farallon spreading center, that may influence melt production in the rising plume (Ballmer et al., 2011).

Average melt flux for the Hawaiian hotspot track is 3.45 m^3/s. Melt volumes along the Hawaiian hotspot track are highly variable, with a marked increase in melt production from 5 Ma to the present. The Hawaiian hotspot has many more spectral peaks than the other hotspots examined. Instead of listing each separately, the reader is referred to Table

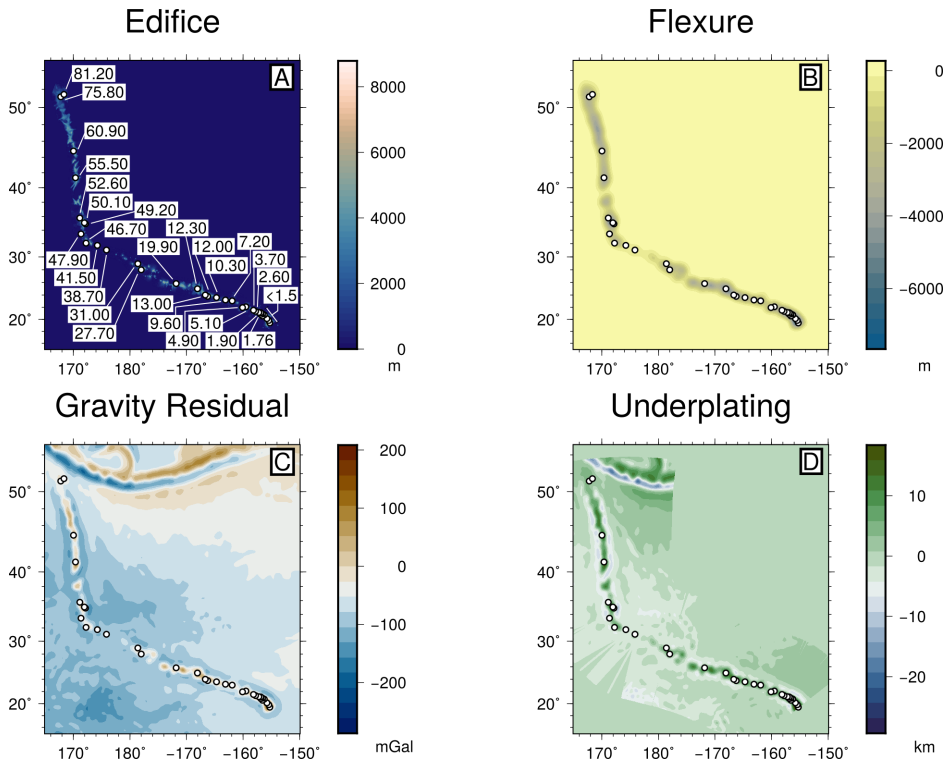

Figure 5.22: Resultant maps for Hawaii hotspot. (A) Volcanic edifice and hotspot age samples. (B) Calculated flexure profile. (C) Gravity residual map. (D) Underplating relative thickness map

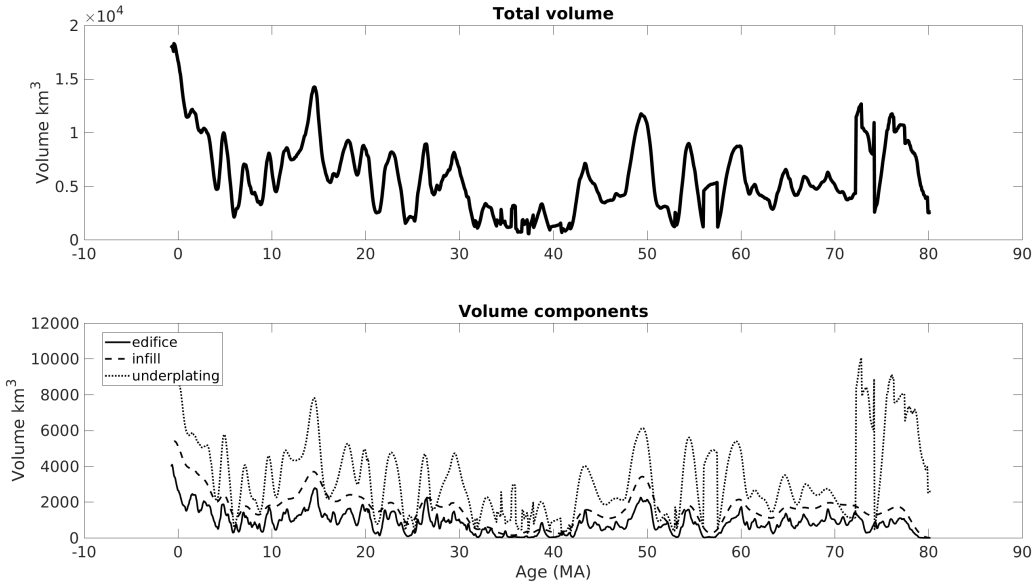

Figure 5.23: Hawaii hotspot melt volumes with time. (Top) Total melt volume. (Bottom) Separated volume components

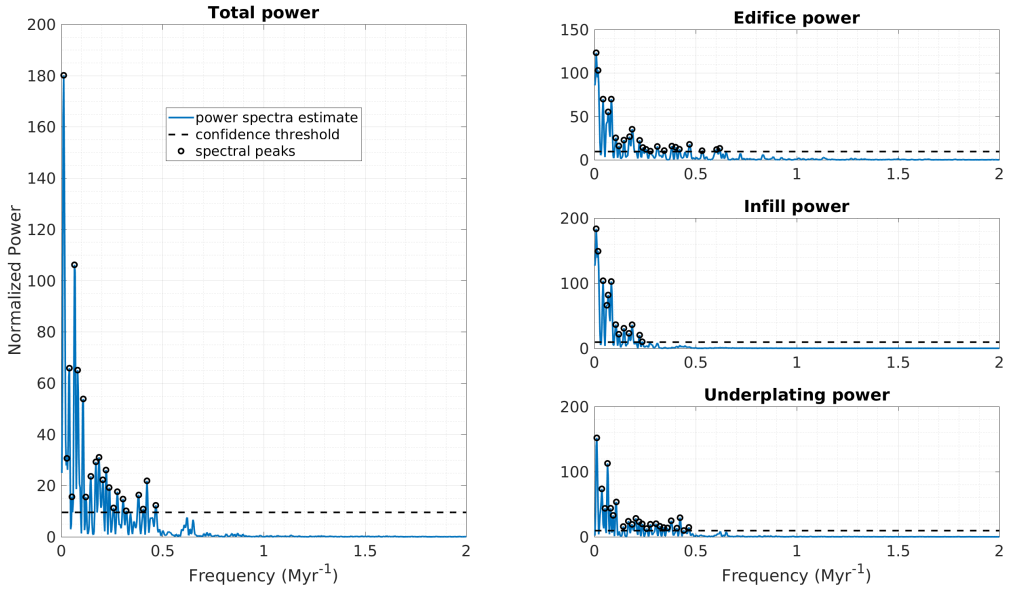

Figure 5.24: Power spectra for the Hawaii hotspot. (Left) Total volume power spectra, with FAP confidence (dashed line) and spectral peaks (circles). (Right) Separated volume component power spectra.

5.2. The edifice volumetric output power spectra has 19 spectral peaks. The infill volume power spectra has 12 peaks (Table 5.2) and the underplating volume power spectra has 23 peaks (Table 5.2). There are 17 power spectral peaks in the total melt volume for the Hawaiian hotspot track.

5.3.7 Kerguelen

The Kerguelen plume is currently located at 49.0°S, 69.0°E (Zhao, 2007), with a complex hotspot track separated by plate motion changes, leaving hotspot-attributed material on the Antarctic, Australian, and Indian plates. The oldest hotspot material comprises the Kerguelen Large Igneous Province, the Bunbury basalts on the Australian continent (Frey et al., 1996; Ingle et al., 2002; Coffin et al., 2002), the Lamprophyres on the Antarctic continent (Storey et al., 1989; Kent, 1991), and the Rajmahal traps Müller et al., 1993; Mahoney et al., 1983; Kent, 1991 on the Indian continent. From 130 Ma to 40 Ma, the Kerguelen hotspot was co-located with the Southwest Indian Ridge. A

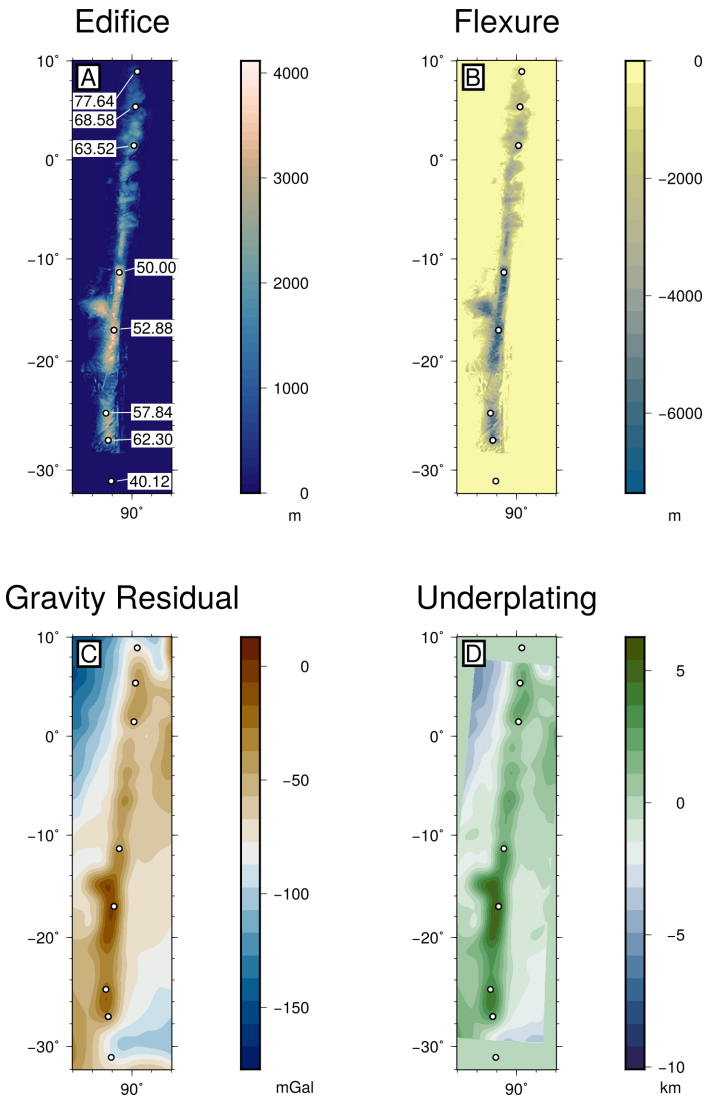

Figure 5.25: Resultant maps for the NinetyEast Ridge along the Kerguelen hotspot track. (A) Volcanic edifice and hotspot age samples. (B) Calculated flexure profile. (C) Gravity residual map. (D) Underplating relative thickness map

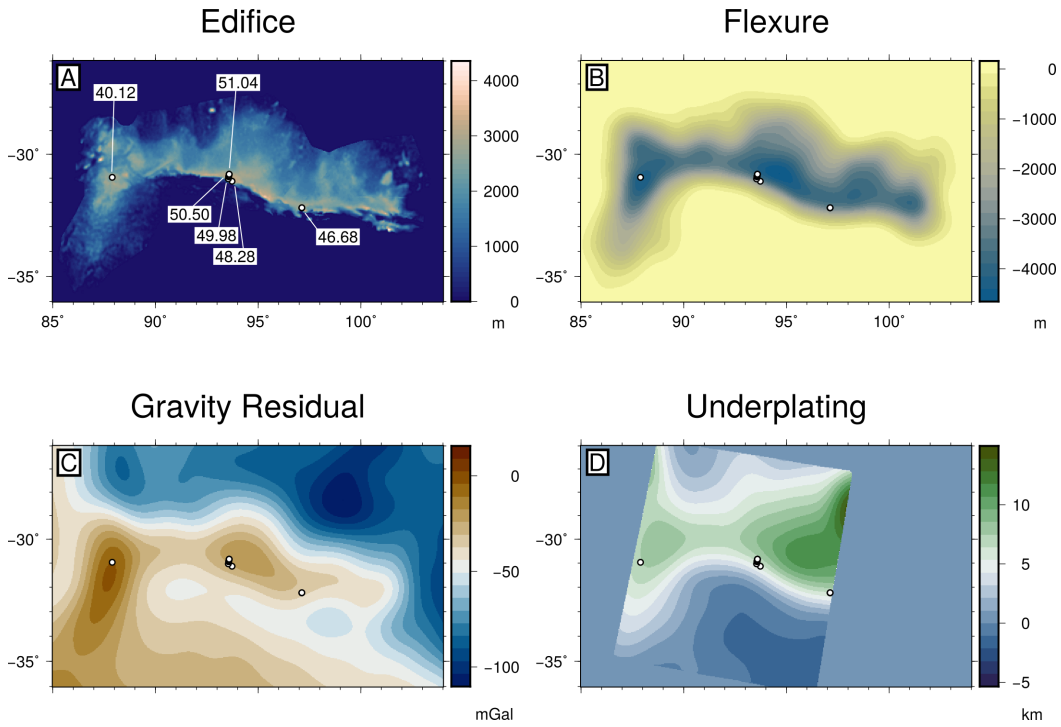

Figure 5.26: Resultant maps for Broken Ridge along the Kerguelen hotspot track. (A) Volcanic edifice and hotspot age samples. (B) Calculated flexure profile. (C) Gravity residual map. (D) Underplating relative thickness map

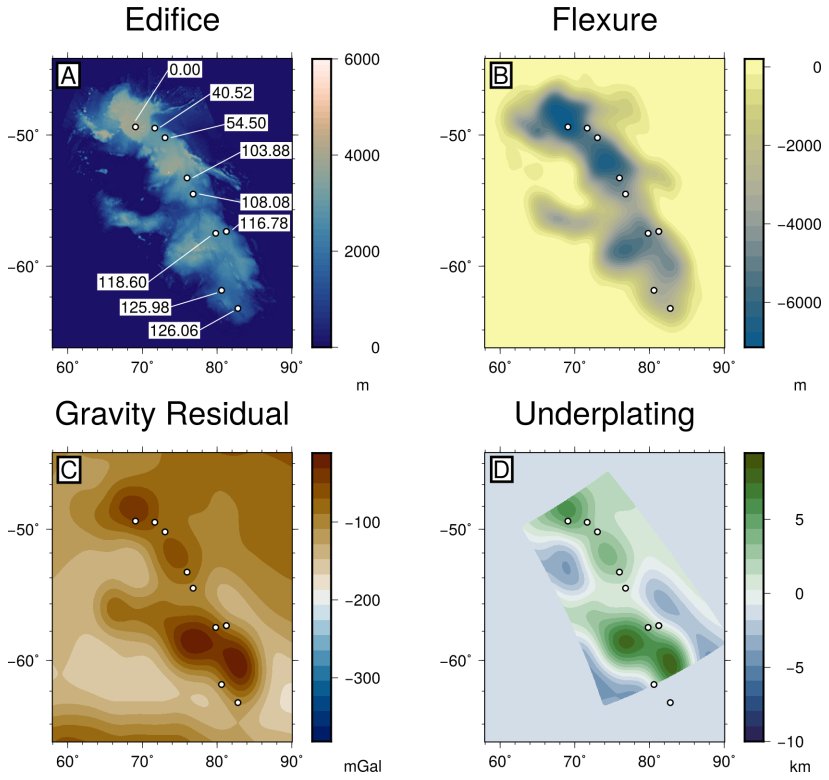

Figure 5.27: Resultant maps for the Kerguelen Plateau along the Kerguelen hotspot track. (A) Volcanic edifice and hotspot age samples. (B) Calculated flexure profile. (C) Gravity residual map. (D) Underplating relative thickness map

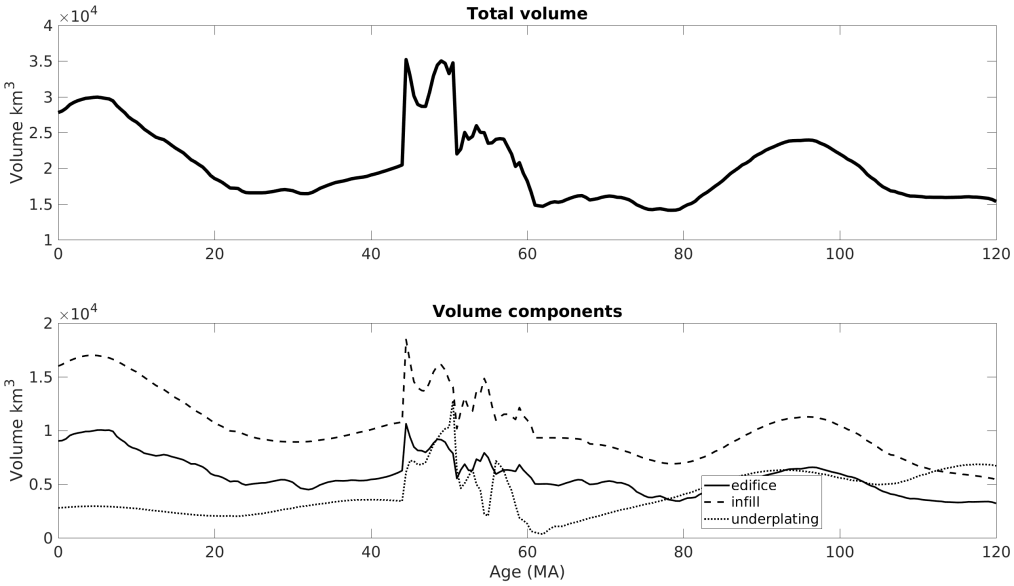

Figure 5.28: Kerguelen hotspot melt volumes with time. (Top) Total melt volume. (Bottom) Separated volume components

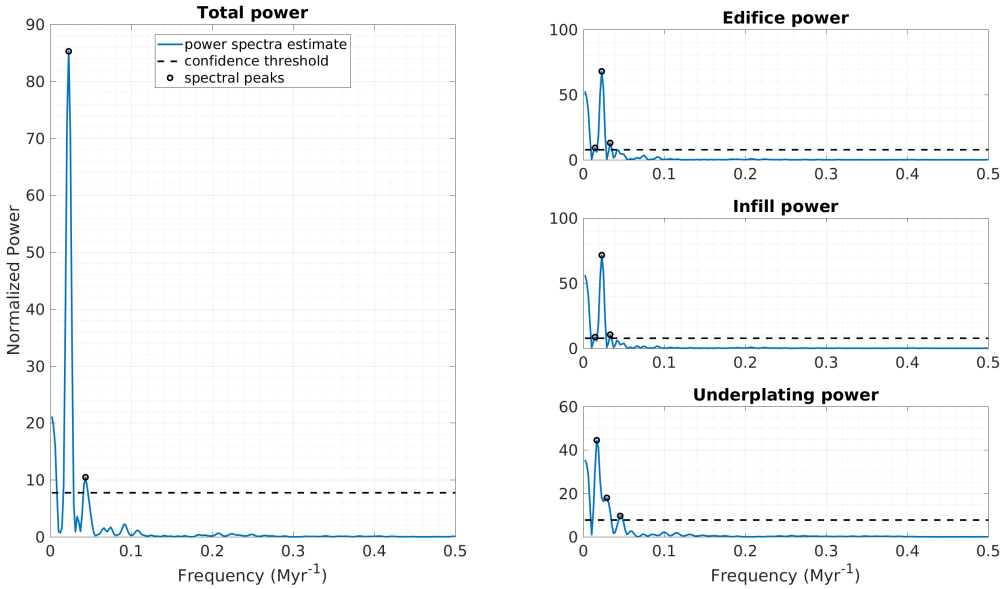

Figure 5.29: Power spectra for the Kerguelen hotspot. (Left) Total volume power spectra, with FAP confidence (dashed line) and spectral peaks (circles). (Right) Separated volume component power spectra.

series of ridge jumps and seafloor spreading has since separated the Kerguelen plateau from Broken Ridge and Ninety East Ridge, leaving a swath of volcanic material on the Indian plate and material spanning 130 Ma to present day on the Antarctic plate. In our analysis, we consider the Ninety East ridge, trending northwards from its termination at Broken Ridge (Coffin et al., 2002) and the Kerguelen plateau, which hosts the Kerguelen archipelago, considered the youngest and current volcanic expression of the plume (Coffin et al., 2002). We ignore hotspot material emplaced on continental crust.

Average melt flux for the Kerguelen hotspot track is 5.14 m^3/s. Melt volumes are relatively constant with two broad peaks at 90 Ma and 5 Ma. A period of plume-ridge interaction from 60–45 Ma briefly increases melt volumes. The Kerguelen hotspot edifice volumetric output power spectra has peaks corresponding to frequencies of 0.015, 0.023, and 0.033 Myr^{-1} which also appear as peaks in the infill volume power spectrum. Un-

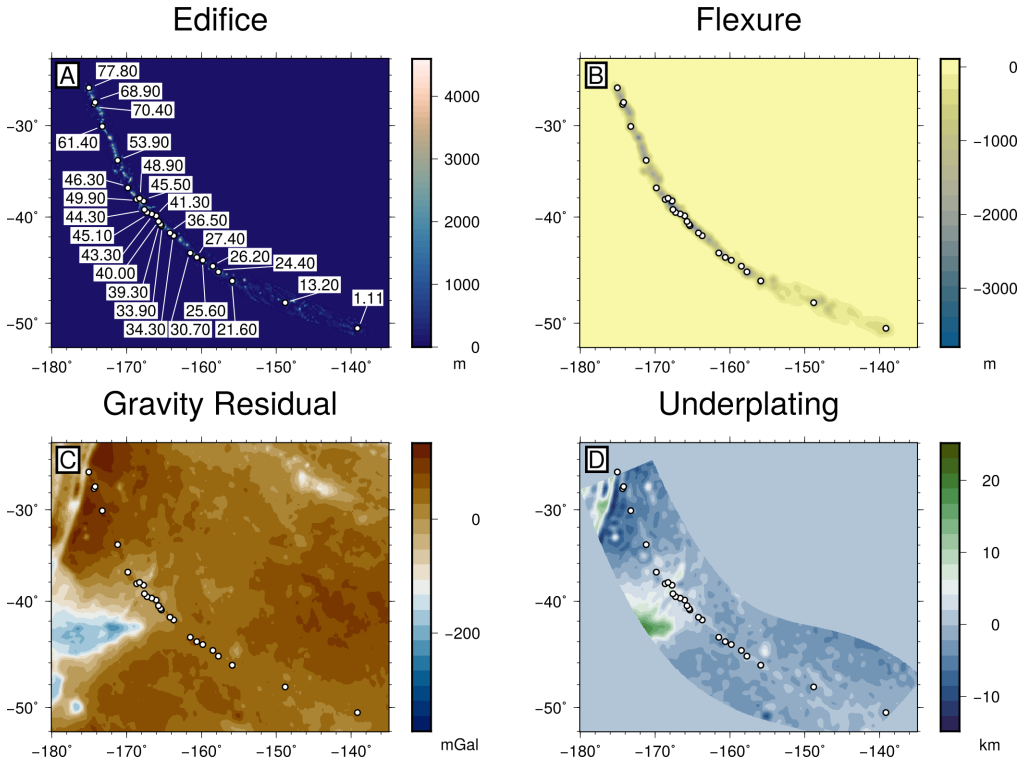

Figure 5.30: Resultant maps for Louisville hotspot. (A) Volcanic edifice and hotspot age samples. (B) Calculated flexure profile. (C) Gravity residual map. (D) Underplating relative thickness map

derplating power spectral peaks are at 0.017, 0.029, and 0.046 Myr^{-1}. Total volumetric spectral peaks are 0.023 and 0.044 Myr^{-1}.

5.3.8 Louisville

The 4300 km long Louisville hotspot track ranges from the present-day presumed plume location in the south-central Pacific (51°S 138°W) to the Tonga-Kermadec Trench, where its oldest expression (>70 Ma, Koppers et al. (2004) and Koppers et al. (2011)) is subducting atop 90 Myr old crust ((Müller et al., 2008). Morphologically, it is a curvilinear chain of isolated 4200-4500 m tall seamounts (Menard, 1964) with two bends at 169°W and 159°W (Lonsdale, 1988). Lonsdale (1988) indicated that crossing fracture zones do not appear to influence melt production, but Beier et al. (2011) show in geochemical observations that lithosphere thickness (and intervening fracture zones) likely controls

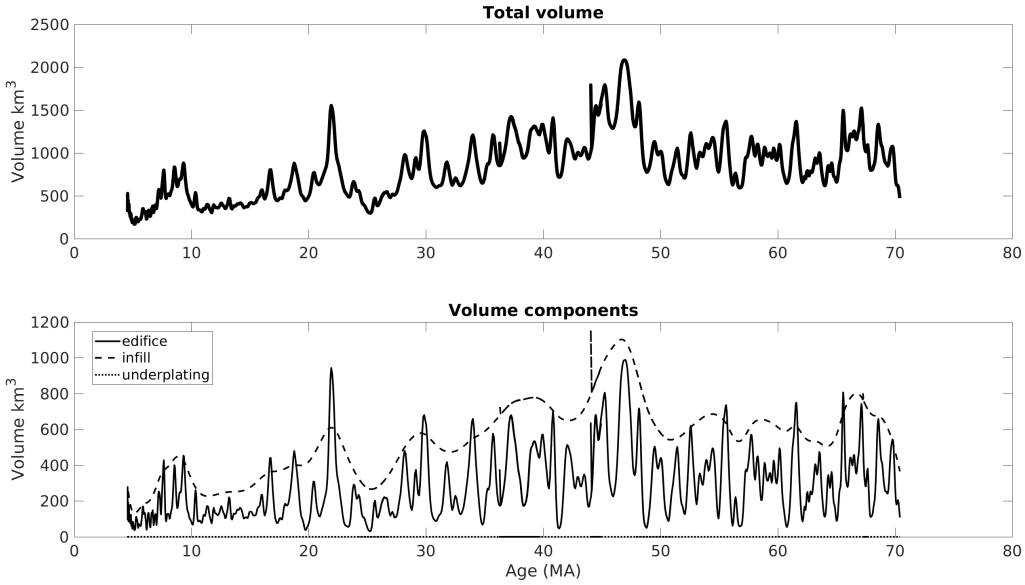

Figure 5.31: Louisville hotspot melt volumes with time. (Top) Total melt volume. (Bottom) Separated volume components

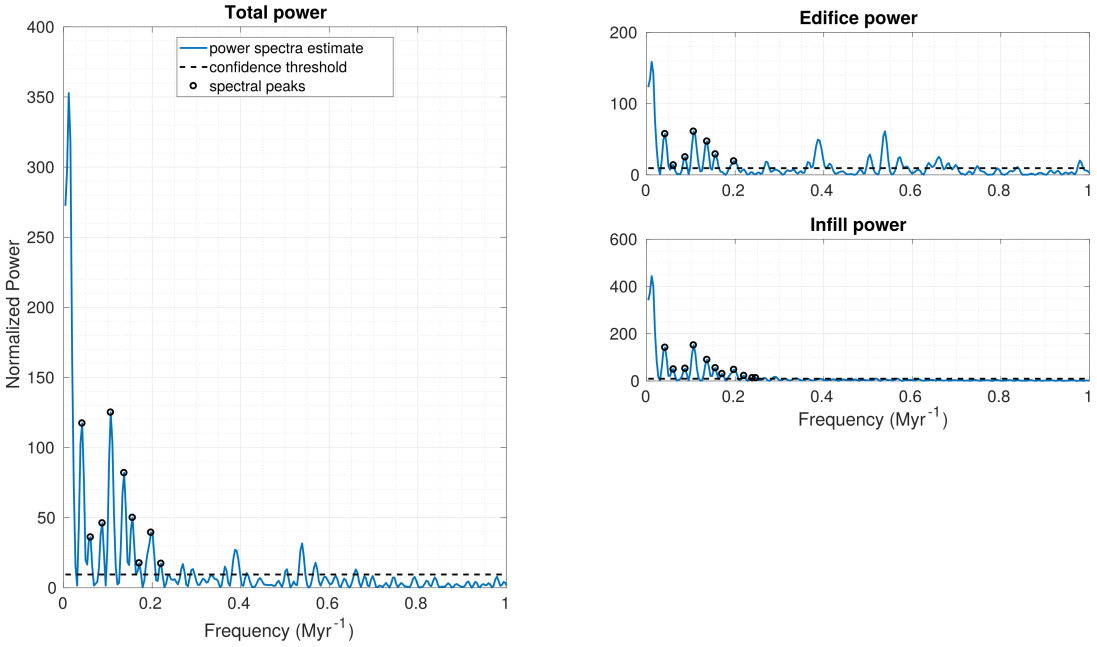

Figure 5.32: Power spectra for the Louisville hotspot. (Left) Total volume power spectra, with FAP confidence (dashed line) and spectral peaks (circles). (Right) Separated volume component power spectra.

degrees of partial melting along the Louisville hotspot track. Tomographic images (Zhao, 2007) indicate a low-velocity zone consistent with a Louisville plume that extends to the core mantle boundary. Previous examination of melt flux along the Louisville chain suggests waning melt production since 45 Ma (Koppers et al., 2004; Beier et al., 2011).

Average melt flux for the Louisville hotspot track is 1.84 m^3/s. Melt volumes vary but decrease overall starting around 40 Ma. Underplating analysis at Louisville yielded an along-track average thickness less than the minimum reporting criterium. Significant power spectral peaks in Louisville hotspot volcanic edifice occur at 0.038, 0.055, 0.072, 0.137, and 0.205 Myr^{-1}. Significant infill spectral peaks include 0.038, 0.055, 0.072, 0.137, 0.160, and 0.201 Myr^{-1}. No underplating peaks are reported. The Louisville total volumetric power spectra has spectral peaks at frequencies of 0.038, 0.055, 0.072, 0.137, 0.160, and 0.201 Myr^{-1}.

5.3.9 Marquesas

The relatively short Marquesas hotspot track covers 6 Myr of history. The track strikes northwest from the presumed plume location beneath the Marquesas FZ at 11°S 138°W in the Pacific Ocean. It has been proposed that the Marquesas track is also related to more distant volcanic expressions in the Hess Ridge and Shatsky Rise (Clouard, 2001) but these links are tentative and based on loosely-inferred plate motions (Sager and Han, 1993); other hotspots are also attributed as the origin of Shatsky Rise volcanics. Our analysis is restricted to the most recent Marquesas volcanism ((Révillon et al., 2017) located adjacent to the contemporary plume expression and extending to the oldest eruptive material from Eiao island (Guillou et al., 2014). Although more detailed ages are available (Guillou et al., 2014), they are at a higher resolution than our method. The source of Marquesas volcanism is revealed by tomographic images showing a low velocity region beneath the hotspot that extends to the core mantle boundary (Zhao, 2007).

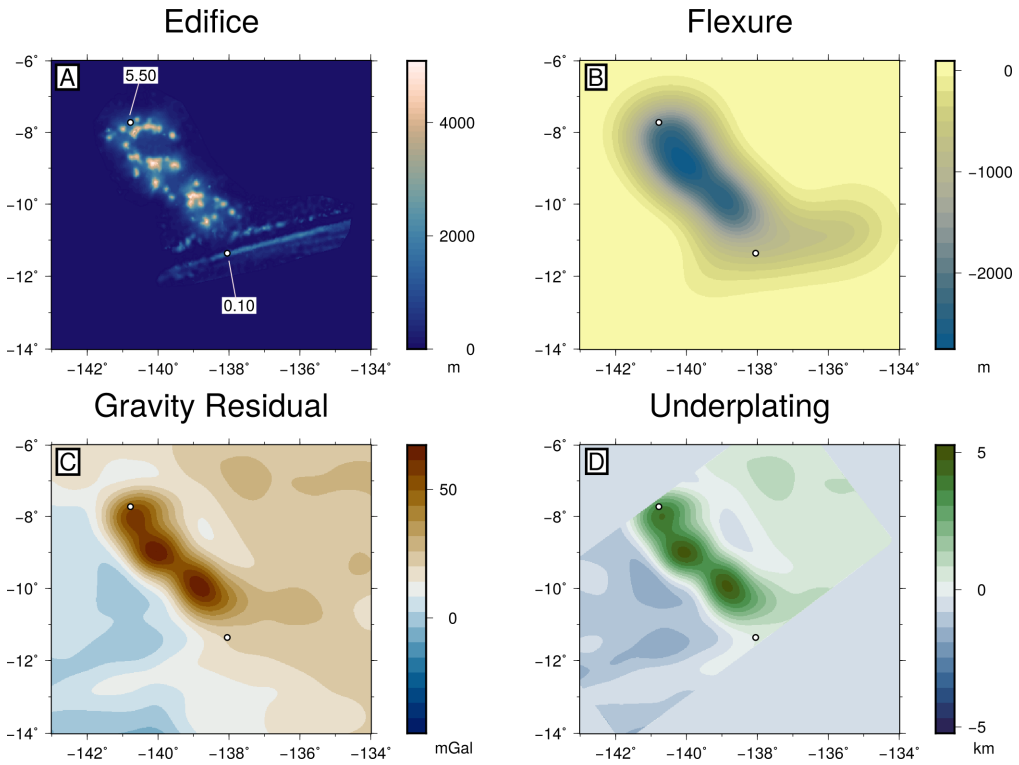

Figure 5.33: Resultant maps for Marquesas hotspot. (A) Volcanic edifice and hotspot age samples. (B) Calculated flexure profile. (C) Gravity residual map. (D) Underplating relative thickness map

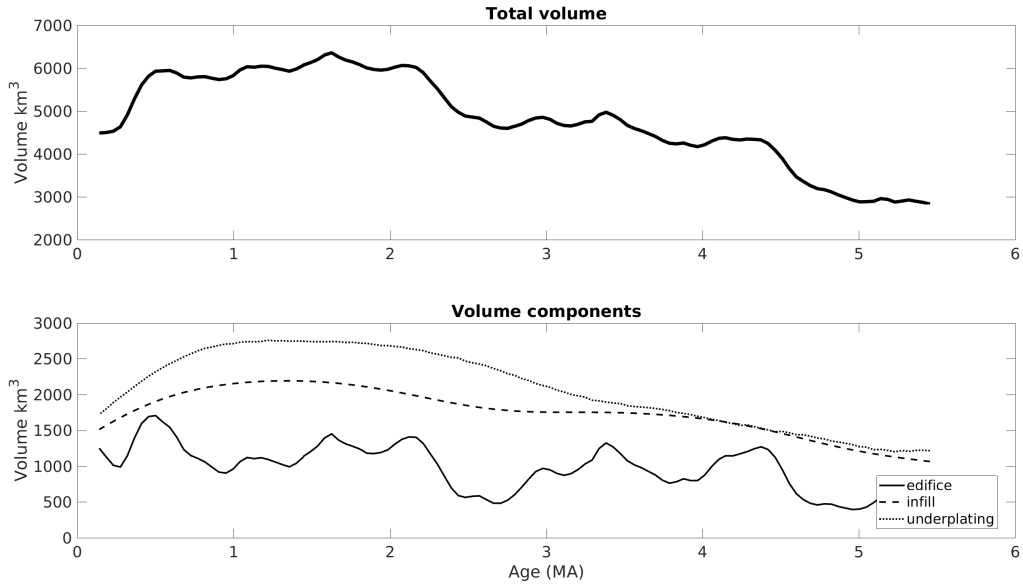

Figure 5.34: Marquesas hotspot melt volumes with time. (Top) Total melt volume. (Bottom) Separated volume components

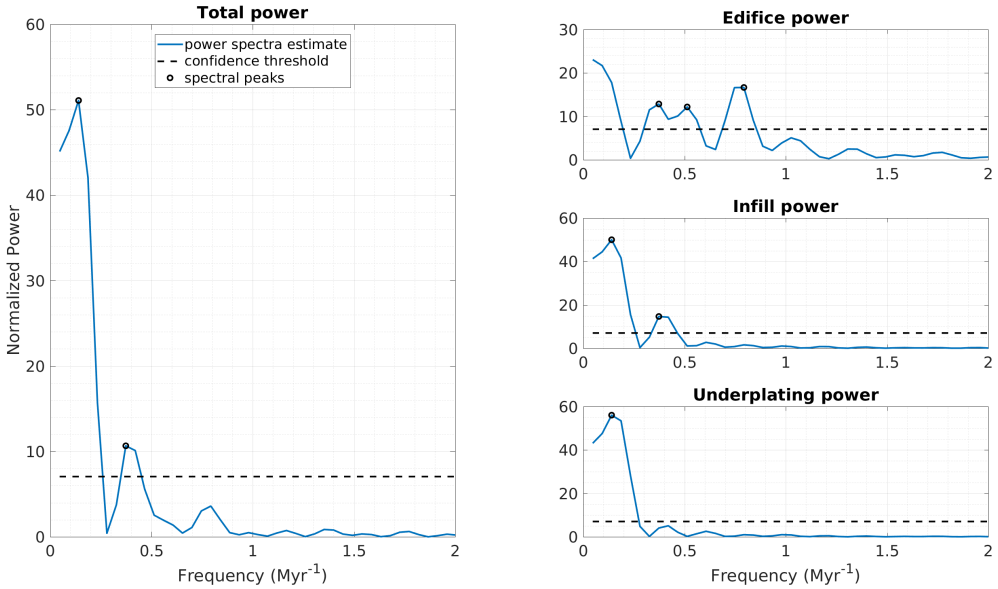

Figure 5.35: Power spectra for the Marquesas hotspot. (Left) Total volume power spectra, with FAP confidence (dashed line) and spectral peaks (circles). (Right) Separated volume component power spectra.

Average melt flux for the Marquesas hotspot track is 13.9 m^3/s. Over the hotspot's short history, melt volumes appear to be increasing. Significant spectral peaks appear in the Marquesas edifice volumetric power spectra at 0.373, 0.513, and 0.793 Myr^{-1}. Infill periodicities share only one peak with the edifice peaks, at 0.373 Myr^{-1}. No significant peaks appear in the Marquesas underplating power spectra. One total melt volume spectral peak is resolved at at 0.373 Myr^{-1}.

5.3.10 Réunion

The Réunion hotspot track is split by the Central Indian Ridge, leaving two distinct tracks along the Indian plate and the African plate. On the Indian plate, the hotspot track strikes south from the 66 Ma Deccan Traps (Duncan and Hargraves, 1990). On the African plate, Réunion hotspot tectonic history is more complicated. The hotspot track location is complicated by interfering continental fragments in the neighboring Seychelles, associated with the breakup of Rodinia (Torsvik et al., 2013). During breakup, the Central

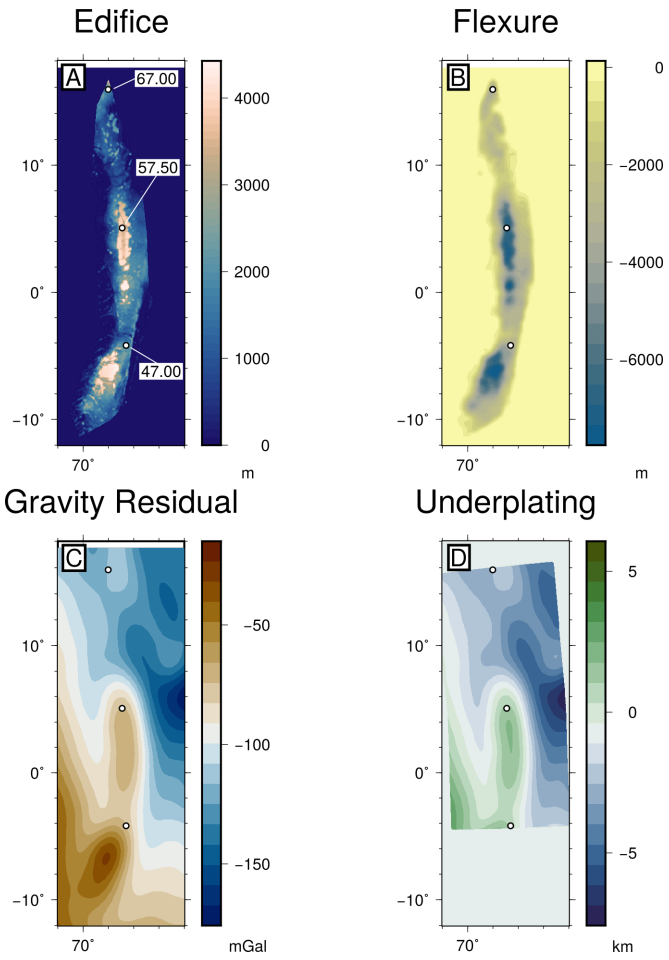

Figure 5.36: Resultant maps for the northern track of the Réunion hotspot. (A) Volcanic edifice and hotspot age samples. (B) Calculated flexure profile. (C) Gravity residual map. (D) Underplating relative thickness map

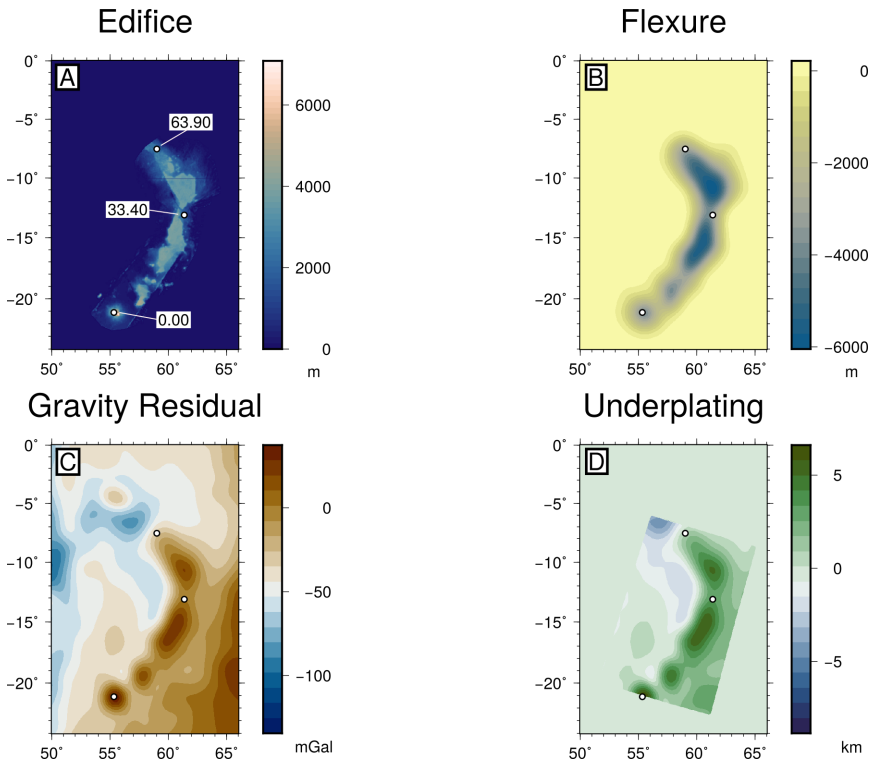

Figure 5.37: Resultant maps for the southern track of the Réunion hotspot. (A) Volcanic edifice and hotspot age samples. (B) Calculated flexure profile. (C) Gravity residual map. (D) Underplating relative thickness map

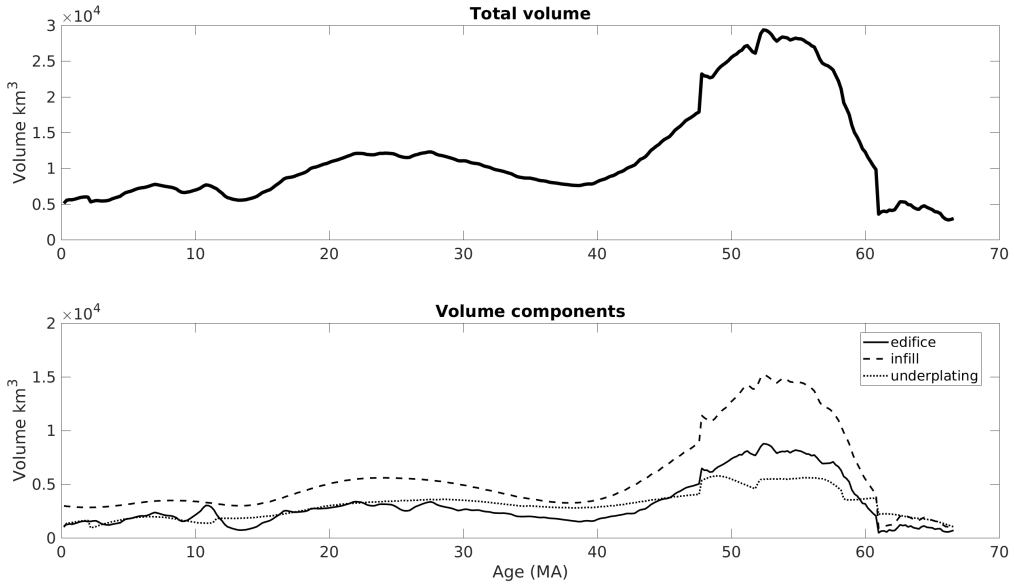

Figure 5.38: Réunion hotspot melt volumes with time. (Top) Total melt volume. (Bottom) Separated volume components

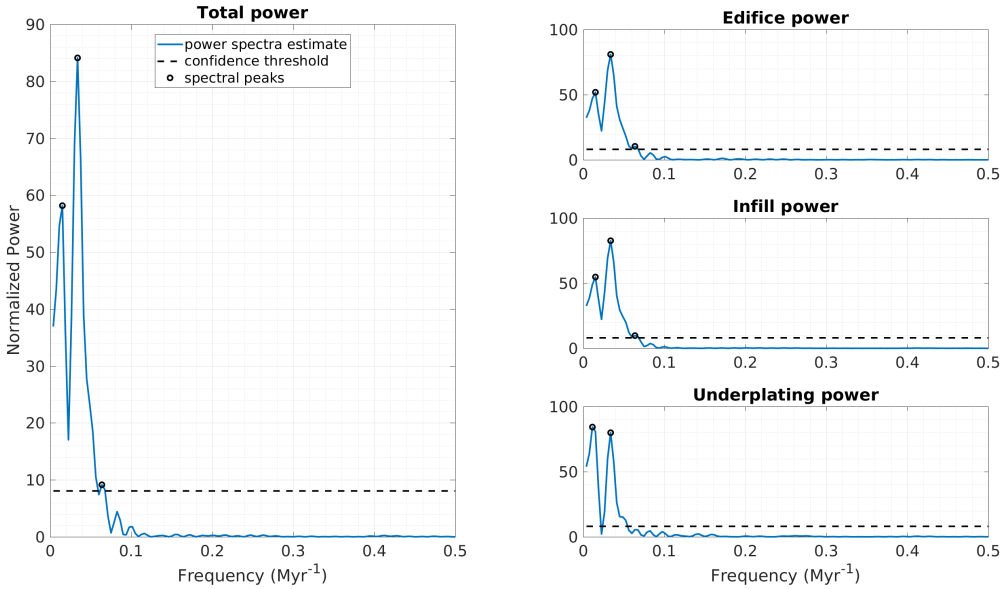

Figure 5.39: Power spectra for the Réunion hotspot. (Left) Total volume power spectra, with FAP confidence (dashed line) and spectral peaks (circles). (Right) Separated volume component power spectra.

Indian Ridge relocated southwest of the plume (80–60 Ma), then northeast of the plume (41 Ma), thus splitting the hotspot track into its current configuration (Torsvik et al., 2013). Here, we consider the India plate hotspot history from the track's intersection with India to Chagos bank (49 Ma, Duncan and Hargraves (1990)) and the African plate history from the oldest Réunion-attributed sampling location along the 64 Ma saddle between the Seychelles block and Saya de Malha Bank (Duncan and Hargraves, 1990) terminating at the recently-active (0.7 Ma) Réunion Island (McDougall, 1971).

Average melt flux for the Réunion hotspot track is 16.0 m^3/s. A large pulse of magmatism is evident at 55 Ma, early in the hotspot's history, at the northern end of the track emplaced on the Indian plate. The Réunion hotspot has spectral peaks in edifice volume at 0.034 and 0.064 Myr^{-1}. Infill volume spectral peaks are identical to edifice volume peaks, while the underplating spectrum has only one peak at 0.034 Myr^{-1}. The total melt volume has spectral peaks at 0.034 and 0.064 Myr^{-1}.

5.3.11 St. Helena

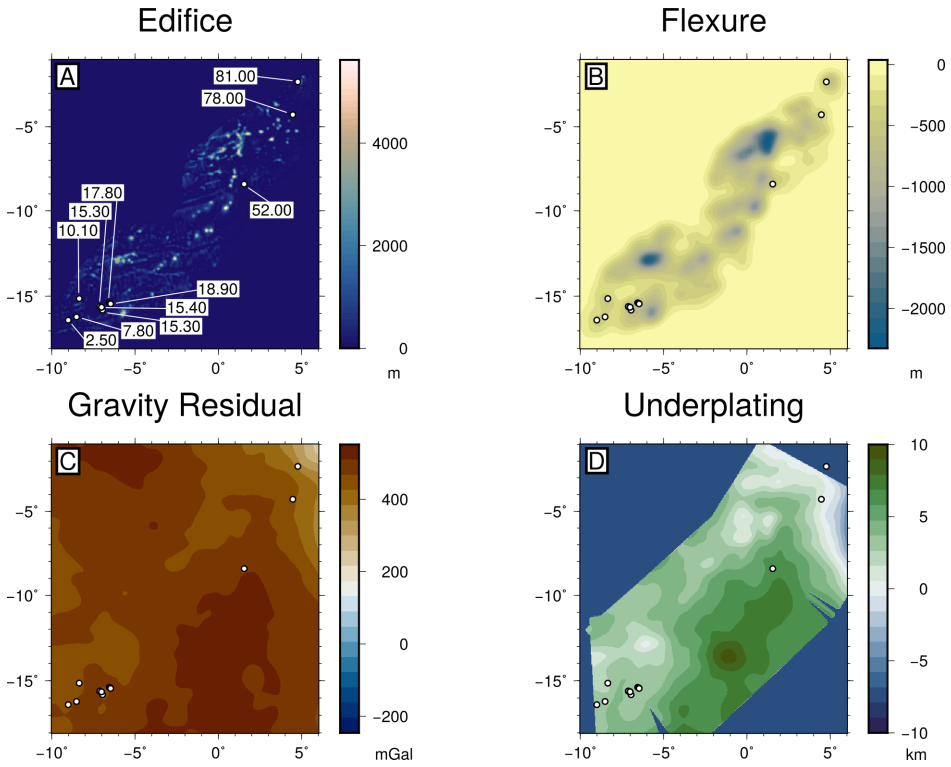

Figure 5.40: Resultant maps for St. Helena hotspot. (A) Volcanic edifice and hotspot age samples. (B) Calculated flexure profile. (C) Gravity residual map. (D) Underplating relative thickness map

The St. Helena hotspot is characterized by a relatively diffuse volcanic expression, striking northeast from a presumed plume located at 16°S 6°W (Montelli et al., 2006). The youngest recovered samples from St. Helena-attributed volcanics are 2.6 Ma (O'Connor et al., 1999; Courtillot et al., 2003). The old end of the hotspot track has material dated at 81 Myr old (O'Connor and Duncan, 2008). The St. Helena volcanic track may be the result of volcanism associated with multiple mantle plumes (O'Connor and Duncan, 2008; O'Connor et al., 1999; Adam et al., 2007). Tomographic images indicate the Ascension plume and the St. Helena plume appear to merge at 1000 km depth, part of a larger complex of plumes that converge at depth, including the Walvis Ridge/Tristan-Gough plume (Montelli et al., 2006). Here we will treat the St. Helena as an isolated hotspot.

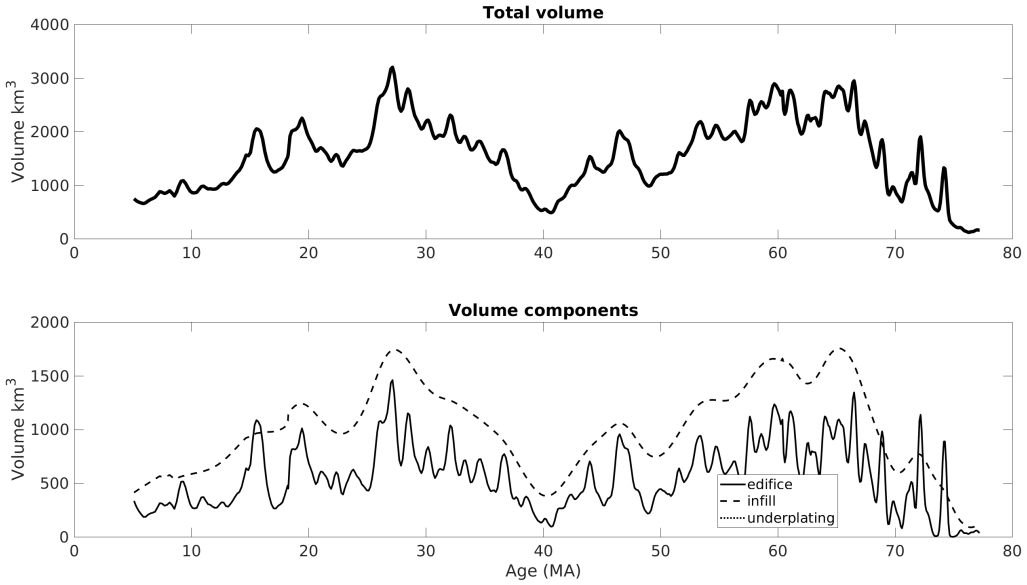

Figure 5.41: St. Helena hotspot melt volumes with time. (Top) Total melt volume. (Bottom) Separated volume components

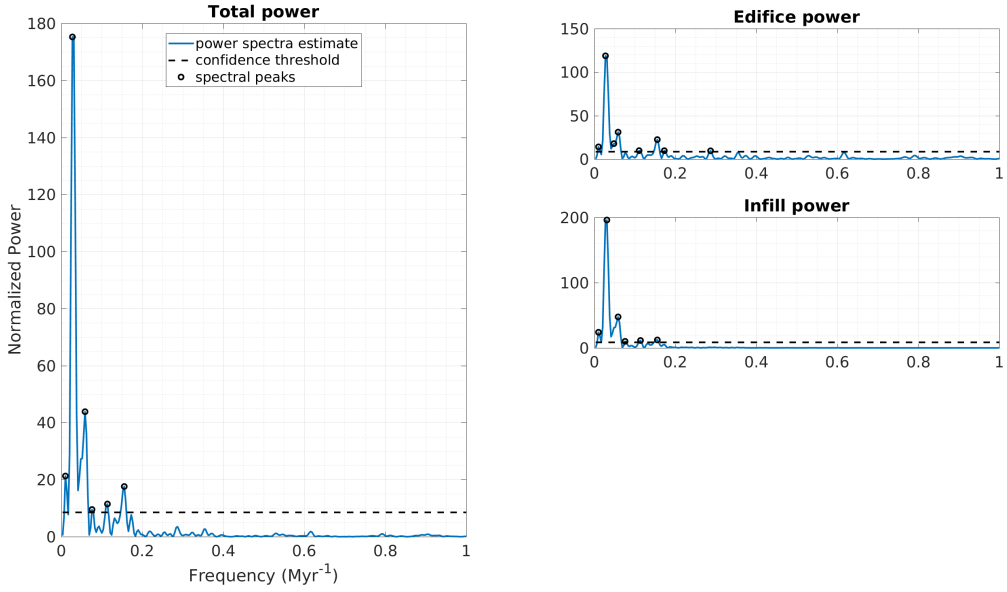

Figure 5.42: Power spectra for the St. Helena hotspot. (Left) Total volume power spectra, with FAP confidence (dashed line) and spectral peaks (circles). (Right) Separated volume component power spectra.

Average melt flux for the St. Helena hotspot track is 1.53 m^3/s. Melt volumes vary over the hotspot's 70 Myr history, with two broad periods of enhanced melt output around 30 Ma and 60 Ma. Significant peaks in the volcanic edifice volumetric power spectra for St. Helena hotspot track appear at 0.031, 0.048, and 0.073 Myr^{-1}, which are shared by the infill volume power spectra. No significant underplating signal was recovered from our analysis. Total volumetric power spectral peaks occur at frequencies of 0.031, 0.048, and 0.073 Myr^{-1}.

5.3.12 Walvis Ridge/Tristan de Cunha/Tristan-Gough

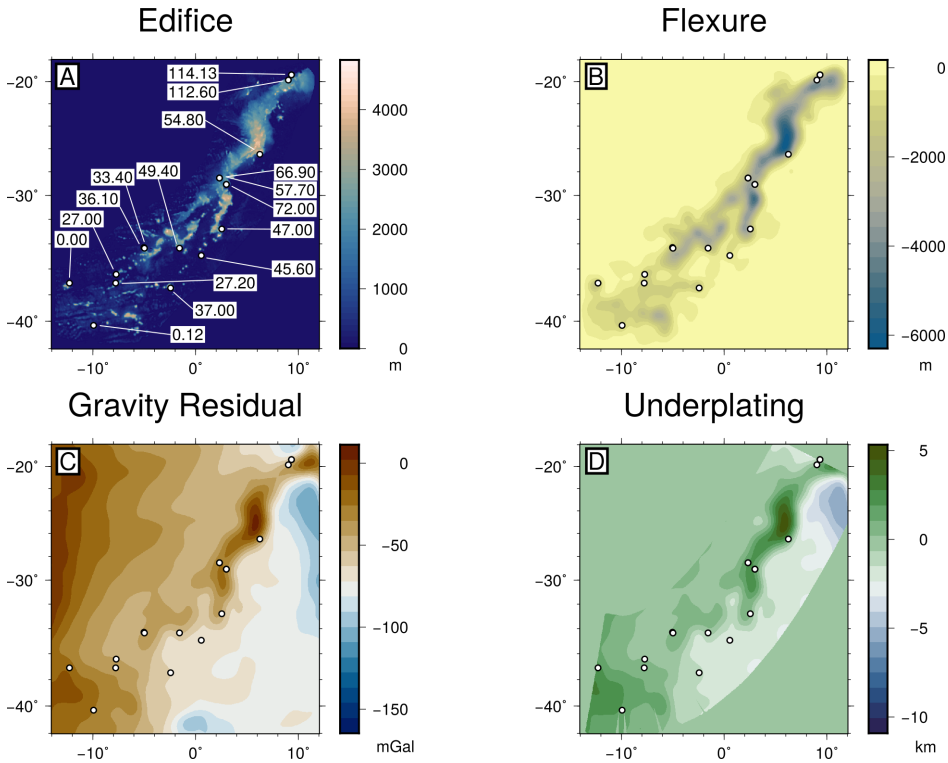

Figure 5.43: Resultant maps for Tristan-Gough hotspot. (A) Volcanic edifice and hotspot age samples. (B) Calculated flexure profile. (C) Gravity residual map. (D) Underplating relative thickness map

The Walvis Ridge (also known as the Tristan de Cunha or Tristan-Gough hotspot track) strikes northeast from a plume location under Tristan de Cunha island at 38°S 14°W (Montelli et al., 2006) with a corresponding section of volcanic material in the Rio

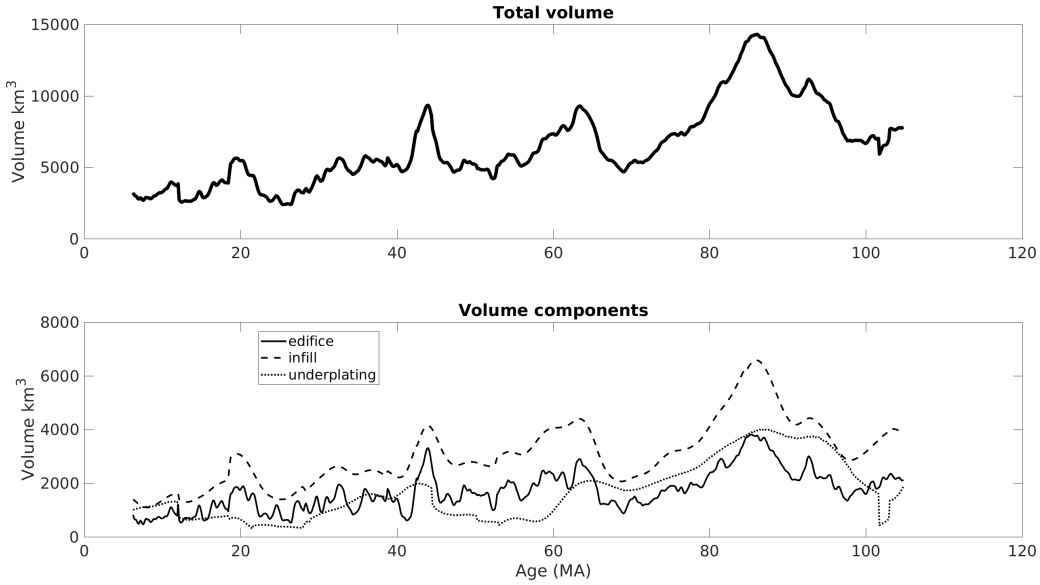

Figure 5.44: Tristan-Gough hotspot melt volumes with time. (Top) Total melt volume. (Bottom) Separated volume components

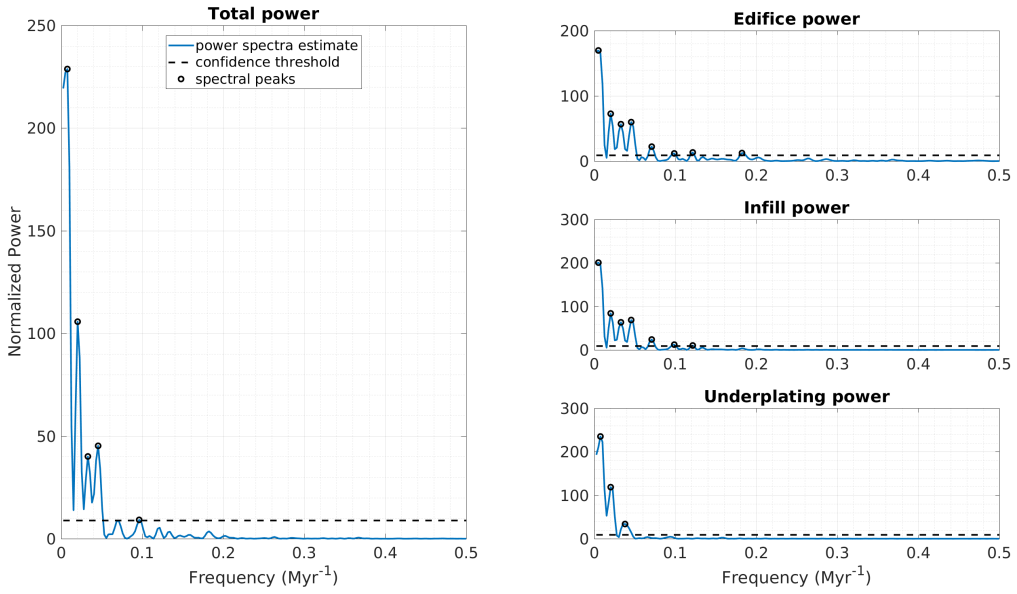

Figure 5.45: Power spectra for the Tristan-Gough hotspot. (Left) Total volume power spectra, with FAP confidence (dashed line) and spectral peaks (circles). (Right) Separated volume component power spectra.

Grande Rise on the west side of the mid-Atlantic ridge, emplaced 70 Ma (O'Connor and Duncan, 2008). Previous work attributes the Etendeka and Paraná flood basalt provinces (127.5-139 Ma) to melting of the plume head associated with the Walvis Ridge system, suggesting the plume emplaced volcanic material on both sides of the ridge from 139 Ma to 70 Ma (O'Connor et al., 1999; Gibson et al., 2005). Here we analyze only the hotspot material on the eastern side of the ridge, as the material on the western side has not been dated at comparable resolution (e.g., Hoernle et al., 2015). Young volcanic material (<20 Ma) east of the mid-Atlantic ridge occurs along separate tracks that strike SW and SSW, respectively. Along the southwest striking track, recent eruptions at Tristan de Cunha Island (Hicks et al., 2012) suggest an underlying plume. However, young eruptive materials are also observed at Gough Island, 400 km away (Maund et al., 1988; Rohde et al., 2013) to the southeast along the south-southwest striking track. The distinct volcanic tracks and apparent simultaneous volcanic activity across 400 km may be due to a widespread plume source or interactions with the nearby mid-Atlantic ridge (Rohde et al., 2013).

Average melt flux for the Tristan-Gough hotspot track is 6.31 m^3/s. Melt volumes generally decrease over the hotspots 90 Myr history. Tristan-Gough edifice and infill volumes share power spectral peaks at frequencies of 0.020, 0.033, 0.046, 0.071, and 0.099 Myr^{-1}. Underplating spectral peaks occur at periods of 0.020 and 0.038 Myr^{-1}. Total volumetric output power spectral peaks are 0.020, 0.033, 0.046, and 0.096 Myr^{-1}.

5.4 Combined Results

The combined average hotspot volume flux for all hotspots analyzed is 6.4 m^3/s, the total average melt flux for all twelve hotspots is 77 m^3/s. Hotspots with no significant underplating signal (Bowie, Cobb, Louisville, and St. Helena) have a total average edifice and infill volume flux of <6 m^3/s, comprising less than 10% of the total average flux. With

the exception of Galápagos, Kerguelen, and Marquesas, all hotspots vary up to 100% of their average volume output during their lifetime (Figure 5.46). Hawaii nearly doubles the average output over 5 Ma. Louisville has steadily decreased from a maximum output around 100% its average at 48 Ma to <50% of its average at 5 Ma.

All hotspots analyzed have periodicity peak(s) that meet the requirements defined above for significant results (Table 5.2). Most significant spectral peaks have periods between 4–12 million years (frequency of 0.0833-0.25 Myr^{-1}). The lowest frequency peak resolved in our analysis is 0.023 Myr^{-1}, in the Kerguelen melt flux power spectrum.

Table 5.3: Hotspot melt fluxes and total volumes

Hotspot	Average flux (m^3/s)	Total volumetric output (km^3)
Bowie[A]	0.31	2.20×10^5
Cobb[A]	0.52	4.81×10^5
Easter	10.2	8.37×10^6
Foundation	4.90	2.80×10^6
Galápagos	11.4	7.32×10^6
Hawaii	3.45	8.81×10^6
Kerguelen	5.14	1.95×10^7
Louisville[A]	0.52	1.09×10^6
Marquesas	13.9	2.34×10^6
Réunion	16.0	3.35×10^7
St. Helena[A]	1.53	3.48×10^6
Tristan-Gough	6.31	1.96×10^7

[A] Hotspots with underplating volumes below detection limits

5.5 Discussion

5.5.1 Comparison with previous hotspot flux estimates

We compare our mean melt fluxes to previous estimates of hotspot melt flux (West et al., 2003; White, 1993a; Van Ark and Lin, 2004; Coffin et al., 2002; Sreejith and Krishna, 2015). Our estimates broadly agree with previous works quantifying melt fluxes at select

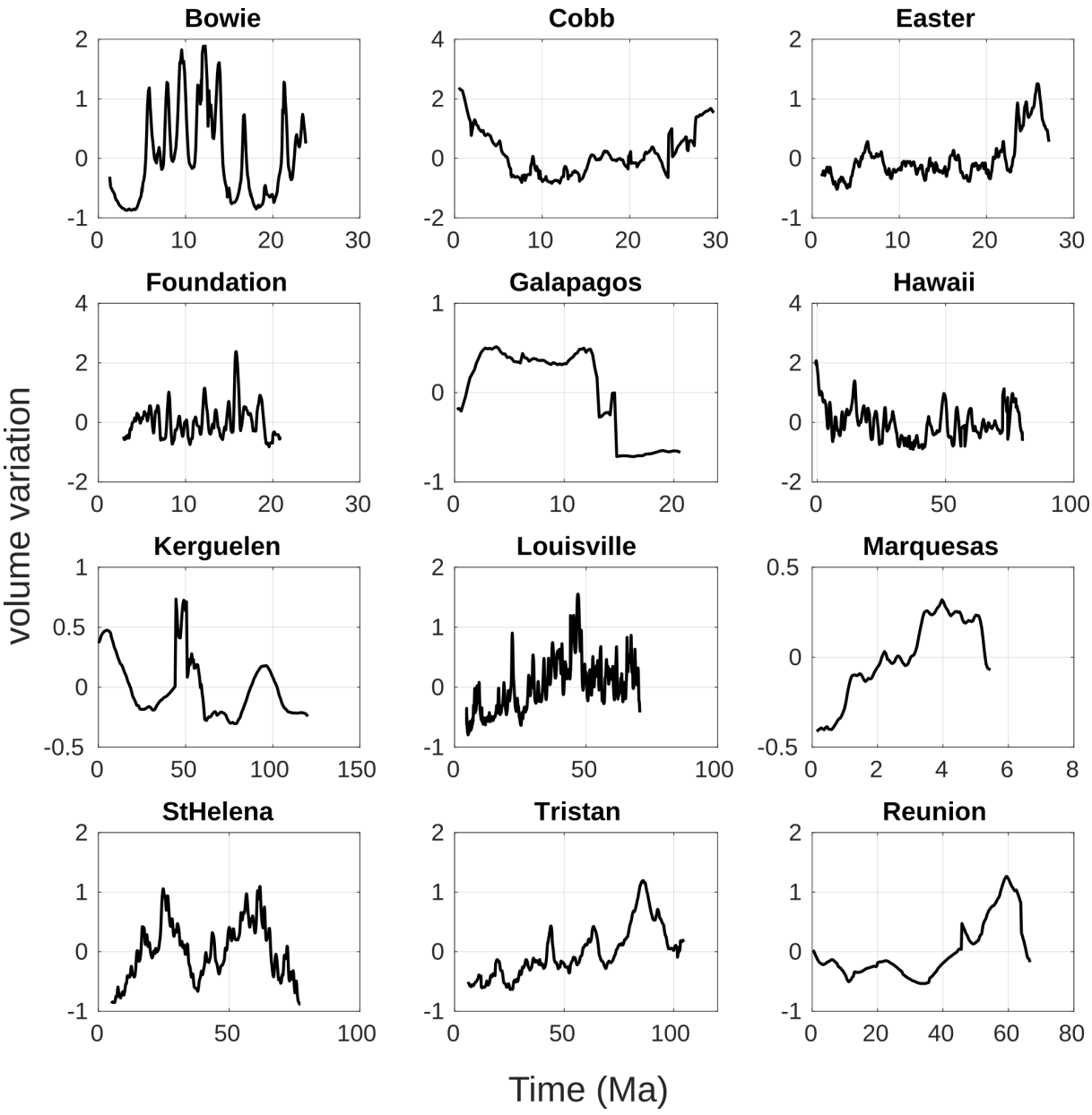

Figure 5.46: Volume variation as a ratio of the along-track average at each hotspot (i.e., 0 corresponds to the average along-track volume, 1 corresponds to a 100% increase in volume relative to the average).

hotspots using various methods (Table 5.3). Some flux estimates are based on current volcanic activity (West et al., 2003), while others evaluate melt production over time (White, 1993a; Van Ark and Lin, 2004; Coffin et al., 2002; Sreejith and Krishna, 2015). We compare our average melt production values to historical ranges of melt production and averages to critically evaluate strengths and shortcomings in our generalized method compared to hotspot-specific studies.

At the Cobb hotspot, West et al. (2003) constrain crustal thicknesses at Axial Seamount with seismic reflection and refraction profiles. They estimate Cobb has a melt flux of 0.3-0.8 m^3/s, compared to our estimate of 0.52 m^3/s. Van Ark and Lin (2004) estimate the Hawaiian hotspot average flux for the length of the hotspot track at 0–8 m^3/s, in agreement with our estimate of 3.5 m^3/s. White (1993a) provides an estimated range of melt production 0.03-0.16 km^3/yr, compared to our value of 0.1 km^3/yr. Coffin et al. (2002) estimate Kerguelen hotspot has a relatively constant flux 0.1 km^3/yr with some deviations during periods of plume-ridge interaction, up to 0.9 km^3/yr. White (1993a) predicts 0.25 km^3/yr of melt production at Kerguelen. Our results show a comparable average melt flux, 0.16 km^3/yr, or 5.1 m^3/s and comparable to estimates of 5-15 m^3/s for the NinetyEast Ridge (Sreejith and Krishna, 2015). At Réunion, White (1993a) estimates current melt production 0.04 km^3/yr, considerably lower than our estimate of 0.5 km^3/yr. The Réunion hotspot has decreased in melt flux from >1 km^3/yr during the Deccan Trap emplacement (66-68 Ma) to much lower present values along a nearly exponential decay curve (White, 1993a). Our estimate is an along-hotspot average, which likely reflects the decreasing melt production highlighted by White (1993a).

Comparing our power spectral results to previous hotspot volume flux power spectra (Van Ark and Lin, 2004; Sreejith and Krishna, 2015) yields mixed agreement at different hotspots. We compare our spectral peak results and differences in methodologies used in

other works. For ease of comparison (and interpretation), we will report spectral peaks here in mega-annum periods (1/f).

At Kerguelen, our analysis is complicated by the separation of portions of the hotspot track due to interactions with the Southwest Indian Ridge. Sreejith and Krishna (2015) resolve power spectral peaks at 16.5 and 5.5 Myr. Our results indicate spectral peaks at 43.7 and 30 Myr. Given the significant differences in methodology and the complex history of the Kerguelen hotspot, it is difficult to validate these results against each other. Disagreement in spectral peaks may be a result of our reconstruction methodology, which does not account for detailed ridge jump reconstructions like Sreejith and Krishna (2015). In our case, we did not want to introduce too many discontinuities in the volume calculation by dividing the NinetyEast Ridge into several smaller blocks; discrete jumps in volumes resulting from combining many separate analyses impart some noise to the spectral signal. We attempt to minimize these discontinuities by analyzing the NinetyEast Ridge as a continuous track, which may have resulted in a loss of the spectral peaks that Sreejith and Krishna (2015) recovered. Alternatively, Sreejith and Krishna (2015) detailed reconstruction may have obscured the low frequency spectral peaks that our analysis recovered.

At the Hawaiian hotspot, our melt volume fluxes differ slightly, but our spectral analysis results generally agree with Van Ark and Lin (2004). Their power spectrum for the Hawaiian hotspot reports spectral peaks at 30.8, 20.6, 15.4, 9.5, 6.2 and 1.5-3.6 Myr periods. Our results indicate similar peaks at 22.9, 14.5, 9.4, and seven peaks below 3.6 Myr. We did not resolve a significant spectral peak comparable to their 30.8 Myr spectral peak, but we note that 30.8 Myr may be a harmonic multiple of the 15.4 Myr peak, which is similar to our 14.5 Myr peak. We do not report peaks below 2.06 Myr, as these spectral peaks fall below our maximum-adjacent volcano spacing criterion. Our results broadly agree with Van Ark and Lin (2004).

5.5.2 Plume pulsing

All plumes analyzed exhibit periodic variations in melt volume production, but the mechanisms responsible for these pulsations are unclear. Previous studies (Morgan et al., 1995) have suggested that major lithosphere discontinuities, such as fracture zones, may modify plume flow and impart flux variations at frequencies lower than volcanic spacing. However, at all the hotspots we analyzed, the spectral peaks in our melt volumes suggest that fracture zones are not the only cause for pulsing plumes. Though the semi-regular spacing of the Pacific FZs across the Hawaiian hotspot track might impart a periodic signal to hotspot melt volumes, as suggested by Morgan et al. (1995), the Hawaiian melt volume power spectra has peaks across a range of frequencies from 0.464 to 0.019 Myr^{-1}, too many to only be consistent with the spacing of FZs (crossing at 2-5 Ma, 20 Ma, and 46 Ma; frequencies of 0.04-0.06 Myr^{-1}). At the Louisville hotspot, melt productivity is geochemically linked to lithospheric thickness and the presence of FZs crossing the hotspot track (Wishbone Scarp, Beier et al. (2011)). These interfering features cross the hotspot track in two locations corresponding to 50 Ma and 40 Ma. Our results show a period of higher melt volume from 48-44 Ma, but the Louisville volume power spectra does not have a spectral peak at 0.1 Myr^{-1}, which would correspond to the timing between the hotspot crossing the two legs of Wishbone Scarp (Beier et al., 2011). Fracture zones likely impart changes to melt productivity along hotspot tracks (Morgan et al., 1995; Beier et al., 2011), but they are not doing so in a regular or periodic manner.

Melt extraction and volcanic processes also may produce periodic variations in hotspot melt production, but individual volcanoes are only active at hotspots for a few million years (e.g., 3 Ma in the Galápagos, Christie et al. (1992) and White (1993b) and 6 Ma in Hawaii, Cousens and Clague (2014)). Our power spectra analysis yields variability in hotspot melt production variation at periods longer than 10 Myr, longer than individual

volcano lifetimes. Our analysis does not discount or exclude lithosphere- and volcano-scale processes as causes for temporal variations in hotspot melt production, but the range of spectral peaks we present includes much lower frequencies than these processes predict. We attribute the lower frequency variations to pulsations in the plume conduit or similar dynamic variations in the plume source.

Other works suggest that in-phase co-pulsations at different hotspots indicate a dynamic connection or similar cause for variations in melt flux (Mjelde and Faleide, 2009). In our spectra results, some hotspots have melt flux pulsations at the same frequency ($\pm$ 0.01 Myr$-$1, Table 5.4). These co-pulsing groups are each found in distinct ocean basins but not all hotspots in one basin are part of the same group. The Pacific Ocean has two separate groups, for example, but none of the co-pulsing groups span the Pacific and another ocean basin. The Easter-Salas, Hawaiian, and Louisville hotspots all share a spectral peak at 0.201 Myr^{-1}. The Galápagos, Easter-Salas, Hawaii, and Foundation hotspots also share a spectral peak around 0.106–0.115 Myr^{-1}. In the Atlantic, the Tristan-Gough and St. Helena hotspots share two spectral peaks, at 0.031–0.033 and 0.046–0.048 Myr^{-1}. Interestingly, the neighboring Bowie and Cobb hotspot tracks do not share any spectral peaks. Co-pulsations of hotspots has been attributed to periodic release of heat from the Earth's core (Mjelde and Faleide, 2009), which would provide a plausible explanation for co-pulsation, but not the stark division of co-pulsing groups into separate ocean basins. Mjelde and Faleide (2009) link pulsations between Iceland and Hawaii, across two ocean basins, which disagrees with our observation of basin groupings.

The hypothesis that large, low shear velocity provinces (LLSVPs) link groups of hotspots together (e.g., Burke et al., 2008; Huang et al., 2011) might provide a better explanation. Anomalously low shear wave velocities occur in portions of the mantle just above the core mantle boundary in 100s of kms-thick regions known as LLSVPs, evidenced by many tomographic images and models (e.g., Becker and Boschi, 2003).

Table 5.4: Co-pulsing hotspots

Hotspot group	Hotspots	Co-pulsation frequencies (Myr^{-1})
Pacific 1	Easter-Salas Hawaii Louisville	0.201
Pacific 2	Easter-Salas Foundation Galápagos Hawaii	0.106–0.115
Atlantic (two frequencies)	St. Helena Tristan-Gough	0.031–0.033 / 0.046–0.048

Hotspots are often located on the edge of these LLSVPs, suggesting that they nucleate from the LLSVP boundaries (Burke et al., 2008). The groups of co-pulsing hotspots Galápagos, Easter-Salas, Hawaii, and Foundation may be associated with the Pacific LLSVP, as may be the Easter-Salas, Hawaii, and Louisville co-pulsation group. Meanwhile, St. Helena and Tristan may be associated with the African LLSVP. If the causal link between co-pulsing hotspots is their connection to the same LLSVP, then it is possible that co-pulsations represent a periodic behavior of the LLSVP; our results do not imply any particular mechanism. Furthermore, while the LLSVP-plume hypothesis would adequately link some of these groups of co-pulsing hotspots together, it does not explain why there are two co-pulsing groups in the Pacific that share some members, though all of the hotspots in both groups should be connected to the same LLSVP (Burke et al., 2008).

5.5.3 Models of pulsing plumes

Thermal plumes have long been examined in laboratory and numerical models. Early models simulated simple thermal buoyancy perturbations (e.g., Detrick and Crough, 1978), while others simulated fully dynamical models, accounting for flow and rate of melt production (e.g., Parmentier et al., 1975). Modern plume models incorporate significantly more complex rheologic and dynamic conditions, including interaction with

overlying lithosphere. Some of these models investigate why plumes may pulse and how melt production may vary as a result of fluctuations in the volume flux of rising material.

Laboratory experiments and numerical simulations on tilted plume conduits suggest that they should remain stable in the upper mantle (Kerr et al., 2008; Mériaux et al., 2010). However, plate-motion induced destabilizations of rising plumes exist in earlier analog models (Whitehead, 1982; Griffiths and Richards, 1989; Griffiths and Campbell, 1990; Richards and Griffiths, 1988; Richards and Griffiths, 1989). Alternatively, models that incorporate plate motion and account for endo- and exothermic mineral phase changes do present periodic flux variations consistent with our observations. For example, numerical models of plumes passing through rheological boundaries suggest regular variation in plume upwelling rates but results between 2-D and 3-D models were inconclusive (Keken et al., 1992; Keken and Gable, 1995). More recently, numerical models including temperature, pressure, and phase-based viscosities indicate that transition zone-derived plume behaviors may produce steady plumes, pulsing plumes, and superplumes, which have semi-periodic and sometimes chaotic pulses (Brunet and Yuen, 2000). Neuharth and Mittelstaedt (2017) found conduit destabilization pulses occurring in modeled plumes as a result of both plate-motion lateral shearing and variations in the Clapeyron slope of phase changes at depth. Conduit stability pulses occur in these models over a range of 4.1–37.9 Myr periods, consistent with our observations. Additionally, these models indicate that pulsations are not well-established until at several 10s of Myr after the initial thermal plume reaches the upper mantle, which may provide an explanation for the apparent lack of significant periodicities in the Marquesas hotspot track. These models do not however provide a plasuible explanation for the distribution of co-pulsing groups, as some groups (the Hawaii, Galápagos, Easter-Salas, and Foundation group, for example) are located across different tectonic plates and thus subject to different plate motion rates.

Assuming pulsations in melt supply are strictly a result of pulsations in the volume flux of plume material to the surface, our results are most consistent with numerical results from Neuharth and Mittelstaedt (2017). Unfortunately, Brunet and Yuen (2000) do not report the periodicity of their plume models, and we cannot evaluate if their models would be consistent with our results. Other models of destabilization (Whitehead, 1982; Griffiths and Richards, 1989; Griffiths and Campbell, 1990; Richards and Griffiths, 1988; Richards and Griffiths, 1989) also do not report periodic behavior. Thus, the combination of rheologic phase change and plate motion effects modeled by Neuharth and Mittelstaedt (2017) seems the most likely cause of pulsations in melt supply observed at the twelve hotspots presented. If this is the case, then the link between co-pulsing groups near similar LLSVPs may simply be geographic, as most of the co-pulsing groups share the same or very similar plate motion velocities.

5.6 Conclusions

All plumes observed appear to have pulsations over regular intervals during their lifetimes. Hotspot melt production pulsations yield variations of 10-200% of average melt production, by volume. The timing of these pulses is consistent with both plate motion destabilization and deep phase transition influences, as suggested by numerical models, though we are unable to discern specific causes for individual pulsations at specific hotspots. The number of spectral peaks in hotspot volumes varies from one to more than ten in some cases. We conclude that the varied characteristics of hotspot pulsations that cannot be explained by lithosphere interaction alone suggests that pulsations are an inherent feature of mantle plumes, likely a result of their dynamic ascent through the Earth.

References

Abercrombie, R.E. and G. Ekström (2001). "Earthquake slip on oceanic transform faults". In: *Nature* 410.6824, pp. 74–7. DOI: 10.1038/35065064.

Adam, Claudia, Valerie Vidal, and Javier Escartín (2007). "80-Myr history of buoyancy and volcanic fluxes along the trails of the Walvis and St. Helena hotspots (South Atlantic)". In: *Earth and Planetary Science Letters* 261.3-4, pp. 432–442. DOI: 10.1016/j.epsl.2007.07.005.

Atwater, T M et al. (1993). "Fracture zone traces across the North Pacific Cretaceous quiet zone and their tectonic implications". In: *The Mesozoic Pacific: Geology, tectonics, and volcanism* 77, pp. 137–154.

Atwater, Tanya and Ken C. Macdonald (1977). "Are spreading centers perpendicular to their transform faults?" In: *Nature* 270.5639, pp. 715–719. DOI: 10.1038/270715a0.

Bach, Wolfgang et al. (2004). "Seawater-peridotite interactions: First insights from ODP Leg 209, MAR 15°N". In: *Geochemistry, Geophysics, Geosystems* 5.9. DOI: 10.1029/2004GC000744.

Balay, Satish et al. (2011). "Efficient Management of Parallelism in Object-Oriented Numerical Software Libraries". In: *Modern Software Tools for Scientific Computing*, pp. 163–202. DOI: 10.1007/978-1-4612-1986-6_8.

Ballmer, Maxim D. et al. (2011). "Spatial and temporal variability in Hawaiian hotspot volcanism induced by small-scale convection". In: *Nature Geoscience* 4.7, pp. 457–460. DOI: 10.1038/ngeo1187.

Barckhausen, Udo et al. (2008). "Birth of an intraoceanic spreading center". In: *Geology* 36.10, pp. 767–770. DOI: 10.1130/G25056A.1.

Becker, Thorsten W. and Lapo Boschi (2003). "A comparison of tomographic and geodynamic mantle models". In: *Geochemistry, Geophysics, Geosystems* 3.1, n/a–n/a. DOI: 10.1029/2001gc000168.

Beeler, N M et al. (2000). "Pore fluid pressure, apparent friction, and Coulomb failure". In: *Journal of Geophysical Research* 105.B11. DOI: 10.1029/2000JB900119.

Behn, Mark D. (2002). "Evidence for weak oceanic tr m faults". In: *Geophysical Research Letters* 29.24, p. 2207. DOI: 10.1029/2002GL015612.

Behn, Mark D. and Garrett Ito (2008). "Magmatic and tectonic extension at mid-ocean ridges: 1. Controls on fault characteristics". In: *Geochemistry, Geophysics, Geosystems* 9.8. DOI: 10.1029/2008GC001965.

Behn, Mark D. and Jian Lin (2000). "Segmentation in gravity and magnetic anomalies along the U.S. East Coast passive margin: Implications for incipient structure of the oceanic lithosphere". In: *Journal of Geophysical Research: Solid Earth* 105.B11, pp. 25769–25790. DOI: 10.1029/2000jb900292.

Behn, Mark D., Margaret S. Boettcher, and Greg Hirth (2007). "Thermal structure of oceanic transform faults". In: *Geology* 35.4, p. 307. DOI: 10.1130/G23112A.1.

Beier, Christoph et al. (2011). "Lithospheric control on geochemical composition along the Louisville Seamount Chain". In: *Geochemistry, Geophysics, Geosystems* 12.9, n/a–n/a. DOI: 10.1029/2011GC003690.

Bideau, Daniel et al. (1991). "Metamorphism of Deep-Seated Rocks From The Garrett Ultrafast Transform (East Pacific Rise Near 13°25 ' S)". In: *Journal of Geophysical Research* 96.B6, pp. 10079–10099. DOI: 10.1029/91JB00243.

Boettcher, M. S. and T. H. Jordan (2004). "Earthquake scaling relations for mid-ocean ridge transform faults". In: *Journal of Geophysical Research* 109.B12, B12302. DOI: 10.1029/2004JB003110.

Bonatti, E et al. (1994). "Transform migration and vertical tectonics at the Romanche fracture zone, equatorial Atlantic". In: *Journal of Geophysical Research: Solid Earth* 99.B11, pp. 21779–21802. DOI: 10.1029/94JB01178.

Bonatti, Enrico and Jose Honnorez (1976). "Sections of the Earth's crust in the Equatorial Atlantic". In: *Journal of Geophysical Research* 81.23, pp. 4104–4116. DOI: 10.1029/JB081i023p04104.

Bonneville, A and M McNutt (1992). "Shear strength of the great Pacific fracture zones". In: *Geophysical Research Letters* 19.20, pp. 2023–2026. DOI: 10.1029/92GL02120.

Bonvalot, S et al. (2012). "World gravity map. Commission for the Geological Map of the World. Eds". In:

Braunmiller, Jochen and John Nábělek (2008). "Segmentation of the Blanco Transform Fault Zone from earthquake analysis: Complex tectonics of an oceanic transform fault". In: *Journal of Geophysical Research* 113.B7, pp. 1–23. DOI: 10.1029/2007JB005213.

Brunet, David and David A. Yuen (2000). "Mantle plumes pinched in the transition zone". In: *Earth and Planetary Science Letters* 178.1-2, pp. 13–27. DOI: 10.1016/S0012-821X(00)00063-7.

Bryan, WB (1981). "Compositional variation in normal MORB from 22°â25° N: MidâAtlantic Ridge and Kane Fracture Zone". In: *Journal of Geophysical ...* 86.

Buck, W. R. (2006). "The role of magma in the development of the Afro-Arabian Rift System". In: *Geological Society, London, Special Publications* 259.1, pp. 43–54. DOI: 10.1144/GSL.SP.2006.259.01.05.

Burke, Kevin et al. (2008). "Plume Generation Zones at the margins of Large Low Shear Velocity Provinces on the core-mantle boundary". In: *Earth and Planetary Science Letters* 265.1-2, pp. 49–60. DOI: 10.1016/j.epsl.2007.09.042.

Cande, Steven C et al. (1995). "Geophysics of the Pitman Fracture Zone and Pacific-Antartic Plate Motions During the Cenozoic". In: *Science* 270.10 November, pp. 947 –953.

Cannat, Mathilde and Monique Seyler (1995). "Transform tectonics, metamorphic plagioclase and amphibolitization in ultramafic rocks of the Vema transform fault (Atlantic Ocean)". In: *Earth and Planetary Science Letters* 133, pp. 283–298.

Choi, Eun-seo, Luc Lavier, and Michael Gurnis (2008). "Thermomechanics of mid-ocean ridge segmentation". In: *Physics of the Earth and Planetary Interiors* 171.1-4, pp. 374–386. DOI: 10.1016/j.pepi.2008.08.010.

Christeson, Gail and Marcia K Mcnutt (1992). "Geophysical constraints on the shear stress along the Marquesas Fracture Zone". In: *Journal of Geophysical Research* 97, pp. 4425–4437. DOI: 10.1029.

Christie, D. M. et al. (1992). "Drowned islands downstream from the Galapagos hotspot imply extended speciation times". In: *Nature* 355.6357, pp. 246–248. DOI: 10.1038/355246a0.

Clouard, Val (2001). "How many Pacific hotspots are fed by deep-mantle plumes?" In: *Geology* 387.8, p. 365. DOI: 10.1130/0091-7613(2001)029<0695:HMPHAF>2.0.CO;2.

Coffin, Millard F et al. (2002). "Kerguelen Hotspot Magma Output since 130 Ma". In: *JOURNAL OF PETROLOGY AUSTRALIA RECEIVED JUNE* 43.14, pp. 1121–1139.

Collette, Bastiaan J. (1974). "Thermal contraction joints in a spreading seafloor as origin of fracture zones". In: *Nature* 251.5473, pp. 299–300. DOI: 10.1038/251299a0.

Condie, KC (2001). *Mantle plumes and their record in Earth history.*

Courtillot, Vincent et al. (2003). "Three distinct types of hotspots in the Earth{\textquoteright}s mantle". In: *Earth and Planetary Science Letters* 205, pp. 295–308.

Cousens, Brian L. and David A. Clague (2014). "Shield to rejuvenated stage volcanism on Kauai and Niihau, Hawaiian Islands". In: *Journal of Petrology* 56.8, pp. 1547–1584. DOI: 10.1093/petrology/egv045.

Crameri, F. et al. (2012). "A comparison of numerical surface topography calculations in geodynamic modelling: An evaluation of the 'sticky air' method". In: *Geophysical Journal International* 189.1, pp. 38–54. DOI: 10.1111/j.1365-246X.2012.05388.x.

Croon, Marcel B., Steven C. Cande, and Joann M. Stock (2008). "Revised Pacific-Antarctic plate motions and geophysics of the Menard Fracture Zone". In: *Geochemistry, Geophysics, Geosystems* 9.7, pp. 1–20. DOI: 10.1029/2008GC002019.

Dalrymple, G. Brent et al. (1987). "40 Ar/ 39 AR AGE, Petrology, and Tectonic Significance of Some Seamounts in the Gulf of Alaska". In: American Geophysical Union (AGU), pp. 297–315. DOI: 10.1029/gm043p0297.

Dauteuil, O., O. Bourgeois, and T. Mauduit (2002). "Lithosphere strength controls oceanic transform zone structure: insights from analogue models". In: *Geophysical Journal International* 150.3, pp. 706–714. DOI: 10.1046/j.1365-246X.2002.01736.x.

Demets, Charles and Stephen Traylen (2000). "Motion of the Rivera plate since 10 Ma relative to the Pacific and North American plates and the mantle". In: *Tectonophysics* 318.1-4, pp. 119–159. DOI: 10.1016/S0040-1951(99)00309-1.

DeMets, Charles, Richard G. Gordon, and Donald F. Argus (2010). "Geologically current plate motions". In: *Geophysical Journal International* 181.1, pp. 1–80. DOI: 10.1111/j.1365-246X.2009.04491.x.

Desonie, D. L. and R. A. Duncan (1990). "The Cobb-Eickelberg seamount chain: Hotspot volcanism with mid-ocean ridge basalt affinity". In: *Journal of Geophysical Research* 95.12, 697â12.

Detrick, R. S., R. S. White, and G. M. Purdy (1993). *Crustal structure of North Atlantic Fracture Zones*. DOI: 10.1029/93RG01952.

Detrick, R. S. et al. (2002). "Correlated geophysical, geochemical, and volcanological manifestations of plume-ridge interaction along the Galápagos Spreading Center". In: *Geochemistry Geophysics Geosystems* 3.10, pp. 1–14. DOI: 10.1029/2002GC000350.

Detrick, Robert S. and S. Thomas Crough (1978). "Island subsidence, hot spots, and lithospheric thinning". In: *Journal of Geophysical Research* 83.B3, p. 1236. DOI: 10.1029/jb083ib03p01236.

Detrick, RS and MH Cormier (1982). "Seismic constraints on the crustal structure within the Vema Fracture Zone". In: *Journal of Geophysical Research* 87.

Dick, Henry J. B. (1989). "Abyssal peridotites, very slow spreading ridges and ocean ridge magmatism". In: *Magmatism in the Ocean Basins* 42.September, pp. 71–105. DOI: 10.1144/GSL.SP.1989.042.01.06.

Dick, Henry J B, Jian Lin, and Hans Schouten (2003). "An ultraslow-spreading class of ocean ridge." In: *Nature* 426.6965, pp. 405–12. DOI: 10.1038/nature02128.

D'Orazio, Massimo, Chiara Boschi, and Daniele Brunelli (2004). "Talc-rich hydrothermal rocks from the St. Paul and Conrad fracture zones in the Atlantic Ocean". In: *European Journal of Mineralogy* 16.1, pp. 73–83. DOI: 10.1127/0935-1221/2004/0016-0073.

Duncan, Robert a and Robert B Hargraves (1990). "40 Ar / 39 Ar Geochronology of basement rocks from the Mascarene Plateau, elements of the Réunion hotspot track The Mascarene Islands : Reunion , Mauritius , and Rodrigues". In: *Proceedings of the Ocean Drilling Program* 115, pp. 43–51.

Ekman, Martin and Jaakko Mäkinen (1996). "Recent postglacial rebound, gravity change and mantle flow in Fennoscandia". In: *Geophysical Journal International* 126.1, pp. 229–234. DOI: 10.1111/j.1365-246X.1996.tb05281.x.

Escartín, J., G. Hirth, and B. Evans (1997). "Nondilatant brittle deformation of serpentinites: Implications for Mohr-Coulomb theory and the strength of faults". In:

Journal of Geophysical Research: Solid Earth 102.B2, pp. 2897–2913. DOI: 10.1029/96jb02792.

Escartín, J. et al. (1999). "Quantifying tectonic strain and magmatic accretion at a slow spreading ridge segment, Mid-Atlantic Ridge, 29°N". In: *Journal of Geophysical Research* 104.B5, p. 10421. DOI: 10.1029/1998JB900097.

Escartín, J., G. Hirth, and B. Evans (2001a). "Strength of slightly serpentinized peridotites: Implications for the tectonics of oceanic lithosphere". In: *Geology* 29.11, pp. 1023–1026. DOI: 10.1130/0091-7613(2001)029<1023:SOSSPI>2.0.CO.

Escartín, Javier et al. (2001b). "Crustal thickness of V-shaped ridges south of the Azores: Interaction of the Mid-Atlantic Ridge (36°-39°N) and the Azores hot spot". In: *Journal of Geophysical Research: Solid Earth* 106.B10, pp. 21719–21735. DOI: 10.1029/2001jb000224.

Fontignie, D. and J. G. Schilling (1991). "87Sr86Sr and REE variations along the Easter Microplate boundaries (south Pacific): Application of multivariate statistical analyses to ridge segmentation". In: *Chemical Geology* 89.3-4, pp. 209–241. DOI: 10.1016/0009-2541(91)90018-M.

Fornari, DJ, DG Gallo, and MH Edwards (1989). "Structure and topography of the Siqueiros transform fault system: Evidence for the development of intra-transform spreading centers". In: *Marine Geophysical Researches*.

Fowler, C. M. R. (2005). *The solid earth : an introduction to global geophysics*. Cambridge University Press, p. 685.

Fox, Paul. J. and David. G. Gallo (1984). "A tectonic model for ridge-transform-ridge plate boundaries: implications for the structue of oceanic lithosphere". In: *Tectonophysics* 104, pp. 205–242.

Freund, Raphael and Anthony M. Merzer (1976). "Anisotropic origin of transform faults". In: *Science* 192.4235, pp. 137–138. DOI: 10.1126/science.192.4235.137.

Frey, Frederick A. et al. (1996). "Petrogenesis of the Bunbury Basalt, Western Australia: interaction between the Kerguelen plume and Gondwana lithosphere?" In: *Earth and Planetary Science Letters* 144.1-2, pp. 163–183. DOI: 10.1016/0012-821x(96)00150-1.

Geist, Dennis et al. (2008). "Construction of the Galápagos platform by large submarine volcanic terraces". In: *Geochemistry, Geophysics, Geosystems* 9.3, n/a–n/a. DOI: 10.1029/2007GC001795.

Geli, L. (1997). "Evolution of the Pacific-Antarctic Ridge South of the Udintsev Fracture Zone". In: *Science* 278.5341, pp. 1281–1284. DOI: 10.1126/science.278.5341.1281.

Gerya, T. V. (2013). "Initiation of transform faults at rifted continental margins: 3D petrological-thermomechanical modeling and comparison to the Woodlark Basin". In: *Petrology* 21.6, pp. 550–560. DOI: 10.1134/S0869591113060039.

Gerya, Taras (2009). *Introduction to Numerical Geodynamic Modelling*. Cambridge: Cambridge University Press. DOI: 10.1017/CBO9780511809101.

Gerya, Taras (2010a). "Dynamical instability produces transform faults at mid-ocean ridges". In: *Science* 329.5995, pp. 1047–1050. DOI: 10.1126/science.1191349.

Gerya, Taras (2010b). "Dynamical instability produces transform faults at mid-ocean ridges." In: *Science (New York, N.Y.)* 329.5995, pp. 1047–50. DOI: 10.1126/science.1191349.

Gibson, S.A. et al. (2005). "Melt-generation processes associated with the Tristan mantle plume: Constraints on the origin of EM-1". In: *Earth and Planetary Science Letters* 237.3-4, pp. 744–767. DOI: 10.1016/J.EPSL.2005.06.015.

Gómez-Ortiz, David and Bhrigu N.P. Agarwal (2005). "3DINVER.M: A MATLAB program to invert the gravity anomaly over a 3D horizontal density interface by Parker-Oldenburg's algorithm". In: *Computers and Geosciences* 31.4, pp. 513–520. DOI: 10.1016/j.cageo.2004.11.004.

Gregg, P. M. et al. (2009). "Melt generation, crystallization, and extraction beneath segmented oceanic transform faults". In: *Journal of Geophysical Research* 114.B11, B11102. DOI: 10.1029/2008JB006100.

Gregg, Patricia M., Jian Lin, and Deborah K. Smith (2006). "Segmentation of transform systems on the East Pacific Rise: Implications for earthquake processes at fast-slipping oceanic transform faults". In: *Geology* 34.4, p. 289. DOI: 10.1130/G22212.1.

Gregg, Patricia M et al. (2007). "Spreading rate dependence of gravity anomalies along oceanic transform faults." In: *Nature* 448.7150, pp. 183–7. DOI: 10.1038/nature05962.

Griffith, A. A. (1921). "The Phenomena of Rupture and Flow in Solids". In: *Philosophical Transactions of the Royal Society A: Mathematical, Physical and Engineering Sciences* 221.582-593, pp. 163–198. DOI: 10.1098/rsta.1921.0006.

Griffiths, Ross W. and Ian H. Campbell (1990). "Stirring and structure in mantle starting plumes". In: *Earth and Planetary Science Letters* 99.1-2, pp. 66–78. DOI: 10.1016/0012-821X(90)90071-5.

Griffiths, Ross W. and Mark A. Richards (1989). "The adjustment of mantle plumes to changes in plate motion". In: *Geophysical Research Letters* 16.5, pp. 437–440. DOI: 10.1029/GL016i005p00437.

Guillou, Hervé et al. (2014). "Volcanic successions in Marquesas eruptive centers: A departure from the Hawaiian model". In: *Journal of Volcanology and Geothermal Research* 276, pp. 173–188. DOI: 10.1016/j.jvolgeores.2013.12.003.

Haase, K. M., C. W. Devey, and S. L. Goldstein (1996). "Two-way exchange between the easter mantle plume and the easter microplate spreading axis". In: *Nature* 382.6589, pp. 344–346. DOI: 10.1038/382344a0.

Haase, K.M. and C.W. Devey (1996). "Geochemistry of lavas from the Ahu and Tupa volcanic fields, Easter Hotspot, southeast Pacific: Implications for intraplate magma gen-

esis near a spreading axis". In: *Earth and Planetary Science Letters* 137.1-4, pp. 129–143. DOI: 10.1016/0012-821x(95)00217-z.

Hall, Chad E. and Michael Gurnis (2005). "Strength of fracture zones from their bathymetric and gravitational evolution". In: *Journal of Geophysical Research B: Solid Earth* 110.1, pp. 1–15. DOI: 10.1029/2004JB003312.

Hanan, Barry B. and J. G. Schilling (1989). "Easter microplate evolution: Pb isotope evidence". In: *Journal of Geophysical Research* 94.B6, pp. 7432–7448. DOI: 10.1029/JB094iB06p07432.

Haxby, William F and E M Parmentier (1988). "Thermal contraction and the state of stress in the oceanic lithosphere." In: *Journal of Geophysical Research* 93.B6, pp. 6419–6429. DOI: 10.1029/JB093iB06p06419.

Hékinian, R and Daniel Bideau (1995). "Magmatism in the Garrett transform fault (East Pacific Rise near 13 27â^2S)". In: *Journal of Geophysical Research* 100.94.

Hey, Richard et al. (2010). "Propagating rift model for the V-shaped ridges south of Iceland". In: *Geochemistry, Geophysics, Geosystems* 11.3, n/a–n/a. DOI: 10.1029/2009GC002865.

Hicks, Anna et al. (2012). "Tristan da Cunha: Constraining eruptive behavior using the 40Ar/39Ar dating technique". In: *Geology* 40.8, pp. 723–726. DOI: 10.1130/G33059.1.

Hieronymus, Christoph F (2004). "Control on seafloor spreading geometries by stress- and strain-induced lithospheric weakening". In: *Earth and Planetary Science Letters* 222.1, pp. 177–189. DOI: 10.1016/j.epsl.2004.02.022.

Hoernle, Kaj et al. (2000). "Existence of complex spatial zonation in the Galápagos plume". In: *Geology* 5, pp. 435–438.

Hoernle, Kaj et al. (2015). "How and when plume zonation appeared during the 132Myr evolution of the Tristan Hotspot". In: *Nature Communications* 6.1, p. 7799. DOI: 10.1038/ncomms8799.

Huang, Shichun, Paul S. Hall, and Matthew G. Jackson (2011). "Geochemical zoning of volcanic chains associated with Pacific hotspots". In: *Nature Geoscience* 4.12, pp. 874–878. DOI: 10.1038/ngeo1263.

Ingle, Stephanie et al. (2002). "Relationship between the early Kerguelen plume and continental flood basalts of the paleo-Eastern Gondwanan margins". In: *Earth and Planetary Science Letters* 197.1-2, pp. 35–50. DOI: 10.1016/S0012-821X(02)00473-9.

Ito, G. (2001). "Reykjanes 'V'-shaped ridges originating from a pulsing and dehydrating mantle plume". In: *Nature* 411.6838, pp. 681–684. DOI: 10.1038/35079561.

Jones, Stephen M., Nicky White, and John Maclennan (2002). "V-shaped ridges around Iceland: Implications for spatial and temporal patterns of mantle convection". In: *Geochemistry, Geophysics, Geosystems* 3.10, pp. 1–23. DOI: 10.1029/2002GC000361.

Jordahl, K A et al. (1995). "Why there are no earthquakes on the Marquesas Fracture Zone". In: *J. Geophys. Res.* 100.B12, pp. 424–431.

Karson, J. A. and H. J. B. Dick (1983). "Tectonics of ridge-transform intersections at the Kane fracture zone". In: *Marine Geophysical Researches* 6.1, pp. 51–98. DOI: 10.1007/BF00300398.

Katz, R.F. et al. (2007). "Numerical simulation of geodynamic processes with the Portable Extensible Toolkit for Scientific Computation". In: *Physics of the Earth and Planetary Interiors* 163.1-4, pp. 52–68. DOI: 10.1016/j.pepi.2007.04.016.

Katz, Richard F., Marc Spiegelman, and Charles H. Langmuir (2003). "A new parameterization of hydrous mantle melting". In: *Geochemistry, Geophysics, Geosystems* 4.9, n/a–n/a. DOI: 10.1029/2002GC000433.

Katz, Richard F, Rolf Ragnarsson, and Eberhard Bodenschatz (2005). "Tectonic microplates in a wax model of sea-floor spreading". In: *New Journal of Physics* 7, pp. 37–37. DOI: 10.1088/1367-2630/7/1/037.

Kaus, B J P et al. (2016). "Forward and Inverse Modelling of Lithospheric Deformation on Geological Timescales". In: *NIC Series* 48, pp. 978–3.

Keken, Peter van, David A. Yuen, and Arie van den Berg (1992). "Pulsating diapiric flows: Consequences of vertical variations in mantle creep laws". In: *Earth and Planetary Science Letters* 112.1-4, pp. 179–194. DOI: 10.1016/0012-821X(92)90015-N.

Keken, Peter E. van and Carl W. Gable (1995). "The interaction of a plume with a rheological boundary: A comparison between two- and three-dimensional models". In: *Journal of Geophysical Research: Solid Earth* 100.B10, pp. 20291–20302. DOI: 10.1029/95jb01152.

Kent, Ray (1991). "Lithospheric uplift in eastern Gondwana: evidence for a long-lived mantle plume system?" In: *Geology* 19.1, pp. 19–23. DOI: 10.1130/0091-7613(1991)019<0019:LUIEGE>2.3.CO;2.

Kerr, Ross C., C. Mériaux, and J. R. Lister (2008). "Effect of thermal diffusion on the stability of strongly tilted mantle plume tails". In: *Journal of Geophysical Research: Solid Earth* 113.9, pp. 1–12. DOI: 10.1029/2007JB005510.

Kingsley, Richard H. et al. (2002). "D/H ratios in basalt glasses from the Salas y Gomez mantle plume interacting with the East Pacific Rise: Water from old D-rich recycled crust or primordial water from the lower mantle?" In: *Geochemistry, Geophysics, Geosystems* 3.4, pp. 1–26. DOI: 10.1029/2001gc000199.

Kingsley, Richard H. et al. (2007). "Hafnium, neodymium, and strontium isotope and parentdaughter element systematics in basalts from the plume-ridge interaction system of the Salas y Gomez Seamount Chain and Easter Microplate". In: *Geochemistry, Geophysics, Geosystems* 8.4, n/a–n/a. DOI: 10.1029/2006GC001401.

Kirby, Stephen H. (1983). "Rheology of the Lithospere". In: *Reviews of Geophysics* 21.6, pp. 1458–1487. DOI: 10.1029/RG021i006p01458.

Kolandaivelu, Kannikha Parameswari et al. (2017). "Analysis of a conductive heat flow profile in the Ecuador Fracture Zone". In: *Earth and Planetary Science Letters* 467, pp. 120–127. DOI: 10.1016/j.epsl.2017.03.024.

Koppers, Anthony A. P., Robert A. Duncan, and Bernhard Steinberger (2004). "Implications of a nonlinear 40 Ar/ 39 Ar age progression along the Louisville seamount trail for models of fixed and moving hot spots". In: *Geochemistry, Geophysics, Geosystems* 5.6. DOI: 10.1029/2003GC000671.

Koppers, Anthony A. P. et al. (2011). "New 40Ar/39Ar age progression for the Louisville hot spot trail and implications for inter-hot spot motion". In: *Geochemistry, Geophysics, Geosystems* 12.12, n/a–n/a. DOI: 10.1029/2011GC003804.

Kruse, S E et al. (1996). "Evolution and strength of Pacific Fracture zones". In: *Journal of Geophysical Research* 101.B6, pp. 13731–13740. DOI: 10.1029/96JB00645.

Kruse, Sarah E. et al. (1997). "Effective elastic thickness of the lithosphere along the Easter Seamount Chain". In: *Journal of Geophysical Research* 102, p. 27305. DOI: 10.1029/97JB02158.

Kuo, BY and DW Forsyth (1988). "Gravity anomalies of the ridge-transform system in the South Atlantic between 31 and 34.5 S: Upwelling centers and variations in crustal thickness". In: *Marine Geophysical Researches*, pp. 205–232.

Kuykendall, Martha G., Sarah E. Kruse, and Marcia K. McNutt (1994). "The effects of changes in plate motions on the shape of the Marquesas Fracture Zone". In: *Geophysical Research Letters* 21.25, pp. 2845–2848. DOI: 10.1029/94GL02437.

Lavier, LL and WR Buck (2002). "Half graben versus largeâoffset lowâangle normal fault: Importance of keeping cool during normal faulting". In: *Journal of Geophysical Research* 107, pp. 1–16.

Lavier, Luc L., W. Roger Buck, and Alexei N. B. Poliakov (2000). "Factors controlling normal fault offset in an ideal brittle layer". In: *Journal of Geophysical Research* 105.B10, p. 23431. DOI: 10.1029/2000JB900108.

Leahy, Garrett M et al. (2010). "Underplating of the Hawaiian Swell: evidence from teleseismic receiver functions". In: *Geophys. J. Int* 183, pp. 313–329. DOI: 10.1111/j.1365-246X.2010.04720.x.

Liu, Z J (1996). *The origin and evolution of the Easter seamount chain.*

Lomb, N. R. (1976). "Least-squares frequency analysis of unequally spaced data". In: *Astrophysics and Space Science* 39.2, pp. 447–462. DOI: 10.1007/BF00648343.

Lonsdale, P. (1994). "Structural geomorphology of the eltanin fault system and adjacent transform faults of the Pacific-Antarctic plate boundary". In: *Marine Geophysical Researches* 16.2, pp. 105–143. DOI: 10.1007/BF01224756.

Lonsdale, Peter (1988). "Geography and history of the Louisville hotspot chain in the southwest Pacific." In: *Journal of Geophysical Research* 93.B4, pp. 3078–3104. DOI: 10.1029/JB093iB04p03078.

Lonsdale, Peter and Daniel Fornari (1980). "Submarine geology of Malpelo Ridge, Panama Basin". In: *Marine Geology* 36.1-2, pp. 65–83. DOI: 10.1016/0025-3227(80)90041-9.

Macdonald, Ken C. et al. (1980). "Hydrothermal heat flux of the âblack smokerâ vents on the East Pacific Rise". In: *Earth and Planetary Science Letters* 48.1, pp. 1–7. DOI: 10.1016/0012-821X(80)90163-6.

Mahoney, J. J. et al. (1983). "Kerguelen hotspot source for Rajmahal Traps and Ninetyeast Ridge?" In: *Nature* 303.5916, pp. 385–389. DOI: 10.1038/303385a0.

Maia, M. et al. (2000). "The Pacific-Antarctic RidgeâFoundation hotspot interaction: a case study of a ridge approaching a hotspot". In: *Marine Geology* 167.1-2, pp. 61–84. DOI: 10.1016/S0025-3227(00)00023-2.

Maia, Marcia et al. (2016). "Extreme mantle uplift and exhumation along a transpressive transform fault". In: *Nature Geoscience* 9.8, pp. 619–623. DOI: 10.1038/ngeo2759.

Mammerickx, J. (1992). "The Foundation Seamounts: tectonic setting of a newly discovered seamount chain in the South Pacific". In: *Earth and Planetary Science Letters* 113.3, pp. 293–306. DOI: 10.1016/0012-821X(92)90135-I.

Manea, Vlad C et al. (2014). "Subduction of fracture zones controls mantle melting and geochemical signature above slabs." In: *Nature communications* 5, p. 5095. DOI: 10.1038/ncomms6095.

Marques, F.O., P.R. Cobbold, and N. Lourenço (2007). "Physical models of rifting and transform faulting, due to ridge push in a wedge-shaped oceanic lithosphere". In: *Tectonophysics* 443.1-2, pp. 37–52. DOI: 10.1016/j.tecto.2007.07.002.

Matthews, Kara J. et al. (2011). "The tectonic fabric of the ocean basins". In: *Journal of Geophysical Research: Solid Earth* 116.12, pp. 1–28. DOI: 10.1029/2011JB008413.

Maund, J. G. et al. (1988). "Volcanism on Gough Island: A revised stratigraphy". In: *Geological Magazine* 125.2, pp. 175–181. DOI: 10.1017/S0016756800009572.

McCarthy, Mary C. et al. (1996). "Changes in plate motions and the shape of Pacific fracture zones". In: *Journal of Geophysical Research: Solid Earth* 101.B6, pp. 13715–13730. DOI: 10.1029/96JB00646.

McDougall, Ian (1971). "The geochronology and evolution of the young volcanic island of Réunion, Indian Ocean". In: *Geochimica et Cosmochimica Acta* 35.3, pp. 261–288. DOI: 10.1016/0016-7037(71)90037-8.

Menard (1964). *Marine geology of the Pacific*. Vol. 2. 4, pp. 365–366. DOI: 10.1016/0025-3227(64)90048-9.

Menard, H. W. and Tanya Atwater (1969). "Origin of Fracture Zone Topography". In: *Nature* 222.5198, pp. 1037–1040. DOI: 10.1038/2221037a0.

Menard, HW and T Atwater (1968). "Changes in direction of sea floor spreading". In: *Nature*.

Mériaux, C.A. et al. (2010). "On the rise of strongly tilted mantle plume tails". In: *Physics of the Earth and Planetary Interiors* 184.1-2, pp. 63–79. DOI: 10.1016/j.pepi.2010.10.013.

Mittelstaedt, E. et al. (2012). "Multiple expressions of plume-ridge interaction in the Galápagos: Volcanic lineaments and ridge jumps". In: *Geochemistry Geophysics Geosystems* 13.5. DOI: 10.1029/2012GC004093.

Mittelstaedt, Eric, Garrett Ito, and Mark D. Behn (2008). "Mid-ocean ridge jumps associated with hotspot magmatism". In: *Earth and Planetary Science Letters* 266.3-4, pp. 256–270. DOI: 10.1016/j.epsl.2007.10.055.

Mittelstaedt, Eric, Garrett Ito, and Jeroen van Hunen (2011). "Repeat ridge jumps associated with plume-ridge interaction, melt transport, and ridge migration". In: *Journal of Geophysical Research* 116.B1, pp. 1–20. DOI: 10.1029/2010JB007504.

Mjelde, Rolf and J. I. Faleide (2009). "Variation of Icelandic and Hawaiian magmatism: Evidence for co-pulsation of mantle plumes?" In: *Marine Geophysical Research* 30.1, pp. 61–72. DOI: 10.1007/s11001-009-9066-0.

Montelli, R. et al. (2006). "A catalogue of deep mantle plumes: New results from finitefrequency tomography". In: *Geochemistry, Geophysics, Geosystems* 7.11. DOI: 10.1029/2006GC001248.

Moore, Diane E. and David A. Lockner (2011). "Frictional strengths of talc-serpentine and talc-quartz mixtures". In: *Journal of Geophysical Research: Solid Earth* 116.1, pp. 1–17. DOI: 10.1029/2010JB007881.

Moresi, L, F Dufour, and H-B Muhlhous (2003). "A Lagrangian integration point finite element method for large deformation modelling of viscoelastic geomaterials". In: *Journal*

in Computational Physics 184, 476â497. DOI: http://dx.doi.org/10.1016/S0021-9991(02)00031-1.

Morgan, J. P., W. J. Morgan, and E. Price (1995). "Hotspot melting generates both hotspot volcanism and a hotspot swell?" In: *Journal of Geophysical Research* 100.B5, pp. 8045–8062. DOI: 10.1029/94JB02887.

Morgan, JP and DW Forsyth (1988). "Three-dimensional flow and temperature perturbations due to a transform offset: Effects on oceanic crustal and upper mantle structure". In: *Journal of Geophysical Research: ...* 93.6, pp. 2955–2966.

Morgan, WJ (1971). "Convection plumes in the lower mantle". In: *Nature*.

Morrow, Thomas A, Eric Mittelstaedt, and Seung-sep Kim (2019). "Are segmented fracture zones weak ? Analytical and numerical models constrain anomalous bathymetry at the Clarion and Murray fracture zones". In: *Earth and Planetary Science Letters* 512, pp. 214–226. DOI: 10.1016/j.epsl.2019.02.010.

Müller, R. Dietmar, Jean-Yves Royer, and Lawrence A. Lawver (1993). "Revised plate motions relative to the hotspots from combined Atlantic and Indian Ocean hotspot tracks". In: *Geology* 21.3, p. 275. DOI: 10.1130/0091-7613(1993)021<0275:RPMRTT>2.3.CO;2.

Müller, R. Dietmar et al. (2008). "Age, spreading rates, and spreading asymmetry of the world's ocean crust". In: *Geochemistry, Geophysics, Geosystems* 9.4, n/a–n/a. DOI: 10.1029/2007GC001743.

Naar, DF and RN Hey (1989). "Speed limit for oceanic transform faults". In: *Geology* November, pp. 1987–1989.

Nagendra, R., P. V.S. Prasad, and V. L.S. Bhimasankaram (1996). "Forward and inverse computer modeling of a gravity field resulting from a density interface using Parker-Oldenberg method". In: *Computers and Geosciences* 22.3, pp. 227–237. DOI: 10.1016/0098-3004(95)00075-5.

Nataf, Henri Claude and John Vandecar (1993). "Seismological detection of a mantle plume?" In: *Nature* 364.6433, pp. 115–120. DOI: 10.1038/364115a0.

Neuharth, Derek J and EL Mittelstaedt (2017). "Temporal Variations in Hotspot Volcanic Production Caused by Interactions Between Upwelling Mantle Plumes and Phase Transitions". In: *AGU Fall Meeting Abstracts*.

O'Connor, J. M., P. Stoffers, and J. R. Wijbrans (1998). "Migration rate of volcanism along the Foundation Chain, SE Pacific". In: *Earth and Planetary Science Letters* 164.1-2, pp. 41–59. DOI: 10.1016/S0012-821X(98)00165-4.

O'Connor, J. M. et al. (1999). "First seamount age evidence for significantly slower African plate motion since 19 to 30 Ma". In: *Earth and Planetary Science Letters* 171.4, pp. 575–589. DOI: 10.1016/S0012-821X(99)00183-1.

O'Connor, J. M. et al. (2000). "Evidence from episodic seamount volcanism for pulsing of iceland plume in the past 70 Myr". In: *Nature* 408.6815, pp. 954–958. DOI: 10.1038/35050066.

O'Connor, J. M., P Stoffers, and J. R. Wijbrans (2004). "The Foundation Chain: Inferring Hotspot-Plate Interaction from a Weak Seamount Trail". In: *Oceanic Hotspots* 6.0, pp. 349–374. DOI: 10.1007/978-3-642-18782-7{_}12.

O'Connor, John M. and Robert A. Duncan (2008). "Evolution of the Walvis Ridge-Rio Grande Rise Hot Spot System: Implications for African and South American Plate motions over plumes". In: *Journal of Geophysical Research* 95.B11, p. 17475. DOI: 10.1029/jb095ib11p17475.

O'Connor, John M., Peter Stoffers, and Michael O. McWilliams (1995). "Time-space mapping of Easter Chain volcanism". In: *Earth and Planetary Science Letters* 136.3-4, pp. 197–212. DOI: 10.1016/0012-821X(95)00176-D.

O'Connor, John M., Peter Stoffers, and Jan R. Wijbrans (2002). "Pulsing of a focused mantle plume: Evidence from the distribution of foundation chain hotspot volcanism". In: *Geophysical Research Letters* 29.9, pp. 64–1. DOI: 10.1029/2002gl014681.

Okal, Emile A. and Anny Cazenave (1985). "A model for the plate tectonic evolution of the east-central Pacific based on SEASAT investigations". In: *Earth and Planetary Science Letters* 72.1, pp. 99–116. DOI: 10.1016/0012-821X(85)90120-7.

Oldenburg, D W and J N Brune (1972). "Ridge transform fault spreading pattern in freezing wax." In: *Science (New York, N.Y.)* 178.4058, pp. 301–4. DOI: 10.1126/science.178.4058.301.

Oldenburg, Douglas W. (1974). "THE INVERSION AND INTERPRETATION OF GRAVITY ANOMALIES". In: *GEOPHYSICS* 39.4, pp. 526–536. DOI: 10.1190/1.1440444.

Oldenburg, Douglas W. and James N. Brune (1975). "An explanation for the orthogonality of ocean ridges and transform faults". In: *Journal of Geophysical Research* 80.17, pp. 2575–2585. DOI: 10.1029/JB080i017p02575.

Olive, Jean Arthur, Mark D. Behn, and Luca C. Malatesta (2014). "Modes of extensional faulting controlled by surface processes". In: *Geophysical Research Letters* 41.19, pp. 6725–6733. DOI: 10.1002/2014GL061507.

Olive, Jean Arthur et al. (2016). "The role of elasticity in simulating long-term tectonic extension". In: *Geophysical Journal International* 205.2, pp. 728–743. DOI: 10.1093/gji/ggw044.

Parker, R L (1972). *The rapid calculation of potential anomalies.*

Parkin, Craig J. et al. (2007). "Imaging the pulsing Iceland mantle plume through the Eocene". In: *Geology* 35.1, pp. 93–96. DOI: 10.1130/G23273A.1.

Parmentier, E M and W F Haxby (1986). "Thermal-Stresses in the Oceanic Lithosphere - Evidence from Geoid Anomalies at Fracture-Zones". In: *Journal of Geophysical Research-Solid Earth and Planets* 91.B7, pp. 7193–7204.

Parmentier, E. M., D. L. Turcotte, and K. E. Torrance (1975). "Numerical experiments on the structure of mantle plumes". In: *Journal of Geophysical Research* 80.32, pp. 4417–4424. DOI: 10.1029/jb080i032p04417.

Perfit, MR, DJ Fornari, and WI Ridley (1996). "Recent volcanism in the Siqueiros transform fault: picritic basalts and implications for MORB magma genesis". In: *Earth and Planetary Science Letters* 141.

Pickle, Robert C. et al. (2009). "Thermo-mechanical control of axial topography of intra-transform spreading centers". In: *Earth and Planetary Science Letters* 284.3-4, pp. 343–351. DOI: 10.1016/j.epsl.2009.05.004.

Pockalny, Robert a. (1997). "Evidence of transpression along the Clipperton Transform: Implications for processes of plate boundary reorganization". In: *Earth and Planetary Science Letters* 146.3-4, pp. 449–464. DOI: 10.1016/S0012-821X(96)00253-1.

Püthe, C. and T. Gerya (2014). "Dependence of mid-ocean ridge morphology on spreading rate in numerical 3-D models". In: *Gondwana Research* 25.1, pp. 270–283. DOI: 10.1016/j.gr.2013.04.005.

Ragnarsson, Rolf et al. (1996). "Rifts in spreading wax layers". In: *Physical Review Letters* 76.18, pp. 3456–3459. DOI: 10.1103/PhysRevLett.76.3456.

Ray, Jyotiranjan S. et al. (2012). "Chronology and geochemistry of lavas from the Nazca Ridge and Easter Seamount Chain: An ˜30 myr hotspot record". In: *Journal of Petrology* 53.7, pp. 1417–1448. DOI: 10.1093/petrology/egs021.

Révillon, Sidonie et al. (2017). *Young Marquesas volcanism finally located.* DOI: 10.1016/j.lithos.2017.10.013.

Richards, Mark A. and Ross W. Griffiths (1988). "Deflection of plumes by mantle shear flow: experimental results and a simple theory". In: *Geophysical Journal* 94.3, pp. 367–376. DOI: 10.1111/j.1365-246X.1988.tb02260.x.

Richards, Mark A. and Ross W. Griffiths (1989). "Thermal entrainment by deflected mantle plumes". In: *Nature* 342.6252, pp. 900–902. DOI: 10.1038/342900a0.

Richards, Mark A., Robert A. Duncan, and Vincent E. Courtillot (1989). "Flood basalts and hot-spot tracks: Plume heads and tails". In: *Science* 246.4926, pp. 103–107. DOI: 10.1126/science.246.4926.103.

Rohde, Joana Kristin et al. (2013). "Evidence for an age progression along the Tristan-Gough volcanic track from new 40Ar/39Ar ages on phenocryst phases". In: *Tectonophysics* 604, pp. 60–71. DOI: 10.1016/j.tecto.2012.08.026.

Roland, Emily, Mark D. Behn, and Greg Hirth (2010). "Thermal-mechanical behavior of oceanic transform faults: Implications for the spatial distribution of seismicity". In: *Geochemistry, Geophysics, Geosystems* 11.7, n/a–n/a. DOI: 10.1029/2010GC003034.

Roland, Emily et al. (2012). "Seismic velocity constraints on the material properties that control earthquake behavior at the Quebrada-Discovery-Gofar transform faults, East Pacific Rise". In: *Journal of Geophysical Research* 117.B11, B11102. DOI: 10.1029/2012JB009422.

Rona, P. A., L. Widenfalk, and K. Bostrom (1987). "Serpentinized ultramafics and hydrothermal activity at the Mid- Atlantic ridge crest near 15oN." In: *Journal of Geophysical Research* 92.B2, pp. 1417–1427. DOI: 10.1029/JB092iB02p01417.

Rowan, Christopher J. and David B. Rowley (2014). "Spreading behaviour of the Pacific-Farallon ridge system since 83 Ma". In: *Geophysical Journal International* 197.3, pp. 1273–1283. DOI: 10.1093/gji/ggu056.

Rüpke, Lars H. and Jörg Hasenclever (2017). "Global rates of mantle serpentinization and H2production at oceanic transform faults in 3-D geodynamic models". In: *Geophysical Research Letters* 44.13, pp. 6726–6734. DOI: 10.1002/2017GL072893.

Ruscitto, D. M., P. J. Wallace, and A. J. R. Kent (2011). "Revisiting the compositions and volatile contents of olivine-hosted melt inclusions from the Mount Shasta region:

Implications for the formation of high-Mg andesites". In: *Contributions to Mineralogy and Petrology* 162.1, pp. 109–132. DOI: 10.1007/s00410-010-0587-y.

Ryan, William B. F. et al. (2009). "Global Multi-Resolution Topography synthesis". In: *Geochemistry, Geophysics, Geosystems* 10.3, n/a–n/a. DOI: 10.1029/2008GC002332.

Sager, W and Han (1993). "Rapid formation of the Shatsky Rise oceanic plateau inferred from its magnetic anomaly". In: *Nature* 364, pp. 610–613.

Sallarès, Valentí (2003). "Seismic structure of Cocos and Malpelo Volcanic Ridges and implications for hot spot-ridge interaction". In: *Journal of Geophysical Research* 108.B12, p. 2564. DOI: 10.1029/2003jb002431.

Sallarès, Valentí et al. (2005). *Crustal seismology helps constrain the nature of mantle melting anomalies: The Galápagos Volcanic Province*.

Sandwell, D. and G. Schubert (1982). "Lithospheric flexure at fracture zones". In: *Journal of Geophysical Research* 87, pp. 4657–4667. DOI: 10.1029/JB087iB06p04657.

Sandwell, David T. (1986). "Thermal stress and the spacings of transform faults". In: *Journal of Geophysical Research* 91.B6, p. 6405. DOI: 10.1029/JB091iB06p06405.

Sandwell, David T et al. (2014). "New global marine gravity model from CryoSat-2 and Jason-1 reveals buried tectonic structure." In: *Science (New York, N.Y.)* 346.6205, pp. 65–7. DOI: 10.1126/science.1258213.

Scargle, J. D. (1982). "Studies in astronomical time series analysis. II - Statistical aspects of spectral analysis of unevenly spaced data". In: *The Astrophysical Journal* 263, p. 835. DOI: 10.1086/160554.

Searle, RC (1983). "Multiple, closely spaced transform faults in fast-slipping fracture zones". In: *Geology* October, pp. 607–610.

Searle, Roger C. et al. (1993). "The Molokai Fracture Zone near Hawaii, and the Late Cretaceous change in Pacific/Farallon spreading direction". In: pp. 155–169. DOI: 10.1029/GM077p0155.

Shemenda, Alexander I and Andrey L Grocholsky (1994). "Physical modeling of slow seafloor spreading the order The jumps normally occur in the wall of a rift valley resulting in". In: 99.93, pp. 9137–9153.

Sibrant, A. L.R. et al. (2018). "Accretion mode of oceanic ridges governed by axial mechanical strength". In: *Nature Geoscience* 11.4, pp. 274–279. DOI: 10.1038/s41561-018-0084-x.

Simons, Kyla et al. (2002). "Volatiles in basaltic glasses from the Easter-Salas y Gomez Seamount Chain and Easter Microplate: Implications for geochemical cycling of volatile elements". In: *Geochemistry, Geophysics, Geosystems* 3.7, pp. 1–29. DOI: 10.1029/2001gc000173.

Singer, Brad S. et al. (2007). "Along-strike trace element and isotopic variation in Aleutian Island arc basalt: Subduction melts sediments and dehydrates serpentine". In: *Journal of Geophysical Research: Solid Earth* 112.6. DOI: 10.1029/2006JB004897.

Sinha, MC and KE Louden (1983). "The Oceanographer fracture zoneâI. Crustal structure from seismic refraction studies". In: *Geophysical Journal International* 1 983, pp. 713–736.

Sinton, John et al. (2003). "Morphology and segmentation of the western Galápagos Spreading Center, 90.5°-98°W: Plume-ridge interaction at an intermediate spreading ridge". In: *Geochemistry, Geophysics, Geosystems* 4.12, n/a–n/a. DOI: 10.1029/2003GC000609.

Sleep, Norman H (1990). "Hotspots and Mantle Plumes ' Some Phenomenology". In: *Journal of Geophysical Research* 95, pp. 6715–6736.

Sreejith, K. M. and K. S. Krishna (2015). "Magma production rate along the Ninetyeast Ridge and its relationship to Indian plate motion and Kerguelen hot spot activity". In: *Geophysical Research Letters* 42.4, pp. 1105–1112. DOI: 10.1002/2014GL062993.

Storey, M. et al. (1989). "Contamination of Indian Ocean asthenosphere by the Kerguelen-Heard mantle plume". In: *Nature* 338.6216, pp. 574–576. DOI: 10.1038/338574a0.

Taylor, B, K Crook, and J Sinton (1994). "Extensional transform zones and oblique spreading centers". In: *Journal of Geophysical Research*.

Tebbens, S. F. et al. (1997). "The Chile ridge: A tectonic framework". In: *Journal of Geophysical Research* 102, p. 12035. DOI: 10.1029/96JB02581.

Tebbens, SF and SC Cande (1997). "Southeast Pacific tectonic evolution from early Oligocene to present". In: *Journal of Geophysical Research* 102.

Torsvik, Trond H. et al. (2013). "A Precambrian microcontinent in the Indian Ocean". In: *Nature Geoscience* 6.3, pp. 223–227. DOI: 10.1038/ngeo1736.

Tréhu, A. M. and G. M. Purdy (1984). "Crustal structure in the Orozco Transform Zone". In: *Journal of Geophysical Research: Solid Earth* 89.B3, pp. 1834–1842. DOI: 10.1029/JB089iB03p01834.

Tucholke, Brian E. and Hans Schouten (1988). "Kane Fracture Zone". In: *Marine Geophysical Researches* 10.1-2, pp. 1–39. DOI: 10.1007/BF02424659.

Turcotte, DL (1974). "Are transform faults thermal contraction cracks?" In: *Journal of Geophysical Research* 79, pp. 2573–2577.

Turcotte, Donald and Gerald Schubert (2002). *Geodynamics*. Cambridge University Press.

Turner, D. L., R. D. Jarrard, and R. B. Forbes (1980). "Geochronology and origin of the Pratt-Welker Seamount Chain, Gulf of Alaska: A new pole of rotation for the Pacific Plate". In: *Journal of Geophysical Research* 85.B11, p. 6547. DOI: 10.1029/JB085iB11p06547.

Van Ark, Emily and Jian Lin (2004). "Time variation in igneous volume flux of the Hawaii-Emperor hot spot seamount chain". In: *Journal of Geophysical Research: Solid Earth* 109.B11. DOI: 10.1029/2003JB002949.

Vidal, V. and A Bonneville (2004). "Variations of the Hawaiian hot spot activity revealed by variations in the magma production rate". In: *Journal of Geophysical Research* 109.B3, pp. 1–13. DOI: 10.1029/2003jb002559.

Villagómez, Darwin R. et al. (2007). "Upper mantle structure beneath the Galápagos Archipelago from surface wave tomography". In: *Journal of Geophysical Research* 112.B7, B07303. DOI: 10.1029/2006JB004672.

Villagómez, Darwin R. et al. (2014). "Mantle flow and multistage melting beneath the Galápagos hotspot revealed by seismic imaging". In: *Nature Geoscience* 7.2, pp. 151–156. DOI: 10.1038/ngeo2062.

Vogt, P. R. (1971). "Asthenosphere motion recorded by the ocean floor south of Iceland". In: *Earth and Planetary Science Letters* 13.1, pp. 153–160. DOI: 10.1016/0012-821X(71)90118-X.

Vogt, Peter R. et al. (1969). "Discontinuities in sea-floor spreading". In: *Tectonophysics* 8.4-6, pp. 285–317. DOI: 10.1016/0040-1951(69)90039-0.

Watts, A. B. (1978). "An analysis of isostasy in the world's oceans 1. Hawaiian-Emperor Seamount Chain". In: *Journal of Geophysical Research: Solid Earth* 83.B12, pp. 5989–6004. DOI: 10.1029/JB083iB12p05989.

Wendt, J.Immo et al. (1999). "Geochemistry of lavas from the Garrett Transform Fault: insights into mantle heterogeneity beneath the eastern Pacific". In: *Earth and Planetary Science Letters* 173.3, pp. 271–284. DOI: 10.1016/S0012-821X(99)00236-8.

Werner, Reinhard et al. (1999). "Drowned 14-m . y . -old Galápagos archipelago off the coast of Costa Rica : Implications for tectonic and evolutionary models". In: 6, pp. 499–502.

Wessel, P (1990). "Thermal bending stresses and vertical motion on oceanic transform fault". In: *Geophysical Research Letters* 17.12, pp. 2401–2404.

Wessel, Paul (1998). "An empirical method for optimal robust regional-residual separation of geophysical data". In: *Mathematical Geology* 30.4, pp. 391–408. DOI: 10.1023/A:1021744224009.

Wessel, Paul (2001). "Global distribution of seamounts inferred from gridded Geosat/ERS-1 altimetry". In: *Journal of Geophysical Research: Solid Earth* 106.B9, pp. 19431–19441. DOI: 10.1029/2000JB000083.

Wessel, Paul (2016). "Regional-residual separation of bathymetry and revised estimates of Hawaii plume flux". In: *Geophysical Journal International* 204.2, pp. 932–947. DOI: 10.1093/gji/ggv472.

Wessel, Paul and Loren W. Kroenke (2000). "Ontong Java Plateau and late Neogene changes in Pacific plate motion". In: *Journal of Geophysical Research: Solid Earth* 105.B12, pp. 28255–28277. DOI: 10.1029/2000jb900290.

West, Michael, William Menke, and Maya Tolstoy (2003). "Focused magma supply at the intersection of the Cobb hotspot and the Juan de Fuca ridge". In: *Geophysical Research Letters* 30.14. DOI: 10.1029/2003GL017104.

White, Nicky and Bryan Lovell (1997). "Measuring the pulse of a plume with the sedimentary record". In: *Nature* 387.6636, pp. 888–891. DOI: 10.1038/43151.

White, Robert S. (1997). "Rift-plume interaction in the North Atlantic". In: *Philosophical Transactions of the Royal Society A: Mathematical, Physical and Engineering Sciences* 355.1723. Ed. by J. R. Cann, H. Elderfield, and A. Laughton, pp. 319–339. DOI: 10.1098/rsta.1997.0011.

White, RS (1993a). "Melt production rates in mantle plumes". In: *Philosophical Transactions of the Royal Society of London. Series A: Physical and Engineering Sciences* 342.1663, pp. 137–153. DOI: 10.1098/rsta.1993.0010.

White, WM (1993b). "Petrology and geochemistry of the Galápagos Islands: Portrait of a pathological mantle plume". In: *Journal of Geophysical ...* 98.

Whitehead, John A. (1982). "Instabilities of fluid conduits in a flowing earth â are plates lubricated by the asthenosphere?" In: *Geophysical Journal of the Royal Astronomical Society* 70.2, pp. 415–433. DOI: 10.1111/j.1365-246X.1982.tb04975.x.

Whittaker, Joanne M. et al. (2013). "Global sediment thickness data set updated for the Australian-Antarctic Southern Ocean". In: *Geochemistry, Geophysics, Geosystems* 14.8, pp. 3297–3305. DOI: 10.1002/ggge.20181.

Wilcock, William S. D., G. M. Purdy, and Sean C. Solomon (1990). "Microearthquake evidence for extension across the Kane Transform Fault". In: *Journal of Geophysical Research* 95.B10, p. 15439. DOI: 10.1029/JB095iB10p15439.

Wilson, J. Tuzo (1963). "A POSSIBLE ORIGIN OF THE HAWAIIAN ISLANDS". In: *Canadian Journal of Physics* 41.6, pp. 863–870. DOI: 10.1139/p63-094.

Winter, John D. (2001). *An Introduction to Igneous and Metamorphic Petrology*. DOI: 10.1180/minmag.1990.054.374.19.

Wolfson-Schwehr, Monica and Margaret S. Boettcher (2019). "Global Characteristics of Oceanic Transform Fault Structure and Seismicity". In: *Transform Plate Boundaries and Fracture Zones*. Elsevier, pp. 21–59. DOI: 10.1016/B978-0-12-812064-4.00002-5.

Zhao, Dapeng (2007). "Seismic images under 60 hotspots: Search for mantle plumes". In: *Gondwana Research* 12.4, pp. 335–355. DOI: 10.1016/j.gr.2007.03.001.

Zhu, Wenlu et al. (2016). "Experimental evidence of reaction-induced fracturing during olivine carbonation". In: *Geophysical Research Letters* 43.18, pp. 9535–9543. DOI: 10.1002/2016GL070834.

Appendix A: Elsevier Copyright Permissions

Chapter two is published in *Earth and Planetary Science Letters*. Permission to reuse this content in a thesis or dissertation is indicated by the statement below, from Elsevier's copyright (https://www.elsevier.com/about/policies/copyright/permissions):

"Can I include/use my article in my thesis/dissertation? –

Yes. Authors can include their articles in full or in part in a thesis or dissertation for non-commercial purposes."